NORTHWESTERN UNIVERSITY

Silicon-based Porous Ceramics via Freeze Casting of Preceramic Polymers

A DISSERTATION

SUBMITTED TO THE GRADUATE SCHOOL
IN PARTIAL FULFILLMENT OF THE REQUIREMENTS

for the degree

DOCTOR OF PHILOSOPHY

Field of Materials Science and Engineering

By

Maninpat Naviroj

EVANSTON, ILLINOIS

June 2017

Abstract

Silicon-based Porous Ceramics via Freeze Casting
of Preceramic Polymers

Maninpat Naviroj

Freeze casting is a technique for processing porous materials that has drawn significant attention for its effectiveness in producing a variety of tailorable pore structures for ceramics, metals, and polymers. With freeze casting, pores are generated based on a solidification process where ice crystals act as a sacrificial template which can eventually be sublimated to create pores. While the majority of freeze-casting studies have been performed using conventional ceramic suspensions, this work explores an alternative processing route by freeze casting with preceramic polymer solutions. Significant differences exist between freeze casting of a particulate suspension and a polymeric solution. These changes affect the processing method, solidification behavior, and pore structure, thereby introducing new challenges and possibilities for the freeze-casting technique.

The first part of this study explored the processing requirements involved with freeze casting of preceramic polymers, along with methods to control the resulting pore structure. Solvent choice, freezing front velocity, and polymer concentration were used as processing variables to manipulate the pore structures. A total of seven organic solvents were freeze cast with a polymethylsiloxane preceramic polymer to produce ceramics with isotropic, dendritic, prismatic, and lamellar pore morphologies. Changes in freezing front velocity and polymer concentration were shown to influence pore size, shape, and connectivity.

Differences between suspension- and solution-based samples freeze cast under equivalent conditions were also investigated. Certain solidification microstructures were strongly affected by the presence of suspended particles, creating differences between pore structures generated from the same solvents. Additionally, processing of solution-based samples were found to be the more facile technique.

Compressive strength and water permeability of dendritic and lamellar structures were analyzed to determine functional differences between the pore structures. Results show that dendritic structures were up to 30 times stronger, while lamellar structures provided higher permeability constants. A change in freezing front velocity was shown to significantly affect permeability but not compressive strength.

Finally, improved pore alignment along the freezing direction was achieved by controlling the nucleation and growth of solvent crystals through the use of a grain-selection template. Dendritic samples freeze cast with a template showed substantial increase in pore alignment, as determined by image analysis and permeability tests, with the permeability constant increasing by up to 6-fold when compared to a control sample.

Approved by:

____

Katherine T. Faber
Department of Materials Science and Engineering
Robert R. McCormick School of Engineering and Applied Science
Northwestern University
Evanston, IL June 2017

Acknowledgements

There are so many people I would like to thank for making this wonderful journey possible.

First and foremost, Professor Katherine Faber, thank you for being the best advisor and mentor anyone could ask for. The guidance, teachings, and support you provided were instrumental through these five years. Your patience and understanding allowed me to speak my mind and explore new ideas in ways I otherwise would not have dared.

My committee members, which I believe consists of a cast exceptionally fitting for this project, thank you for your valuable time and advice. The diverse range of expertise assembled here have contributed immensely to every aspect of my research. Professor Peter Voorhees, your deep knowledge of solidification theory provided countless ideas and solutions on such a complex topic. Professor Kenneth Shull, thank you for the discussions on polymer chemistry, an area I was never too familiar with. Finally, Professor Colombo, in addition to your invaluable support regarding preceramic polymers, the inception of this project is also thanks to your collaboration from the very first day.

I would also like to thank all the staff and collaborators that have helped made this research possible. Jerry Carsello, Ben Myers, Eric Miller, Mark Seniw, Carla Shute, and Kathleen Stair, your help is what makes the research at Northwestern University as good as it is. Thank you Chi Ma, for your microscopy assistance at Caltech. Xianghui Xiao of

the Advanced Photon Source at Argonne National Lab, the tomography work would not have been possible without your help.

The administrative staff at Northwestern and Caltech deserves a huge credit for making everything run so smoothly, especially under the circumstances which I had to go through. Joan Sullivan and Christy Jenstad, thank you for warmly welcoming me to Caltech as if I were one of your own and making my transition a breeze.

To the Faber Group, Fabian Stolzenburg, Amanda Childers, Zhao Liu, Sarah Miller, Matthew Johnson, Neal Brodnik, Madeleine Wright, Ryan DeBlock, Noriaki Arai, Claire Kuo, Benjamin Herren, Lucy Buannic, Rafa Cabezas Rodríguez, Melody Wang, Hye-Joon Lee, Tim Ekeh, Giacomo Koszegi, Ellen Chuan, Carl Keck, thank you for all the research suggestions, optimism, insightful lunchtime debates, and much much more. This group always felt like family and my experience would not have been the same without each and everyone one of you. Special thanks to Matt Johnson for setting up the new lab at Caltech and saving me at least a couple extra months.

Friends, family, and loved ones which need not be named, thank you for the love and support throughout the years.

–Putt

Table of Contents

List of Tables

List of Figures

CHAPTER 1

Introduction

1.1. Motivation

Pores in ceramic materials are often seen as a detriment since they can undermine the mechanical, optical, and electrical properties of the material.[1] However, nature provides us with numerous examples where pores can provide essential functions.[2] Bone, wood, dentin, and nacre are examples of materials which benefit from the porosity within their structures. The pore structure in bone and wood creates a strong but lightweight frame, while enabling necessary functions such as transport of water or nutrients. On the other hand, dentin and nacre show how exceptional strength and toughness can be achieved when a secondary phase is incorporated with a porous scaffold. Similarly, various engineering components often require materials with pore structures to achieve their functions. For example, porous ceramic components are sought for in applications such as filters, catalyst supports, bone scaffolds, thermal management systems, and electrodes for fuel cells and batteries.[3–6] Depending on the application, the ceramic scaffold material is chosen to provide high strength, thermal and chemical stability, and biocompatibility, while the pore structure provides transport capabilities, high specific surface areas, and low relative densities.[7]

Since each application requires a different pore structure to optimize their performance, the ability to control and tailor the pore structure during processing is beneficial. Of particular need are anisotropic and directionally-aligned pore for applications requiring superior performance in a specific direction. While many processing techniques have been explored, few have shown the promise of creating high-aspect-ratio pores with precise features. Freeze casting is a technique that has gained interest for this very reason. In freeze casting, pores are generated via solidification of a system containing a dispersed solid phase and a liquid sacrificial phase. During solidification, the sacrificial phase forms ice crystals which grow and segregate the two primary components. A sublimation process then removes the sacrificial phase to create pores patterned from the solidification microstructure. A temperature gradient applied during solidification helps produce directionally-aligned porosity. Furthermore, pore structures can be tailored by controlling processing parameters such as solvent choice, freezing front velocity, and solids content.

Although the majority of research on freeze casting has focused on the use of traditional ceramic powders, freeze casting with preceramic polymers as an alternative precursor is an exciting prospect. Preceramic polymers not only provides a larger phase space for porous ceramics, but also introduces processing avenues and solidification behavior not typically achievable with ceramic powders. As such, a wider variety of material compositions and pore networks can be engineered to better serve the needs of various applications.

1.2. Objectives

This work aims to explore new possibilities in the field of ceramics processing by integrating preceramic polymers with the freeze casting technique. As there is a scarcity of prior work on this topic, an understanding of how the two concepts interact must first be established, followed by implementing appropriate adjustments to the processing steps. The extent to which pore structures can be manipulated with this technique is explored through various processing parameters such as solvent choice, freezing front velocity, and polymer concentration. Differences between how the suspension and solution-based processes behave can be understood by comparing samples made under equivalent conditions.

With a solid understanding of the processing conditions and the ability to create various pore structures established, it is important to understand how these structures may perform differently. Hence, mechanical and permeability measurements were chosen to be performed on different freeze cast pore structures.

Finally, modifications to the conventional freeze casting technique can be incorporated to increase process controls during freeze casting. In particular, improved pore alignment along the thermal gradient can be achieved by using a grain-selection template which reduces the number of nucleation sites.

1.3. Thesis Organization

This thesis is organized to such that the necessary background information on the core topics of porous ceramics, freeze casting, preceramic polymers, and solidification are first provided in Chapter 2. In Chapter 3, the basic principles of freeze casting preceramic polymers are discussed, along with the effects of various processing parameters. Chapter 4 offers a comparison between freeze casting of ceramic suspensions and preceramic polymer solutions. Chapter 5 then discusses the the mechanical and permeability properties of various freeze cast pore structures. Chapter 6 introduces a technique to enhance control of the pore structure and increase its alignment. Finally, Chapter 7 summarizes the results and concludes with ideas for future studies.

CHAPTER 2

Background

This chapter covers the main concepts and ideas involved with freeze casting of preceramic polymers. As the underlying goal is to create porous materials, a general understanding of these materials is first established. The various processing techniques used for creating porous ceramics is then discussed, with a focus naturally given to freeze casting. A brief review of preceramic polymers and polymer-derived ceramics is then presented to introduce their behavior and capabilities. Finally, basic solidification theory is also covered due to the importance of solidification behavior on the freeze casting technique and the pore formation process.

2.1. Porous Materials

Porous materials are materials containing a solid matrix phase and a pore phase. The pores can be either open pores, which are connected to the outside environment, or closed pores, which are enclosed and surrounded by the matrix material. Common examples of porous materials seen everyday include wood, sponges, and synthetic foams. Porosity within a material can provide various functions such as lower specific densities, tailored thermal and electrical properties, high specific surface areas, and transport capabilities.[7] A porous material is generally classified according to its pore structure, which can be defined by parameters such as the pore fraction, pore size, pore shape, tortuosity, and interconnectivity. These pores can range in size from the angstrom- and nanometer- scale, seen in materials such as zeolites or metal organic frameworks (MOFs) used for catalysis or molecular separation, to larger micron-sized pores, seen in filters and scaffolds serving functions such as fluid transport.

While all classes of materials (metals, ceramics, and polymers) can be used as the matrix material depending on the properties needed, porous ceramics has emerged as an area of particular interest. Filters, catalyst supports, bone scaffolds, thermal management systems, and electrodes are all modern engineering applications which require porous ceramics due to the thermal and chemical stability, biocompatibility, and unique electrical properties ceramic materials provide.[3–6,8] However, compared to polymeric or metallic systems, ceramics face more stringent processing constraints. The inherent brittleness of ceramic materials requires pore structures to be carefully incorporated such that the mechanical properties of the material are not overly compromised.

2.1.1. Processing Techniques for Porous Ceramics

Ceramics face processing challenges not only from the brittleness of the materials, but also from limitations in processing conditions. Ceramic materials' dependence on powder processing techniques, high densification temperatures, and limited machinability all complicate the process. Thus, various techniques have been developed for creating porous ceramics. In a review article on processing techniques for porous ceramics, Studart et al. categorizes the techniques into three main categories: replication, sacrificial templating, and direct foaming (Fig. 2.1).[9]

The replication technique creates a porous ceramic by using a temporary porous scaffold which has the form and pore structure of the desired final product. Generally, the ceramic material is applied or coated onto a scaffold, and a pyrolysis step is subsequently performed to remove the scaffold. Synthetic structures such as polymeric and carbon foams are often used as the scaffold materials. Replica techniques have been widely used in the industry due to their simplicity. However, drawbacks for this method include the need for an intricate pyrolysis step, struts being susceptible to damage and leading to reduced mechanical properties, and a minimum pore size of roughly 200 µm due to flow constraints during impregnation. In addition to traditional coating-based techniques,

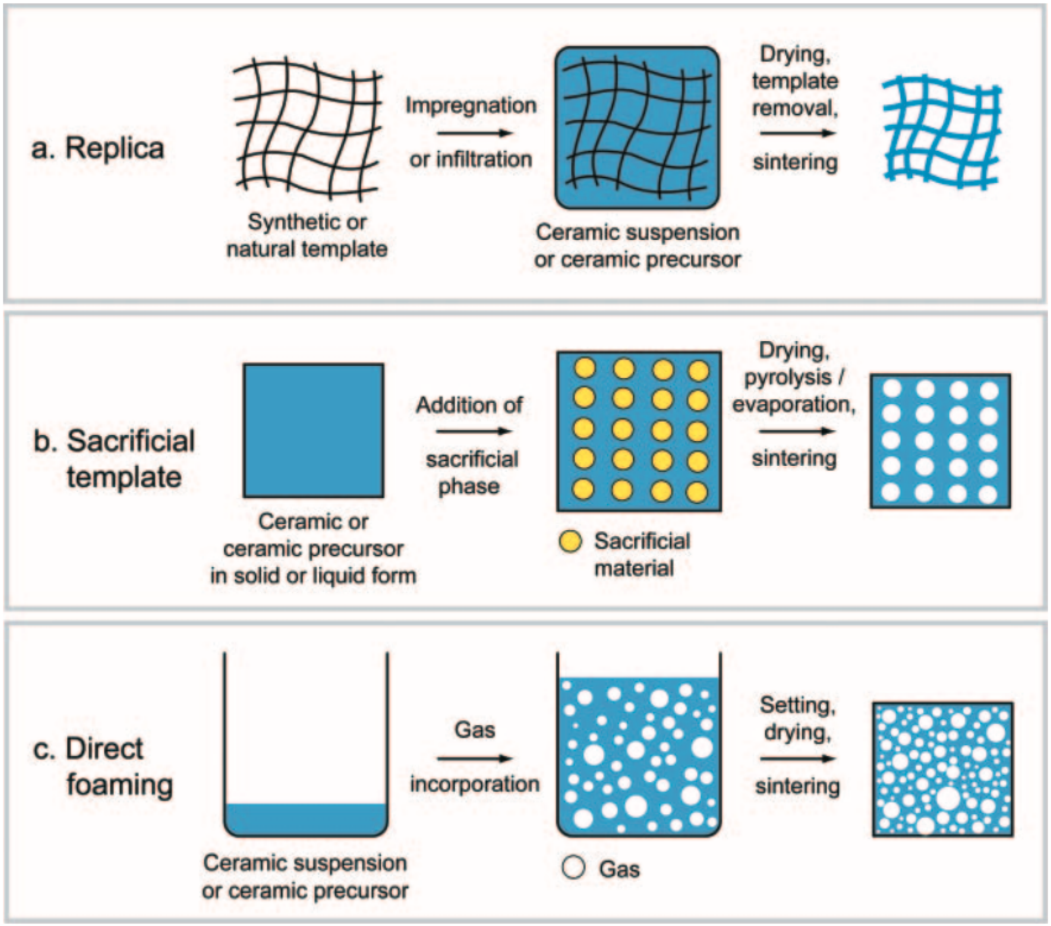

Figure 2.1. Illustrations of the various techniques for fabricating porous ceramics, a) replication, b) sacrificial templating, and c) direct foaming.[9]

a chemical conversion process of the scaffold, such as the graphitization of wood (Fig. 2.2(a)), is also considered a replication technique since the pore structure of wood is replicated.

Sacrificial templating is a technique where pores are generated by using a dispersed sacrificial phase that initially act as space holders. When the sacrificial materials are later removed in the processing step, they create pores with the corresponding shape and size. This method is able to produce a wide variety of porous structures since the sacrificial phase, also called the pore former, is available in various shapes and sizes. Examples of pore formers include starches, polymeric beads, fibers, and ice crystals. For example, Figure 2.2(b) shows a micrograph of a porous ceramic produced using nylon fibers as a sacrificial template. While sacrificial templating is one of the more versatile processing methods with regards to tailorability of the pore network, there can be drawbacks to the technique. Depending on the materials used, a well-dispersed and precisely organized sacrificial phase can be difficult to achieve. In some cases, removal of the sacrificial phase requires intricate burn-out steps that are time consuming and uneconomical.

Direct foaming generates pores by injecting gas into a ceramic suspension or precursor, creating bubbles which then turn into spherical pores (Fig. 2.2(c)). During the foaming process, the precursor material is set using a stabilizing-agent so that the structure generated by the bubbles is maintained. Processing parameters for direct foaming include the amount and rate of gas applied for foaming, as well as the type of stabilization agent or surfactant used. Direct foaming can be used to create porous ceramics in a relatively quick, economical, and environmentally friendly manner. However, pores are limited to spherical morphologies, making the pore structure not particularly tailorable.

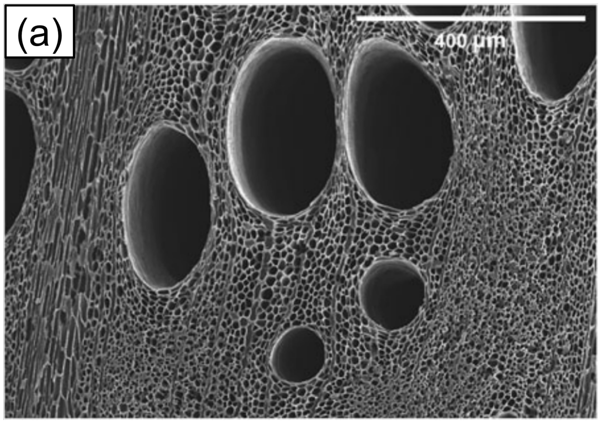

(a) Replication of red oak wood

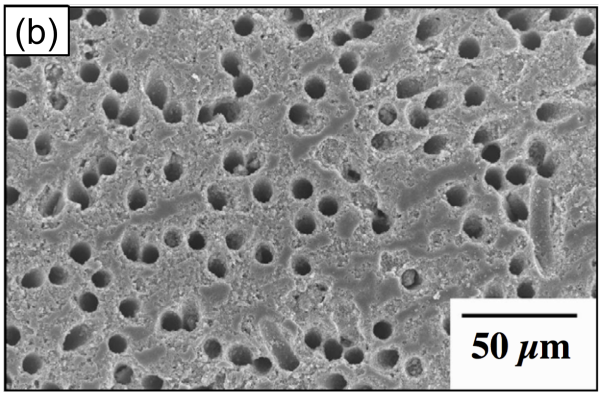

(b) Sacrificial templating of nylon fibers

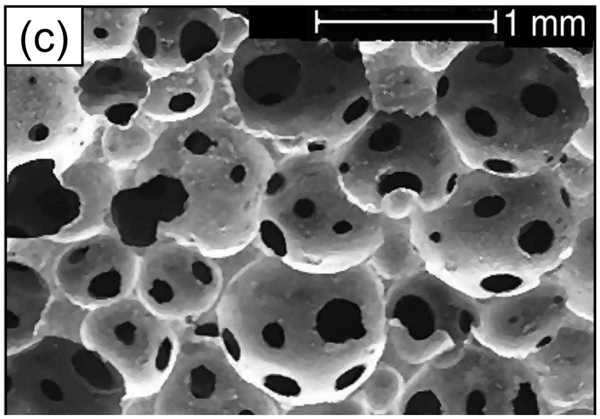

(c) Direct foaming of ceramic slurry

Figure 2.2. Examples of porous ceramics from various processing techniques: (a) replication through graphitization of red oak wood,[10] (b) sacrificial templating of nylon fibers,[11] (c) direct foaming.[12]

2.2. Freeze Casting

Freeze casting is a form of sacrificial templating that has attracted attention for its ability to produce pore structures which are tailorable through various processing parameters.[13–18] Its ability to generate directionally aligned pores and anisotropic structure also differentiates itself from other processing techniques such as partial sintering and direct foaming. This section covers the basic principles of the freeze casting process and the effects of various processing parameters on the pore structure. Focus is given to suspension-based freeze casting of ceramics due to the vast amount of existing literature as compared to solution-based freeze casting. A brief overview of solidification fundamentals is also covered due to their importance in the pore formation process.

2.2.1. Freeze Casting Process

The main concept of freeze casting is based upon a phase segregation process which is achieved through solidification of a mixture consisting of at least two components - a dispersed solid phase and a sacrificial liquid phase. Solidification of the sacrificial liquid phase creates ice crystals which act as templates which are subsequently removed to form a porous structure. Specifically, the freeze casting process generally involves four processes as shown in Figure 2.3. First, the mixture to be used for freeze casting is prepared. Generally, a ceramic slurry (e.g. an alumina powder/water suspension) is used (shown in red), however, a preceramic polymer/solvent solution can also be used (shown in blue), as it is in this work. For suspension-based systems, a stable mixture with minimal sedimentation is desired to obtain consistent samples, meanwhile good compatibility and dissolution between the polymer and solvent is desired for solution-based systems, and

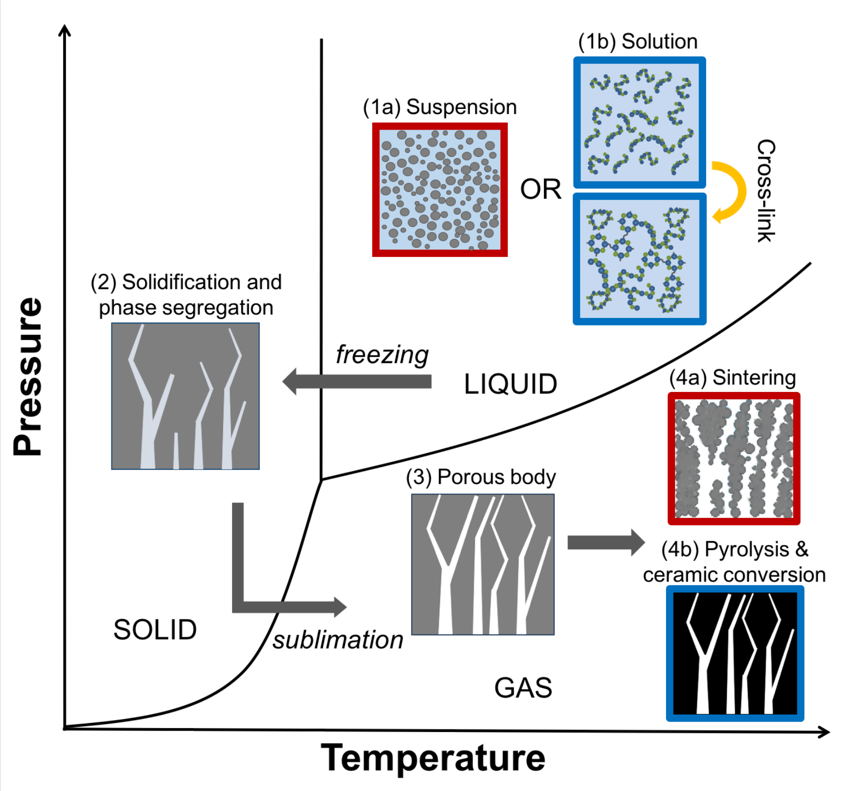

Figure 2.3. Main processes involved in freeze casting of ceramic suspensions or preceramic polymer solutions. Red and blue subfigures refer to processes specific to suspension and solution-based systems, respectively.

partial cross-linking of the polymer must be achieved for the structure to retain its shape through pyrolysis. Next is the freezing step, where the suspension or solution is taken to a temperature below its melting point and crystal growth is initiated. This is the critical process where the pore structure is determined. Third, the fully solidified mixture goes through a sublimation process, often through the use of a freeze dryer. Here, the sacrificial phase is sublimated and removed, leaving a scaffold with a pore structure representative of the ice crystal's growth behavior. Lastly, the porous body is sintered or pyrolyzed in order to densify the scaffold material and create a strong porous ceramic. Of the four essential processes in freeze casting, the mixture preparation and the solidification process are the two steps that have the most influence on the pore network of the final material.[15,19,20]

2.2.2. Processing Variables

Solids Content

Parameters involving the solids content include the solids loading, particle size and shape, and its chemical composition. Varying the solid loadings can lead to changes in the pore fraction, pore size, and interconnectivity of the network. Solid loadings of roughly 5 - 60 vol.% have been used for freeze casting to obtain structures with porosities ranging from 30 - 95%.[19] High solid loadings can lead to difficulties in the solidification and segregation process, while low solid loadings yield structures with compromised mechanical integrity. A study by Peppin et al. has shown that suspensions with high solids concentration tend to impose a destabilizing effect on the solid-liquid interface.[21] Pore size and interconnectivity of the pore network naturally decrease with increasing solid loadings due to decreased available pore space.[19]

Effects of particle size and shape on the freeze casting process have also been extensively studied. Particles ranging from 200 nm to 16 µm have been used.[19] Smaller particles tend to produce more stable colloidal suspensions and also allow for higher resolution and fidelity of the pore structure. However, particles below 100 nm are rarely used as the increase in surface area begins to pose a challenge for obtaining stable dispersions. Additionally, interactions between the suspended particles and the propagating freezing front have been studied. Smaller particles are more resistant to engulfment by the freezing front, as their higher mobility allows for particle redistribution even in relatively high

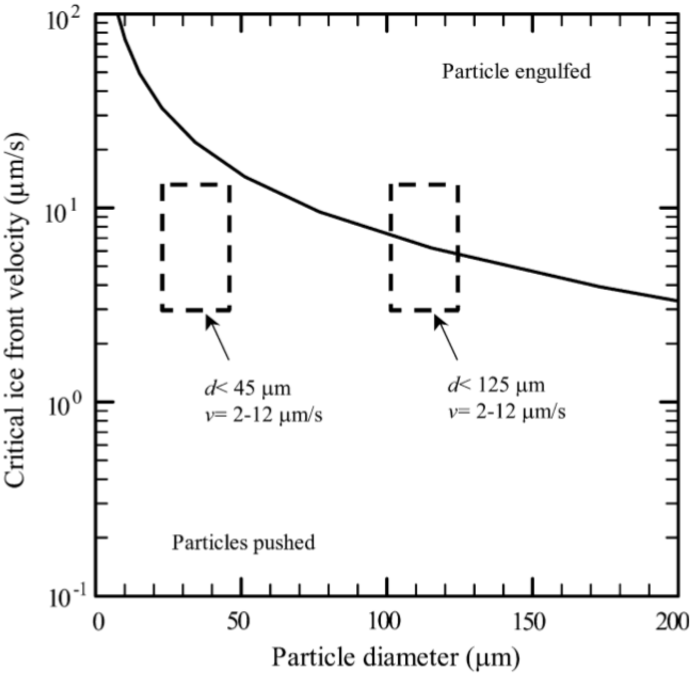

Figure 2.4. Effects of particle size on particle pushing and engulfment at the freezing front.[22]

freezing front velocities, as shown in Figure 2.4.[22] The conditions here are derived from a balance of the attractive (gravity and viscous drag) and repulsive (buoyancy and van der Waals) forces at the freezing interface, and also experimentally tested. Additionally, subtle changes in the periodicity of the pore structures have also been observed in particles with diameters between 100 and 400 nm.[23] Regarding particle shapes, a study by Uhlmann et al. showed that particle roughness had a stabilizing effect on solid-liquid interface, increasing the critical velocity required to break down the planar solidification front.[24] Platelet-shaped particles have been used by Ghosh et al. to induce structural changes in aqueous samples, resulting in improved mechanical properties.[25]

While most work on freeze casting has used ceramic powders, metals and polymers have also been studied. In metallic freeze casting, titanium particles have been the main choice of material; however, issues with high oxygen content and large particle sizes ranging from 20 to 125 µm have been reported.[22,27] Iron and nickel-based freeze casting has also been performed for use in energy-related applications.[28,29]. For polymeric systems, various chemistries including water-soluble PVA and acrylate-based monomers have been explored. Freeze casting of these polymers differs in principle from ceramic and metallic suspensions as they are often fully dissolved as solutions.[30,31] A summary of past studies

Table 2.1. Summary of freeze casting studies performed on ceramics, metals, and polymers, including the types of materials and dispersion media used, as well as general comments.[26]

	Ceramics	Metals	Polymers
Materials	Oxides, carbides, nitrides, borides, etc.	Cu, Au, Ag, Fe, Ni Ti, W, etc.	Agarose, cellulose, gelatin, PVA, PS, PLA, PEG, etc.
Dispersion media	Mostly water, but also camphene and several other organic solvents	Mostly water and camphene	Mostly water (water-soluble polymers), but also solvents such as camphene and naphthalene
Comments	Most widely studied material system; small particles and existing knowledge on colloidal processing enables good control over stable suspensions	Limited to relatively large metal powders; reactivity in air and solvents often pose a challenge	Few studies involving directional solidification; often involve gelation and liquid-liquid phase separation processes which produce isotropic pores

performed on each material system, as well as differences between their freeze casting behavior are shown in Table 2.1.

Dispersion Medium

The choice of dispersion medium is an extremely important processing variable for freeze casting as it directly influences the solidification microstructure, and consequently the pore structure. The most commonly dispersion medium in freeze casting is water due to its well-understood physical and chemical characteristics, low toxicity, and accessible solidification temperature.[23] Camphene is an organic compound that is also often used as a dispersion medium since it can be sublimated in ambient conditions; however, it does have to be processed at elevated temperatures as it has a melting point above room temperature.[13,34] Another compound that has been used in freeze casting studies is t-butanol.[33,35] Figure 2.5 shows an example of the pore structure generated by freeze casting these solvents; water, camphene, and t-butanol generate lamellar, dendritic, and prismatic pore structures, respectively. Reasons behind why each solvent generates a particular solidification microstructure will be discussed in Section 3.3.4.

Freezing Conditions

Traditional solidification studies often define their processing parameters as a combination of the thermal gradient across the solid-liquid interface and the growth velocity defined by a controllable pulling speed. These two variables provide the necessary conditions required for different types of solidification behavior. For many solidification setups such as the Czochralski and Bridgman methods, these parameters can be readily controlled.[36–38]

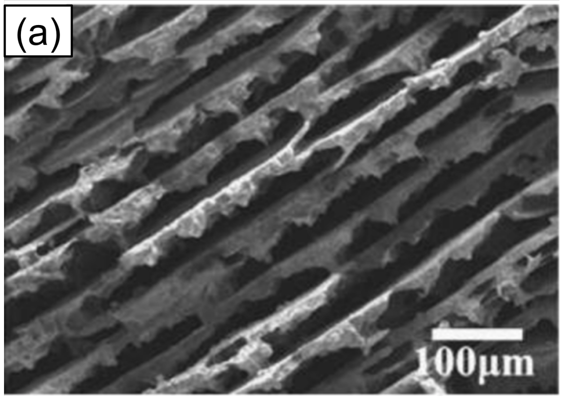

(a) Water

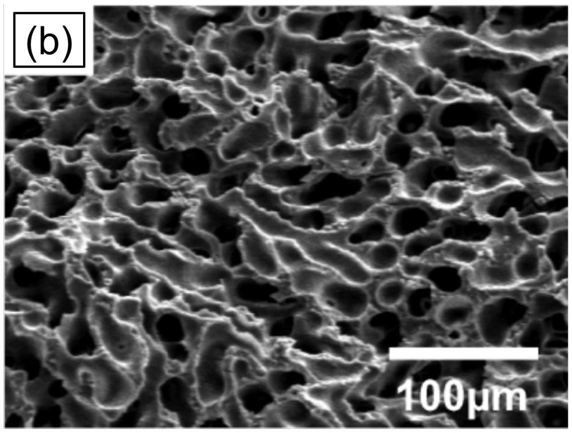

(b) Camphene

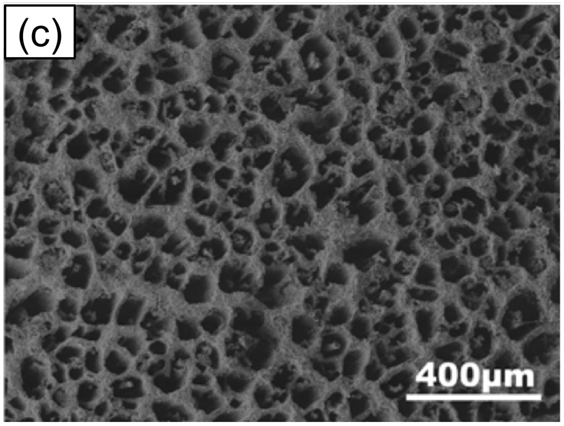

(c) t-Butanol

Figure 2.5. Freeze cast pore structures from various dispersion mediums: (a) water,[32] (b) camphene,[13] (c) TBA.[33]

However, most freeze casting setups thus far have determined the freezing conditions by simply controlling the temperature of the cooling surface in contact with the suspension or solution. The thermal gradient across the interface and the growth velocity are consequently dependent on the temperature of that surface. This limitation still presents challenges for precise control of the solidification conditions during freeze casting.

Controlling the cooling rate or the cold surface temperature influences the kinetics of crystal growth and determines the structure wavelength of the freezing front, thereby affecting the pore size and pore spacing. A fast cooling rate will yield smaller pores and features when compared to a slower cooling rate, as shown in Figure 2.6.[23] A study by Seuba et al. found that faster cooling rates generated thinner pore walls in aqueous-based lamellar structures, which resulted in higher Weibull moduli and improved mechanical reliability (Fig. 2.7).[39] Drastic changes in the freezing conditions such as large temperature gradients and very slow freezing rates can also initiate a transition in microstructural regimes (e.g. dendritic to cellular growth), however this has not been achieved in freeze casting due to the poor temperature control mentioned earlier.[40] In contrast, Samitsu et al. also showed that extremely high cooling rates can vitrify polymer-based samples, creating an isotropic mesoporous structure derived from cold crystallization of the solvent.[41]

The direction of the thermal gradient applied to during freeze casting will also affect the direction of crystal growth, and consequently the anisotropy of the pore structure. Generally, freeze casting is performed under a one-dimensional thermal gradient, with a cold source placed at the bottom of the sample. Ice crystals are formed at the base and grow upward, yielding a directional pore structure. However, several studies have

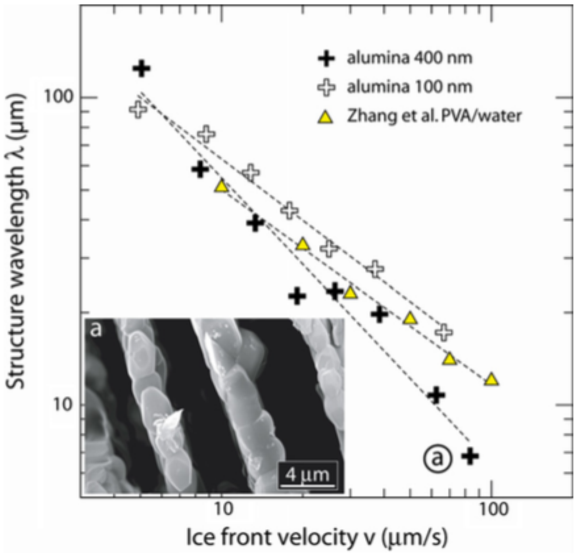

Figure 2.6. Effects of varying cooling rates on the structure wavelength and pore size of freeze cast lamellar structures. Samples were made from aqueous-based suspension of alumina particles, with porosities of roughly 64%.[23]

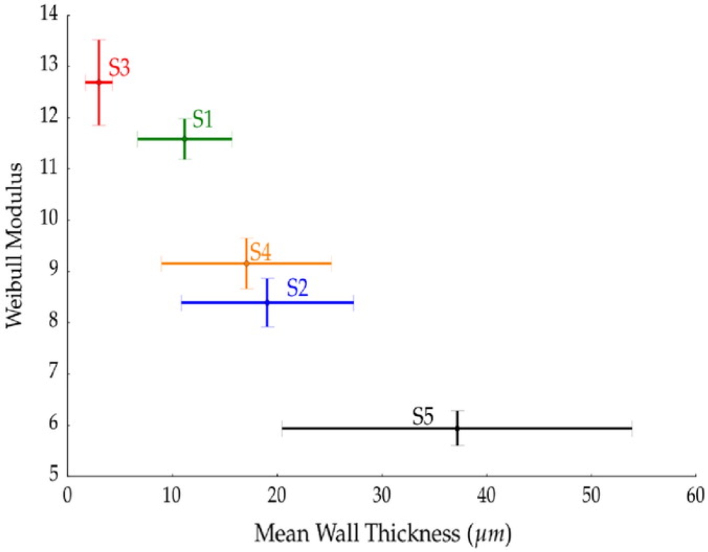

Figure 2.7. Weibull modulus of aqueous-based freeze cast samples with varying lamellar wall thicknesses. Samples produced with faster cooling rates yielded thinner walls and higher Weibull moduli.[39]

implemented more complex setups to enable dual and radial temperature gradients for greater control over the pore structure.[42,43]

Additives

Various additives have been used in aqueous systems to manipulate the solidification behavior and achieve unique pore structures. In one study, Munch et al. used a variety of additives, including sodium chloride, sucrose, glucose, trehalose, gelatin, glycerol, and citric acid to examine their influence on the pore structure of a freeze cast aqueous suspension.[44] Changes in the pore morphology, instability wavelength, and pore size were

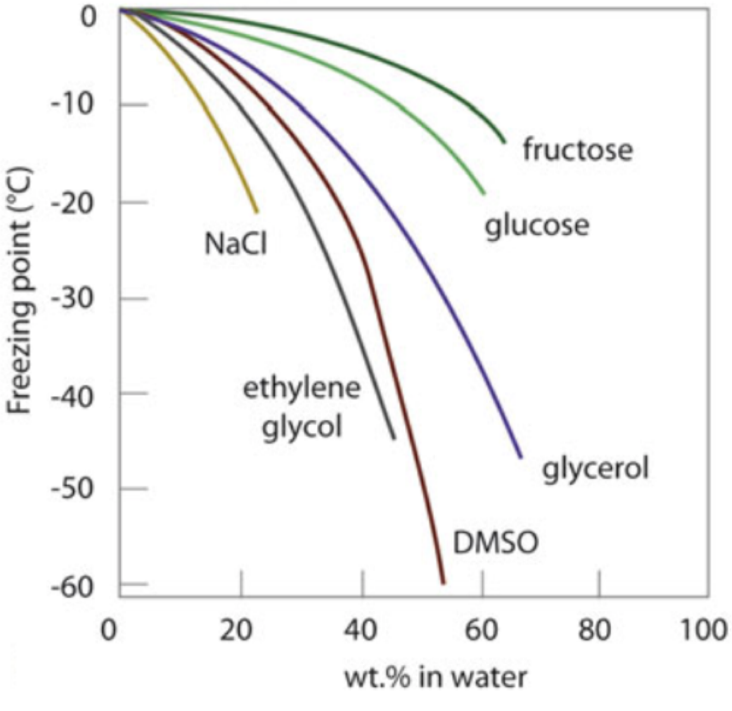

Figure 2.8. Effect of various additives on the freezing point of water, including natural cryoprotectants such as glucose and fructose and synthetic compounds such as dimethylsulfoxide (DMSO).[20]

achieved through the use of these additives. Other studies have also shown the effects of additives such as dioxane[32], polyethylene glycol[45], polyvinyl alcohol,[46] and polyacrylamide[47] on the solidification behavior and pore structure. These additives essentially modify the crystal growth kinetics which dictate the solidification microstructure, such as the viscosity, interface energies, and freezing temperature (Fig. 2.8). The pore structure of freeze-cast samples are therefore highly modifiable through use of such additives.

External Factors

While all the processing parameters discussed thus far have dealt with factors inherent to the freeze casting process, external forces can also be applied to the system to control the pore structure. Porter et al. applied a rotating magnetic field while freeze casting various types of suspensions loaded with Fe_3O_4 nanoparticles. Depending on the chemistry of the solids content, biphasic or homogeneous particle distributions were observed. Interconnectivity and alignment of pore channels can also be adjusted based on inter-particle interactions and the applied rotating magnetic field.[48] Alternatively, Tang et al. made use of the inherent polar characteristics of water molecules to adjust the alignment of lamellar structures by applying an electrostatic field perpendicular to the thermal gradient (Fig. 2.9). The lamellar spacing can also be controlled based on the intensity of the applied electrostatic field.[49] Zhang et al. applied an electric field to manipulate particle rejection forces, resulting in changes in the threshold required for instability of the planar growth. The thickness of a dense ceramic layer at the bottom of the sample was also seen to increase along with the applied voltage intensity.[50] Lastly, a recent study performed freeze casting of TiO_2 suspensions in various reduced gravity environments to determine the effects of gravitational forces and convection on freeze cast structures. Results showed that lamellar spacings decreased with increasing gravitational forces, agreeing with prior microgravity solidification studies performed on binary alloy systems.[51]

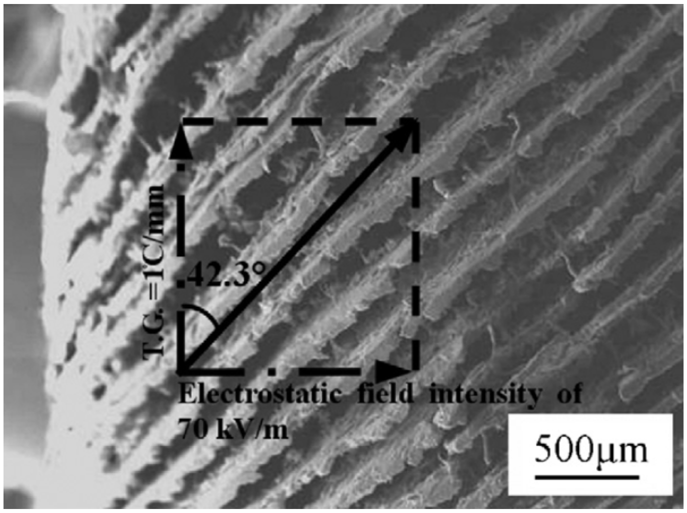

Figure 2.9. Freeze cast lamellar structure with applied electrostatic field perpendicular to the temperature gradient.[49]

2.2.3. Solidification

A solid understanding of solidification theory is vital for freeze casting since the solidification microstructure directly influences the pore structure generated. Extensive studies have been performed on fundamental solidification principles since it is an essential process required for the formation of almost all materials. Yet, it is not fully understood, and new frontiers are still being explored as scientists currently perform studies in space to understand solidification behavior in microgravity environments.[52–54] Metallic systems, and alloys in particular, have been the main focus of solidification studies due to their enormous market size and the strong influence of solidification microstructure on their properties. Certain organic solvents such as succinonitrile have also been used for studies when more accessible experimental conditions are desired. Here, a short review is given of basic solidification theory and how various types of solidification microstructure are formed. With this understanding, various pore structures can be more readily achieved and manipulated during freeze casting.

Interfacial Instability and Constitutional Undercooling

The formation of solidification microstructures can be attributed to the breakdown of planar growth fronts. A system undergoing solidification in thermal equilibrium conditions ideally consists of a planar solid-liquid interface which is microstructurally smooth. However, as crystal growth proceeds in real conditions, the system is bound to experience natural perturbations such as thermal fluctuations, insoluble particles, or grain boundaries. These perturbations can either continue to grow and break down the planar interface if the system is unstable, or subside and allow the interface to remain planar if the system is stable (Fig. 2.10).[55] Under a positive temperature gradient, the perturbations extend into a liquid region with a higher temperature than the solid region and are therefore discouraged from growing; the features should subside and a stable interface is expected. On the contrary, under a negative temperature gradient, the perturbations extend into a liquid region at a lower temperature where continued growth is encouraged; the planar interface breaks down and unstable growth is expected. However, a positive temperature gradient is by far the more common scenario encountered, especially during directional solidification, and yet, microstructures arising from interfacial instabilities are seen in the vast majority of materials. This indicates that the interface can become unstable and breakdown into finer microstructures even under a positive temperature gradient.

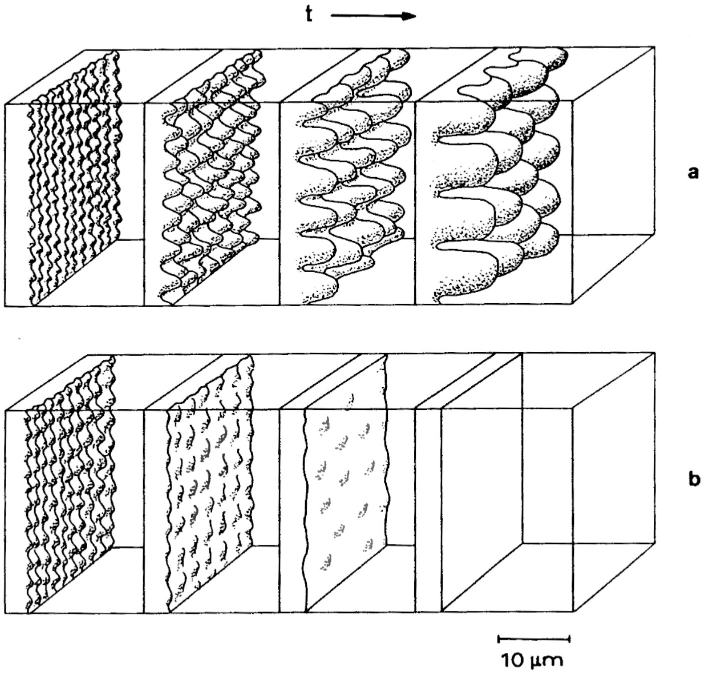

Figure 2.10. Evolution of perturbation effects on unstable and stable solid-liquid interfaces. (a) Perturbations grow under unstable interfacial conditions, breaking down the planar interface and creating solidification microstructures. (b) Under stable interfacial conditions, the perturbations subside and a planar solid-liquid interface is retained.[55]

The main mechanism responsible for interfacial instability under a positive temperature gradient is called *constitutional undercooling.* While the scenarios explained above are theoretically true for pure substances, alloys and real compounds are bound to have some impurities or dissolved solutes. During solidification, there is a rejection of solute from the solid phase into the liquid phase ahead of the interface due to the difference in solubility. This creates a solute concentration pile-up, or a boundary layer, at the interface which decreases exponentially into the melt until it reaches the alloy concentration of $\mathrm{C_0}$, as represented in Figure 2.11. Consequently, since the solute concentration affects the solidification temperature of the liquid ($\mathrm{T_l}$) through freezing point depression, a boundary layer with varying liquidus temperatures is created. This scenario is depicted in Figure 2.11. Here, even with a positive temperature gradient, if the heat flux ($\mathrm{T_q}$) or temperature gradient is not sufficiently strong, a constitutionally undercooled zone is created where the temperature ahead of the interface is lower than that of $\mathrm{T_l}$ and unstable growth is promoted. Depending on the slope of the liquidus line and the temperature gradient, the undercooled zone may be large or small, affecting the growth rate and solidification behavior.[55,56]

As the interfacial instabilities grow to become solidification microstructures, it is important to be able to describe the nature of their features. A systematic analysis to describe this interfacial instability was established by Mullins and Sekerka, and hence the phenomenon is often called the Mullins-Sekerka instability.[57] The analysis is performed by treating the planar interface with a sinusoidal perturbation; thermal and diffusion gradients fields are applied to the boundary conditions and the interface is consequently described. Equation 2.1 represents the Mullins-Sekerka instability criterion:

$$\frac{\dot{\delta}}{\delta} = \frac{\mathrm{V}\omega\left\{-2\mathrm{T_m}\Gamma\omega^2\left[\omega^* - \left(\frac{\mathrm{V}}{\mathrm{D}}\right)(1-\mathrm{k})\right] - (\mathrm{G}' - \mathrm{G})\left[\omega^* - \left(\frac{\mathrm{V}}{\mathrm{D}}\right)(1-\mathrm{k})\right] + 2\mathrm{mG_c}\left[\omega^* - \left(\frac{\mathrm{V}}{\mathrm{D}}\right)\right]\right\}}{(\mathrm{G}' - \mathrm{G})\left[\omega^* - \left(\frac{\mathrm{V}}{\mathrm{D}}\right)(1-\mathrm{k})\right] + 2\omega\mathrm{mG_c}} \tag{2.1}$$

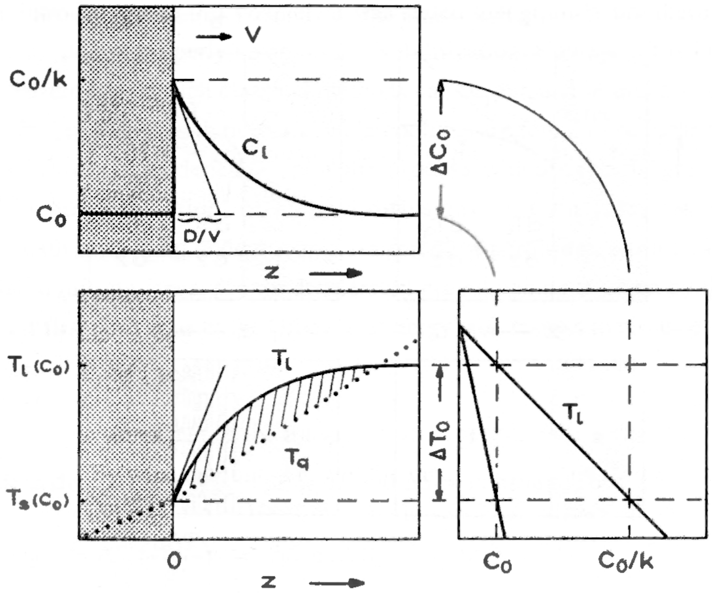

Figure 2.11. Constitutional undercooling due to solute pile-up at the solid-liquid interface. A change in liquidus temperature is generated based on differences in solute concentration. Hatched area shows the constitutionally undercooled region based on the liquidus line and T_q.[55]

where δ is the amplitude of the perturbation at the solid-liquid interface, ω is the frequency of the perturbation, V is the growth rate, T_m is the melting point, Γ is ratio of the solid-liquid surface energy and the heat of fusion, D is the diffusion coefficient, k is the distribution coefficient, G is the temperature gradient adjusted by the appropriate conductivity ratios, m is the slope of the liquidus line, and G_c is the gradient of the solute concentration. Not only does this equation provide the conditions in which perturbations will grow or subside based on the wavelength, it also provides critical information such as the size and wavelength of the features based on the freezing conditions. This serves as a guide for understanding how the pore structure formed from freeze casting can be controlled and manipulated.[30,57,58]

Cells and Dendrites

An unstable interface can grow to form various types of solidification microstructures, with the majority being classified as either *cells* or *dendrites*. Cells represent a structure that is not far removed from the perturbed planar interface, while dendrites represent a more highly unstable interface. Cellular structures have a smooth directional feature

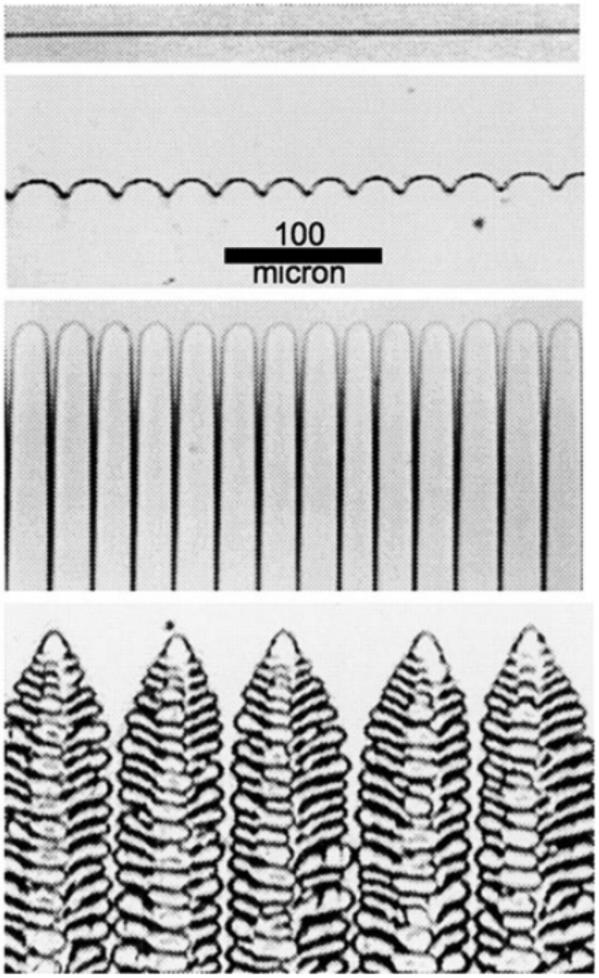

Figure 2.12. Succinonitrile solidified under increasingly higher velocities shows the evolution of the solid-liquid interface from planar to cellular to dendritic.[56]

while dendrites have side-arms and are often described as tree-like. Figure 2.12 shows the evolution of succinonitrile solidified under increasingly unstable conditions and undergoing the transitions from planar, to cellular, to dendritic. The microstructures observed here are representative of classic cells and dendrites, however details of the structure can vary depending on the solidification conditions and anisotropy of the solidifying material.[55,59]

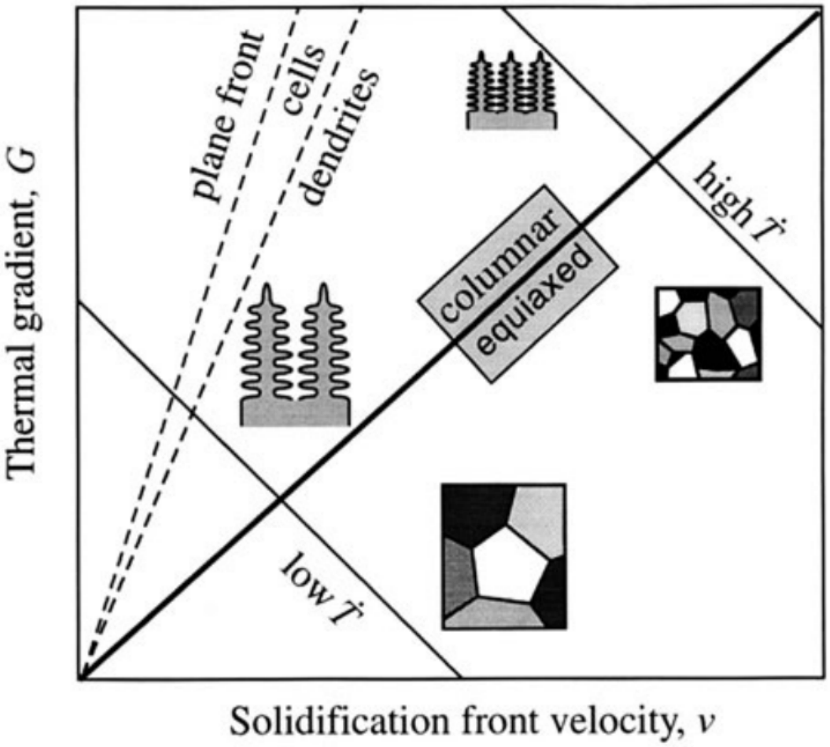

Figure 2.13. Microstructural map of solidification microstructures depending on thermal gradient and solidification velocity.[56]

The transition between these solidification regimes can be controlled during processing by adjusting the thermal gradient across the interface, G, and the solidification velocity, v. These variables are inversely related with regards to maintaining the stability of the solidification front. As shown in a microstructure map in Figure 2.13, the solidification front becomes increasing unstable with low thermal gradients and high solidification velocities. Since the cellular structure is a transient structure between the stable plane and the fully unstable dendrites, the satisfying condition for cellular growth is quite limited. Consequently, various types of dendritic structures make up the majority of the solidification microstructures observed since the conditions for planar growth are relatively extreme and not often achieved under practical circumstances.[55,56]

Crystal Structure and Anisotropy

The idea that conditions of the interfacial instability determined the solidification microstructure operates under the assumption that the solidifying material was isotropic, and any crystallographic characteristics are negligible or disregarded. This assumption helps simplify the kinetics of atomic attachments, leaving crystal growth to be simply determined by diffusion and capillary effects. The non-preferential attachment of atoms results in an interface which is atomically rough and crystal growth is described as *non-faceted.* Cells and dendrites are examples of non-faceted solidification microstructures.

While this is mostly true for simple isotropic materials, other materials can have a higher degree of anisotropy which results in preferential attachment of atoms in certain crystallographic directions. In this scenario, the interface is atomically flat due to selective atom adsorption and crystal growth is *faceted.* Additionally, higher undercoolings are also expected in faceted growth due to the slower growth kinetics.[55,56,60]

The distinction between materials that exhibit faceted and non-faceted growth behavior can be approximated by their enthalpy of fusion. The structural change from the liquid to solid phase for non-faceted materials is not as large compared to faceted materials. Consequently, the enthalpy of fusion for non-faceted materials is generally lower than those of faceted materials.[55]

In order to provide a quantitative analysis of this faceted to non-faceted transition, Jackson et al.[61] developed a model based on the minimum free energy of the system as a function of the surface sites occupied by ad-atoms. The crux of this result is shown in Figure 2.14, where the α-factor is a parameter which shows that the profile of the minimum free energy curve changes at a critical α value of 2. At low α values (< 2), the minimum free energy is located at $\xi = 0.5$, indicating that the interface is atomically roughly and crystal growth is non-faceted. On the other than, when the α values are high (> 2), the minimum free energy is located near $\xi = 0$ or 1, indicating a smooth interface indicative of faceted growth. The α-factor is expressed by:

$$\alpha = \frac{\eta}{\mathrm{Z}} \frac{\mathrm{L}}{\mathrm{kT_m}} \tag{2.2}$$

where η is the number of nearest neighbor sites adjacent to an atom on the interface, Z is the total number of nearest neighbors for an atom within the crystal, L is the enthalpy of fusion, k is the Boltzmann constant, and $\mathrm{T_m}$ is the material's melting temperature.[61–63]

The principles of the Jackson α-factor was derived based upon a 2-layer interface model which is not always representative of actual scenarios as solidification interfaces can exhibit a gradual transition between the solid and liquid phases. Thus, the α-factor does not serve as a rule, but rather a guide which helps give insight to the type of solidification microstructure a material is likely to generate. Exceptions are seen in materials such as white phosphorous, where a low α-factor is accompanied by faceted features. Its cubic

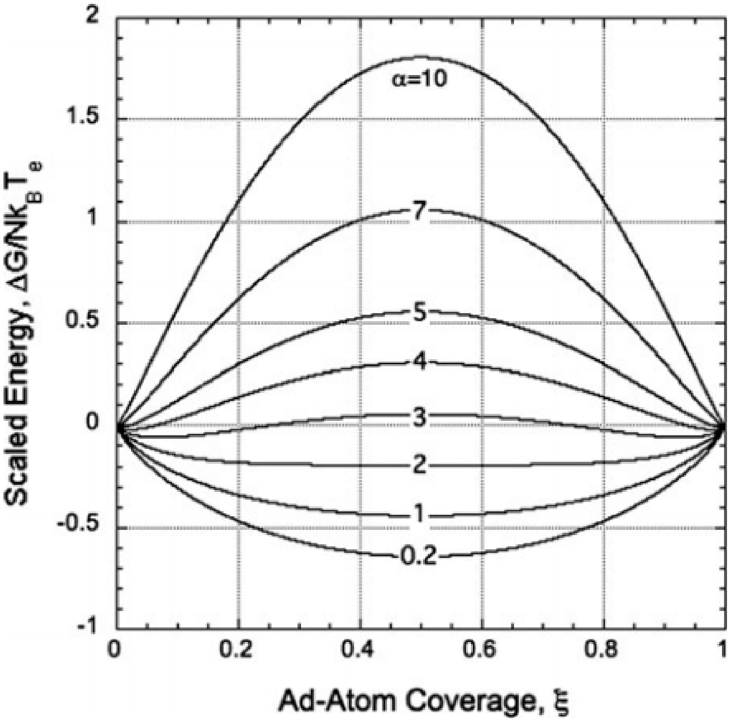

Figure 2.14. The concept of the Jackson α-factor is shown with a plot of the free energy change with respect to the fraction of ad-atom covered sites. A transition in the minimum free energy curve is observed when α is greater or less than 2.[56]

structure consists of 56 P_4 molecules with complex bonding, and therefore does not fall within the scope of the 2-layer interface model used. Nevertheless, various examples have shown that the α-facto is an effective tool. Metals with simple and centro-symmetric crystallographic structures such as Pb, Cu, Ag, and Al tend to have very low α-factors and are observed to produce non-faceted microstructures. On the other hand, non-metallic, semi-metallic, and organic materials such as Bi, Ge, and Salol have high α-factors and generate smooth interfaces with faceted features.[56]

2.3. Preceramic Polymers

Preceramic polymers are alternative precursors for ceramic materials which enables new processing opportunities otherwise not possible with traditional ceramic powders. This study will explore the benefits preceramic polymers can provide when used in conjunction with freeze casting. A general overview of preceramic polymers is first covered, including their physical behavior, processing details, and forming methods. The various types of polymer-derived ceramics (PDCs) consequently attained are then introduced. Focus is given to silicon oxycarbide ceramics derived from polysiloxanes as they are the materials of interest in this study.

2.3.1. Overview of Polymer-Derived Ceramics (PDCs)

Polymer-derived ceramics were discovered in the 1960s when the pyrolysis of organosilicon polymers was shown to yield silicon-based ceramics. The use of preceramic polymers then grew in popularity during the 1970s as Yajima et al. demonstrated that polycarbosilane can be used as a precursor to produce high quality SiC fibers by melt spinning.[64,65] Being polymeric in nature, the physical behavior of preceramic polymers is inherently different from hard materials that are conventionally used for ceramic processing. This allows for increased versatility during processing which was not possible prior to their development. The pyrolysis temperature required to convert the precursor into a ceramic material is lower than regular sintering temperatures. Additionally, increased chemical and structural homogeneity can be achieved with preceramic polymers. When compared to sol-gel processing where monomers are used as precursors, preceramic polymers experience fewer problems with shrinkage and cracking.[66,67]

Preceramic polymers are able to yield a variety of ceramic phase compositions depending on the type of polymer used. Silicon-based precursors have been most heavily studied and used due to their stability and commercial availability. Generally, the organosilicon polymers contain boron, carbon, nitrogen, or oxygen constituents, which in turn can yield various types of PDCs, as shown in Figure 2.15. These can produce a wide range of compositions including binary (SiC, Si_3N_4, etc.), ternary (SiOC, SiCN, etc.easily processed), and quaternary (SiCNO, SiAlCO, etc.) systems. Other variants such as aluminum- and boron-based ceramics can be obtained from their respective organometallic polymers, however they are scarcely studied due to their chemical instability even in ambient conditions.[67,68]

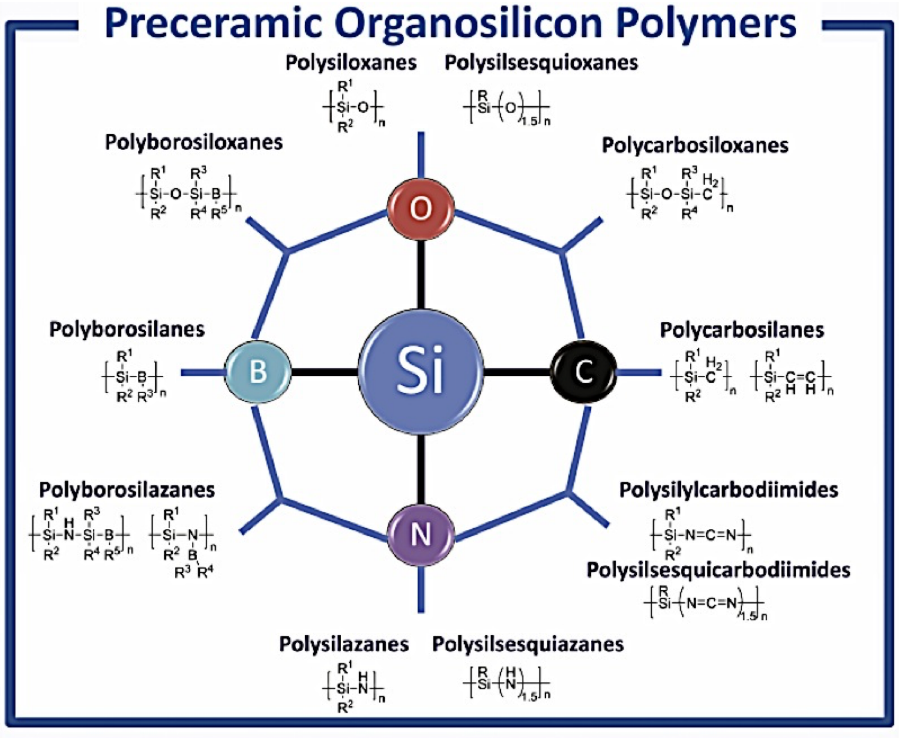

Figure 2.15. Silicon-based polymer-derived ceramics from various organosilicon precursors.[67]

The synthesis process for preceramic polymers determines the composition and properties of the final PDC, as well as factors such as ceramic yield, cross-linking behavior, and viscosity of the precursor. Generally, each type of preceramic polymer can be defined by their backbone and side-groups. Organosilicon polymers contain silicon in their backbone, with the addition of other elements grouping them into classifications such as polysiloxane (oxygen), polycarbosilane (carbon), and polysilazane (nitrogen). Alternatively, side-groups can range from simple groups such as H or CH_3 to more complex groups. Solubility and rheology of the polymer, as well as various properties of the PDCs such as thermal, optical, and electrical can be tailored through these side-groups. Additionally, a balance is usually sought between ceramic yield and processability. Highly branched and large molecular weight polymers give high ceramic yields through pyrolysis due to the lower amount of volatile groups present but are less easily processed and may not dissolve well in various solvents.[68,69]

Shaping and forming of preceramic polymers is highly versatile when compared to traditional powder ceramic processing. Various types of polymer processing techniques can be used to take advantage of the flowability and viscoelastic properties of polymers. Injection molding, coating, spraying, fiber drawing, electrospinning, and ink jetting are some examples of techniques which have been used with preceramic polymers. Additionally, manufacture of ceramic matrix composites often takes advantage of preceramic polymers by using polymer infiltration pyrolysis (PIP), as it is often preferred over chemical vapor infiltration (CVI) for environmental reasons. Shaping and machining parts in the polymeric state is also preferable as it avoids brittle fracture and use of heavy abrasives.[67,70]

The processing procedure for converting a preceramic polymer into a PDC generally involves three steps, as illustrated in Figure 2.16. First, a preceramic polymer is cross-linked and shaped as desired. Cross-linking can be achieved in several ways, often either thermally or by addition of a cross-linking agent. Once the polymer is cross-linked such that the network is robust enough to survive decomposition, it undergoes a pyrolysis step where it is heated in an inert atmosphere. During this process, the polymer converts to a ceramic material as volatile species such as hydrocarbons are removed from the compound. Often times, an amorphous ceramic is initially generated, however crystallization can be achieved at higher temperatures.

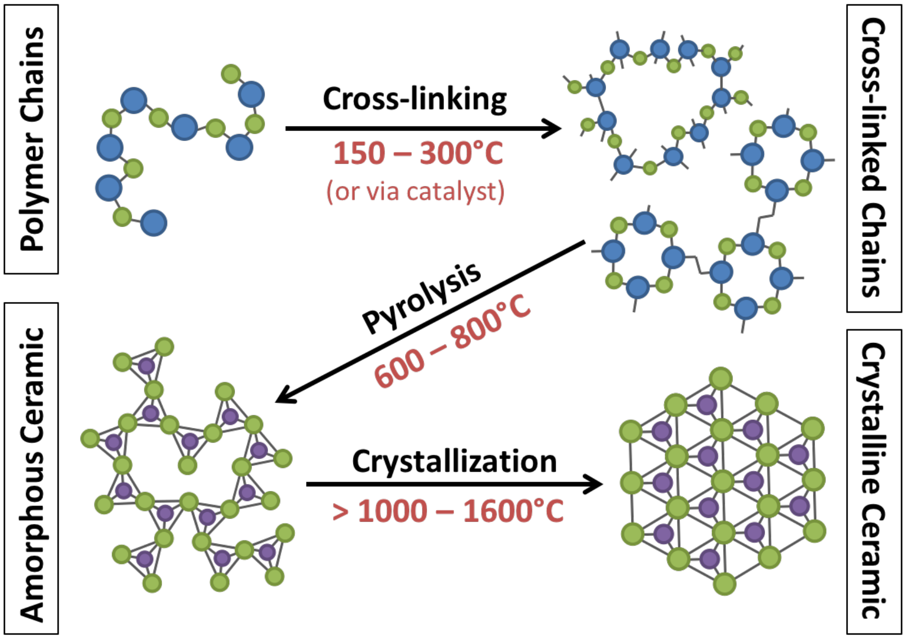

Figure 2.16. General procedure for processing polymer-derived ceramics from preceramic polymers. Adapted from Greil 2000[71]

A major concern for the use of preceramic polymers is the shrinkage that occurs as the volatile species are removed during pyrolysis. This is particularly troublesome when producing dense monolithic components which are prone to cracking since the typical linear shrinkage ranges between 20 and 30%. The use of fillers in the form of passive or active powders has been the main method for minimizing shrinkage. Passive fillers are inert powders which do not react with the preceramic polymer or during heat treatment. The filler reduces shrinkage by simply occupying unchanged volume and providing additional pathways for gas transport. On the other hand, active fillers are powders which react during processing, increasing in volume and thus counteracting the shrinkage. These fillers can be ceramic, metallic, or even polymeric in composition. Reactions usually occur with reactive gases, ceramic residue, or other products generated from polymer decomposition. Naturally, the use of active fillers will generate new phases and result in compositional inhomogeneity. Some of these phases can contribute to the material by adding favorable properties, as with metallic fillers forming metal carbide phases to increase the hardness.[66,67]

2.3.2. Silicon Oxycarbide

Synthesis and Cross-linking of Polysiloxanes

Polysiloxanes are the most commonly used type of preceramic polymer due to their stability, low cost, and high ceramic yield. Various synthesis methods can be used to obtain polysiloxanes, with the simplest involving a reaction of organochlorosilane with water.[67,72] Alternatively, silicon-rich variants of polysiloxanes, namely polysilaethers, can be synthesized through routes such as polycondensation of α,ω-functionalized linear silanes[73] or ring-opening polymerization of cyclic silaethers.[74] The incorporation of side-groups that will cross-link under the desired scenarios is also required so that the structure and shape can be retained through pyrolysis. Depending on the side-group present, polysiloxanes can achieve cross-linking through mechanisms such as thermally activated polycondensation reactions, transition metal catalyst-assisted reactions, and free radical initiation.[69]

Structure and Properties of Silicon Oxycarbide

Silicon oxycarbide (SiOC) can be obtained through pyrolysis of polysiloxane in an inert atmosphere such as nitrogen or argon. During this process, various volatile species are released, including water, ethanol, and methanol at lower temperatures (100 to 400 °C), as well as hydrogen and methane at higher temperatures (600 to 800 °C).[75–78] The atomic structure of the resulting polymer-derived SiOC is similar to that of silica, as it is largely an amorphous network of Si-O bonds. However, the glass network in SiOC contains Si-C bonds in addition to Si-O, as well as free carbon phases such as turbostratic carbon sheets which are dispersed throughout the material. Thus, many properties of SiOC are comparable to a composite of silica and these various constituents. For example, the Si-C bonds help strengthen the glass structure and result in enhanced thermal and mechanical properties.[79,80] Additionally, the free carbon dispersed throughout the network is known to create nanodomains which act as diffusion barriers. As a result, SiOC is black in appearance, and resistant to crystallization up to roughly 1400 °C.[81–83]

The exact structure and properties of SiOC are however highly variable and dependent on the glass network and carbon content. Contrary to rudimentary ideas, the structure of glasses is not correctly described as a purely random network, but rather possessing a degree of nanoheterogeneity which is dependent on the structural features of the precursor, as well as its processing conditions and history.[84] This is especially apparent in the case of SiOC. The molecular structure of the polymeric precursor, degree of cross-linking, additives used, and thermal treatment all determine the composition and structure of the SiOC network. Differences in relative amounts of SiC_4-, SiC_3O-, SiC_2O_2-, $SiCO_3$ and SiO_4- bonds, as well as free carbon within the system, make SiOC a very complex material. Studies have suggested several models of the SiOC network, such as the one shown in Figure 2.17, with segregation of the O-rich and C-rich phases, and the free carbon playing different roles depending on their abundance.[68,85]

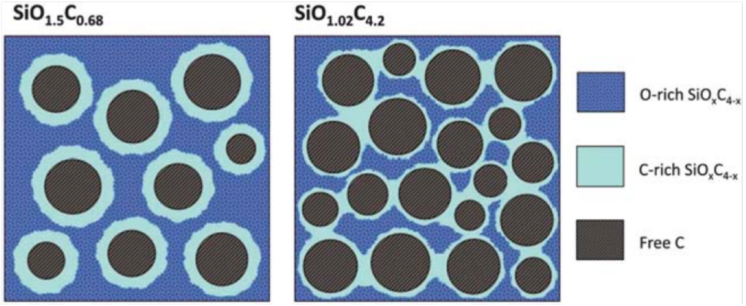

Figure 2.17. A proposed model for SiOC, consisting of segregated O-rich, C-rich, and free carbon domains. The left and right model represents SiOC with low and high carbon contents, respectively.[68]

Recent studies also show that the SiOC network can be controlled and manipulated. Pyrolysis of polysiloxanes in hydrogen[86] or water vapor[87] environments initiates decarburization reactions that reduce the amount of carbon in the SiOC network, resulting in an optically white SiOC. Liang et al. showed that the reduced carbon content was reflected by a lower amount of sp^2 bonded free carbon and C-rich species (SiC_3O, SiC_4), and an increase in O-rich species ($SiCO_3$ and SiO_4), as shown in Figure 2.18.[87] White SiOC obtained through water vapor pyrolysis also showed increased ceramic yield and reduced shrinkage, with no compromise on the mechanical properties. Additionally, it has been shown that 1-D silicon carbide and silicon nitride nanostructures can be grown during pyrolysis of SiOC in the presence of dispersed metal catalyst, further enhancing the complexity of the structure.[78,88,89]

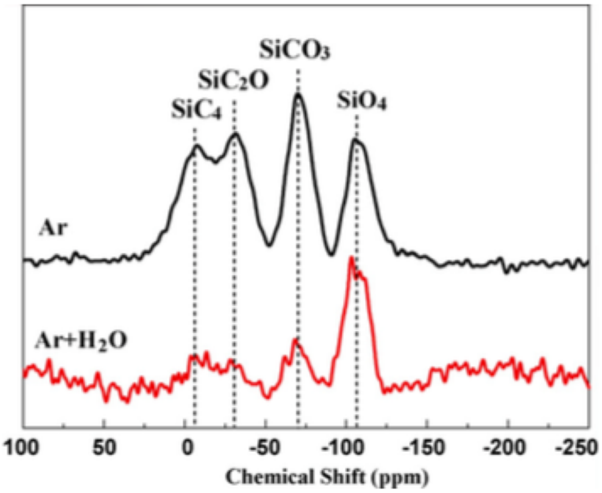

Figure 2.18. Si NMR spectra of SiOC from polysiloxane pyrolyzed in Ar and Ar with water vapor.[87]

The presence of secondary phases within a polymer-derived ceramic has also raised interest as intriguing nanocomposites. For example, a SiOC/$MoSi_2$ composite showed several orders of magnitude of increased electrical conductivity. The change was attributed to the formation of conductive paths dispersed throughout the matrix.[90] SiOC/HfO_2 and SiOC/ZrO_2 nanocomposites was also shown to improve the thermal stability of SiOC by suppressing carbothermal decomposition to temperatures as high as 1600 °C.[91,92]

With this, numerous niche applications have been proposed for polymer-derived SiOC, including battery anodes,[93] pressure sensors,[94] NEMS/MEMS,[95] and various biomedical devices.[96] For example, SiOC has shown improved storage capacity compared to traditional graphite anodes, however it is prone to lithium loss during initial cycling. Piezoresistivity seen in SiOC pyrolyzed at high temperatures also shows potential for use in high temperature sensors. Lastly, SiOC showed the ability to activate coagulation of human blood plasmas, tailorable with the amount of carbon phases, and could be used for artificial heart valves.

CHAPTER 3

Controlling Pore Structure via Freeze Casting of Preceramic Polymers

Material in this chapter is reproduced in part from ”Directionally aligned macroporous SiOC via freeze casting of preceramic polymers”, M. Naviroj et al.; *Journal of the European Ceramic Society*, 35.8 (2015): 2225-2232 and ”Suspension- and solution-based freeze casting for porous ceramics’, M. Naviroj et al.; *Journal of Materials Research*, in press.

3.1. Introduction

As discussed in Section 2.2.1, a considerable amount of work has been performed on freeze casting of ceramic powders (suspension freeze casting), yet little has been explored with regards to fabricating porous ceramics by freeze casting preceramic polymers (solution freeze casting). Namely, a study by Yoon et al. demonstrated the ability to produce polymer-derived SiC ceramics with a dendritic pore morphology by freeze casting a polycarbosilane/camphene solution.[97] Additionally, Zhang et al. recently created hierarchically porous structures through freeze casting partially pyrolyzed preceramic polymers.[98] However, in this case the pyrolyzed polymer acted as suspended particles rather than dissolved solutes, and therefore is not regarded as solution freeze casting despite the use of preceramic polymers. The scarcity of research on preceramic polymer freeze casting, coupled with the fact that not all current understanding regarding suspension freeze casting is directly applicable, motivated these studies.

In this chapter, the fundamentals and capabilities of freeze casting with preceramic polymers are explored. First, a processing method adapted for solution-based systems is introduced, and a means for accurately measuring the freezing front velocity is implemented. Chemical and physical behavior of the preceramic polymer as well as the polymer-derived SiOC are then characterized. Next, control of the pore morphology is demonstrated through changes in the dispersion medium; seven different organic solvents were chosen in order to provide a wide range of enthalpies of fusion. As mentioned in Section 2.2.3, it has been shown that solidification microstructures can be correlated with each solvent's interfacial anisotropy or Jackson α-factor, which is largely dependent on the material's enthalpy of fusion. The effectiveness of this concept in predicting freeze cast pore structures is discussed. Finally, effects of freezing front velocity and polymer concentration on the pore structure are investigated.

3.2. Experimental Methods

3.2.1. Materials

A commercially available polymethylsiloxane (Silres MK powder, Wacker Chemie, CH_3-$SiO_{1.5}$, Munich, Germany) was used as the preceramic polymer. This polymer was chosen for its commercial availability, chemical stability, and high ceramic yield. The molecular weight of this highly branched polymer is roughly 9500 g/mol, and the SiOC obtained following pyrolysis has a carbon content of 13 wt.%.[77,99,100] Additionally, MK powder's rheological and decomposition characteristics are also well-characterized in literature.[101,102]

A range of organic solvents which dissolve the MK powder and have accessible melting points and relatively low toxicities were selected for use in this study, namely, cyclooctane (Sigma-Aldrich, St. Louis, MO, USA), cyclohexane (Sigma-Aldrich), camphene (Alfa Aesar, Ward Hill, MA, USA), tert-butanol (Fisher Scientific, Waltham, MA, USA), dioxane (Sigma-Aldrich), dimethyl carbonate (Sigma-Aldrich), and p-xylene (Sigma-Aldrich). The melting temperatures of these solvents, obtained from the manufacturers, are listed in Table 3.1.

Two cross-linking agents were used in this study: dibutyltin dilaurate (DBTDL, Dabco T-12, Air Products, Allentown, PA, USA) and N-(2-Aminoethyl)-3-aminopropyltrimethoxysilane (Geniosil GF 91, Wacker Chemie, Munich, Germany). The Geniosil GF 91 showed better performance, providing a more robust polymeric body as well as chemical purity, and was therefore used for the majority of the samples.

Table 3.1. Solvents used for freeze casting in this study and their respective melting temperatures. Melting temperatures were obtained from the manufacturers.

Solvent	Melting temperature (°C)
Cyclooctane	11.5
Cyclohexane	5.5
Camphene	35
tert-Butanol	24.5
Dioxane	11
Dimethyl carbonate	3
p-Xylene	12.5

3.2.2. Sample Preparation and Freeze Casting

The typical procedures used for freeze casting (Fig. 2.3) and processing PDCs (Fig. 2.16) were combined to successfully freeze cast preceramic polymers. First, the preceramic polymer was mixed in an organic solvent and dissolved using a magnetic stir bar for ∼10 min. Dissolution was often achieved at room temperature, however slightly elevated temperatures were used for some solvents with higher melting points. Once a homogeneous solution was achieved, 1 wt.% of the cross-linking agent was added in order to partially cross-link the polymer chains. The polymer solution was then poured into a casting mold and placed onto the freeze-casting setup. Following complete solidification, samples were placed in a freeze dryer (VirTis AdVantage 2.0, SP Scientific, Warminster, PA, USA), and held at a pressure of ∼200 mTorr and a condenser temperature of -60 °C until the solvent was fully sublimated. Finally, each sample was pyrolyzed in an inert atmosphere of flowing nitrogen or argon gas to yield a ceramic SiOC. Samples were pyrolyzed at 1100 °C for 4 hours, with a heating rate of 2 °C/min, and cooled down to room temperature at 5 °C/min.

Particular care was required in each of the steps. First, a suitable amount of cross-linking was essential, as a poorly cross-linked sample can lose its structure during pyrolysis, while an excessive amount of cross-linking will yield a gel that is not pourable and cannot be cast. Samples with higher polymer concentrations are naturally more prone to gelation. Additionally, appropriate freeze drying rates were necessary, as cracks can occur if the solvent is sublimated too rapidly. Samples not fully dried prior to removal from the freeze dryer will shrink and deform at ambient conditions. Lastly, relatively low heating rates during pyrolysis were called for prevent cracking.

For the casting mold, a cylindrical borosilicate glass tube was used to provide optical transparency as well as chemical resistance against the various solvents. In order to remove the freeze-dried samples from the mold without deformation or cracking, a clear PET film with a silicone coating was used as a liner, covering the base and the inner diameter of the mold. A thin layer of vacuum grease was also applied between the film and the glass mold in order to create a good seal between the two components.

The freeze casting setup consisted of a thermoelectric device placed on top of a heat sink, which comprised of an aluminum plate attached to a circulating refrigerated silicone oil bath (FP50-ME, Julabo USA, Inc., Allentown, PA, USA). The thermoelectric device was connected to a PID-controller which could regulate a constant temperature, as well as programed temperature profiles.

In order to measure the freezing front velocity, images of the freezing front were recorded using a camera (Sony Alpha a6000, 18-55mm f/3.5-5.6 Lens) attached to an intervalometer. Depending on the solidification rate, images were taken every 10 or 60 seconds, with a shutter speed of 1/30 second. Image analysis was performed using ImageJ (National Institutes of Health) to determine the freezing front velocity. Additionally, since the view of the freezing front can be obstructed by condensation forming on the mold surface during solidification, a transparent beaker was placed over the freeze casting setup to prevent ambient air flow and limit condensation.

3.2.3. Characterization: Chemical and Physical Characteristics

Polymer-to-Ceramic Conversion

In order to examine the polymer-to-ceramic conversion of the MK preceramic polymer, Fourier transform infrared spectroscopy (FTIR) was performed using a Thermo Nicolet Nexus 870 (Waltham, MA, USA). Samples were prepared by mixing 5 mg of material with 500 mg of potassium bromide (KBr). The mixture was finely ground, and 30 mg of the mixture was loaded into a die and pressed into thin pellet. FTIR spectra were obtained for samples at three different conditions: MK powder as-received, pyrolyzed to 600 °C, and pyrolyzed to 1100 °C. Scans were performed from 3500 to 400 cm^{-1}.

Crystal Structure

XRD spectra of freeze cast SiOC pyrolyzed to 1100 °C were collected using a Rigaku Dmax (The Woodlands, TX, USA) to determine the crystallinity of the final material. Scans were performed with Cu-Kα radiation from 10° to 60° 2θ at 0.05° increments, with a dwell time of 2.5 secs. Samples were made with both dibutyltin dilaurate or Geniosil GF 91 as cross-linking agents to evaluate how the SiOC structure might be affected.

True Density

Helium pycnometry was performed on an AccuPyc 1330 (Micromeretics, Norcross, GA, USA) to determine the true density of SiOC after pyrolysis at 1100 °C. Here, the sample was crushed using a mortar and pestle into a fine powder and weighed. The powdered sample was placed in the pycnometer to determine its volume, which, when combined with the mass, can be used to determine the true density negating any open or closed pores. Results were averaged over 10 runs.

Phase Diagram

Polymer-solvent phase diagrams were constructed by direct observation. Temperature was controlled using a PID-controller and the experiments were conducted on the same cold surface used for freeze casting. Each sample was prepared by depositing ∼10 µL of solution onto the cold plate, and immediately covering it with a thin microscope cover slip in order to minimize solvent evaporation which could cause changes in the polymer concentration. A transparent beaker was also placed around the setup to prevent condensation.

Three types of phase transitions were studied for each solvent: the natural freezing point (T_f), the agitated freezing point (T_f*), and the liquidus temperature (T_L). The natural freezing point, T_f, was determined by cooling the solution down at 2 °C/min until solidification ensued; the first observable point of nucleation, discernible by a sudden increase in the opacity, was recorded as the T_f. On the other hand, T_f* was determined using identical conditions, except each sample was repeatedly agitated by tapping the microscope cover slip with a sharp tip until nucleation was observed. Lastly, T_L was determined by first freezing the solution with a cooling rate of 1 °C/sec, followed by heating at 5 °C/min. Samples become optically opaque as they are solidified, and turn transparent as the temperature approaches T_L; the disappearance of the last observable opaque region was recorded as the T_L. Five samples were tested for each condition and their mean and standard deviation are reported. The T_L of deionized water, with an expected value of 0 °C, was used for calibration, assuming linearity at all temperatures.

3.2.4. Characterization: Pore Structure

Porosity and Density

The Archimedes method was used to determine the open porosity (P), bulk density (B), and apparent skeletal density (A) of each sample according to Equations 3.1 - 3.3. The mass of each sample was measured five times under each of three different conditions: dried (D), saturated with water (M), and suspended in water (S). In order to measure the saturated and suspended masses, porous samples were first infiltrated with deionized water by one of two methods: submersed in boiling water for 6 hours, or in vacuum for 30 minutes. Negligible differences were observed between results from the two methods. The water temperature was then allowed to return to room temperature prior to recording the mass, and the density of water was assumed to be 1 g/cm^3.

$$\mathrm{P} = \frac{\mathrm{M} - \mathrm{D}}{\mathrm{M} - \mathrm{S}} \times 100\% \tag{3.1}$$

$$\mathrm{B} = \frac{\mathrm{D}}{\mathrm{M} - \mathrm{S}} \tag{3.2}$$

$$\mathrm{A} = \frac{\mathrm{D}}{\mathrm{D} - \mathrm{S}} \tag{3.3}$$

Pore Size Distribution

Mercury intrusion porosimetry (MIP, Auto Pore IV, Micromeritics, Norcross, GA, USA) was used to analyze the pore size of freeze-cast structures. MIP is a pore characterization technique that uses the non-wetting nature of mercury to obtain information such as the median pore size, pore size distributions, total pore volume, cumulative pore volume, and apparent density of a porous material. This destructive characterization technique measures the volume of mercury infiltrated into pores as pressure is incrementally increased. The data obtained is then used to calculate the various properties listed above according to the Washburn equation:

$$\mathrm{d} = \frac{-4\gamma\cos(\theta)}{\mathrm{P}} \tag{3.4}$$

where d is the diameter or throat size of the pore, γ is the surface tension of mercury, θ is the contact angle between the mercury and the solid, and P is the applied pressure. At low pressures, mercury will fill the larger pores, while smaller pores will be filled as higher pressures are applied. Since the intrusion of mercury is dependent on the surface tension at the pore opening, the data obtained is solely based on the smallest throat size of each pore and its interior volume. The effectiveness of MIP for characterization is therefore limited to materials where the pore throat sizes are similar to the pore diameters. Hence, systems with closed pores, bottle-neck (blind) pores, interconnected (cross-linked) pores,

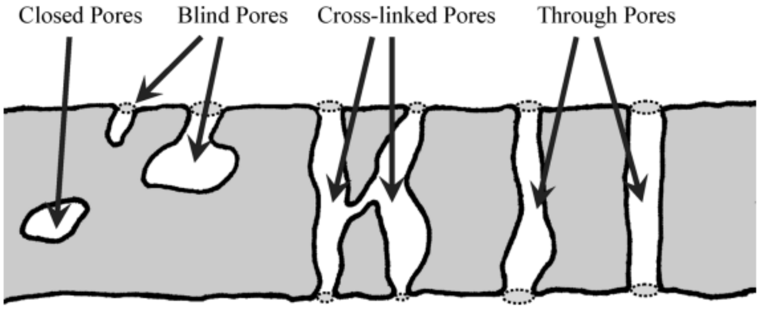

Figure 3.1. Schematic of the various pore geometries pertaining to mercury intrusion porosimetry.[103]

and pores with varying channel widths or complex geometries may yield results that are not representative of their true microstructures (Fig. 3.1).

3D Image Analysis

Three-dimensional microstructural data of porous materials were obtained through X-ray computed tomography (XCT) performed at 2-BM of the APS in Argonne National Lab. The 3D data set of each sample was obtained by reconstructing multiple slices of 2D X-ray radiographs. These 2D images were collected by placing each sample between a detector and an incident X-ray beam, where each sample was slowly rotated through 180° at 1.5° per second. A 25 keV X-ray was used to scan cylindrical samples with a diameter of 3 mm, with an exposure time of 50 ms and a resulting radiograph resolution of 1.47 µm/pixel. Image reconstruction was performed in the Amira image processing software and the geometric surface area was calculated using a marching cubes algorithm performed in MATLAB. The geometric specific surface area (the total calculated geometric surface area normalized by the total pore volume) was used to provide insight regarding the feature size of the pores, where a higher geometric specific surface area corresponds to smaller characteristic length scales.

Optical Microscopy of Solidification Microstructures

Optical microscopy was used to record the solidification microstructures of various preceramic polymer solutions undergoing directional solidification. Polymer solutions were prepared by dissolving 20 wt.% MK powder in cyclooctane, cyclohexane, t-butanol, dioxane, or dimethyl carbonate. A drop of the polymer solution was then deposited between two thin microscope cover slips and placed on a chilled aluminum plate such that a portion of the slip overhangs from the plate. This setup creates a thermal gradient which promotes directional solidification toward the suspended region. The resulting solidification microstructures were observed under an optical microscope, where a mounted digital camera was used to capture the images. In each experiment, the temperature of the cold plate was not well-controlled and ranged roughly between -20 to 0 °C. Consequently, a variety of solidification microstructures were observed from a single solvent.

3.3. Results and Discussion

3.3.1. Chemical and Physical Analysis of Freeze Cast SiOC

FTIR

Figure 3.2 shows the FTIR spectra of the as-received MK preceramic polymer, pyrolyzed to 600 °C, and to 1100 °C. First, the spectrum obtained from the as-received polymer shows all the characteristic bonds expected from a polymethylsiloxane. The broad peak at 1100 cm^{-1} is attributed to the Si-O-Si backbone of polysiloxanes while the peaks at 2900 cm^{-1}, 1270 cm^{-1}, and 800 cm^{-1} correspond to the C-H, Si-CH_3, and Si-C groups present in the side-branches, respectively.[79,104]

Decomposition of the polymer is known to occur at around 600 °C, while at 1100 °C a fully inorganic sample is obtained.[75] FTIR spectra from the as-received MK polymer and those pyrolyzed to 600 °C contained the same peaks, implying that the conversion process is incomplete and the sample is still largely polymeric at 600 °C. However, at 1100 °C, peaks at 1270 cm^{-1} and 2900 cm^{-1} associated with the organic groups Si-CH_3 and C-H, respectively, are absent. This indicates that the material has fully released the volatile species and converted into a ceramic.

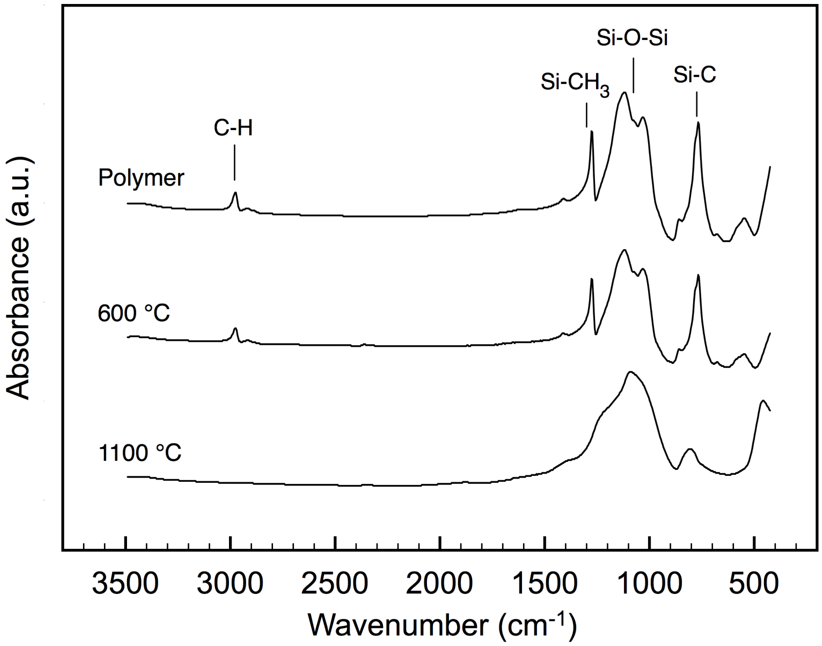

Figure 3.2. FTIR spectra of the MK preceramic polymer as it undergoes the polymer-to-ceramic conversion via pyrolysis.

The 1100 cm^{-1} peak corresponding to Si-O-Si bonds is present in both the polymer and the ceramic material, as the polymeric backbone is converted into a silica glass network after pyrolysis. Similarly, the Si-C peak at 800 cm^{-1} also remained present through all temperatures, as expected from the SiOC structure discussed in Section 2.3.2. These results agree with previous studies regarding the polymer-to-ceramic conversion process for polymethylsiloxanes.[105,106]

X-Ray Diffraction

MK polymer samples cross-linked with Geniosil GF 91 and dibutyltin dilaurate catalysts were pyrolyzed to 1100 °C and analyzed with XRD. Figure 3.3 shows that both samples are structurally amorphous, as indicated by the characteristic broad peak from 16° to 30° 2θ. The amorphous nature of this polymer-derived SiOC is desired and expected from polymer-derived ceramics. These materials are known to have high resistance to creep and crystallization which is attributable to the free carbon that is a remnant of the cross-linked polymeric network. The turbostratic carbon structures create nanodomains that act as obstacles for diffusion and consequently crystallization.[68,83] However, the Geniosil

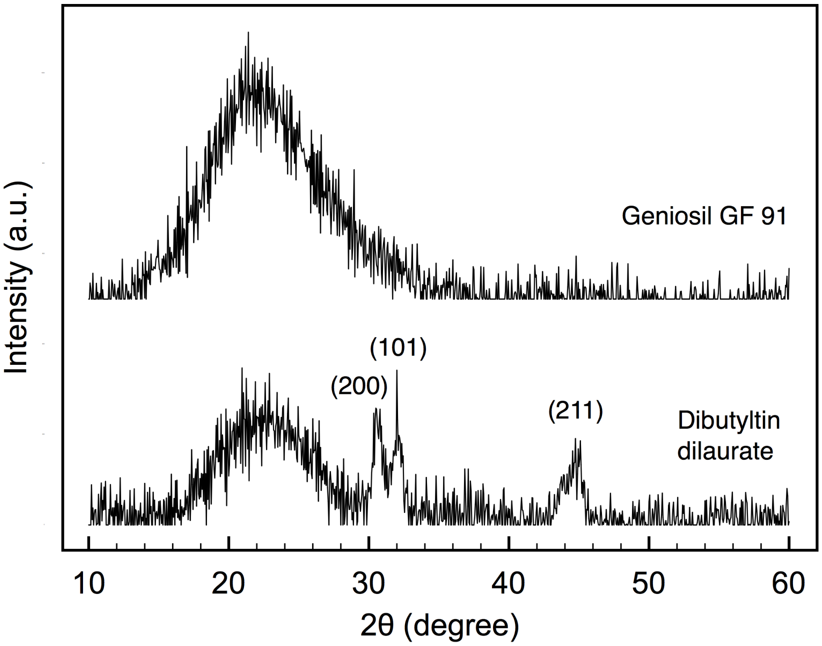

Figure 3.3. XRD spectra of MK preceramic polymer cross-linked with two types of catalyst and pyrolyzed to 1100 °C. Both scenarios yield amorphous structures, however tin contamination is seen with the use of dibutyltin dilaurate.

catalyst produced a clean sample without any crystalline components, whereas several crystalline peaks are seen with dibutyltin dilaurate. The peaks at 30.6, 32.0, and 44.9° 2θ correspond to residual metallic tin which remained with the sample after pyrolysis. The Geniosil is therefore the preferred catalyst as the presence a low melting point metal in the final ceramic material is undesirable.

Density and Porosity

Figure 3.4 shows the bulk density of porous freeze-cast SiOC samples through a range of open porosities, as determined by the Archimedes method. Samples shown here were freeze cast with either cyclohexane or dimethyl carbonate as solvents, with the solvent choice showing no influence on the trend. Pore fraction was controlled by varying the polymer concentration. Samples with lower pore fractions (high polymer concentrations) than 50% were challenging to process as dissolution became difficult and an increase in viscosity also made casting problematic. On the other hand, samples with extremely high pore fractions can be produced, but a rapid decrease in the mechanical integrity was observed with decreasing polymer concentration.

Table 3.2 shows the true density of SiOC obtained from helium pycnometry, as well as the average apparent skeletal density of samples from Figure 3.4. The closed porosity of freeze cast samples can then be calculated according to the following equation:

$$\mathrm{C} = \left[\left(1 - \frac{\mathrm{B}}{\mathrm{T}}\right) \times 100\right] - \mathrm{P} \tag{3.5}$$

where C is the closed porosity, B bulk density, T is the true density, and P is the open porosity.

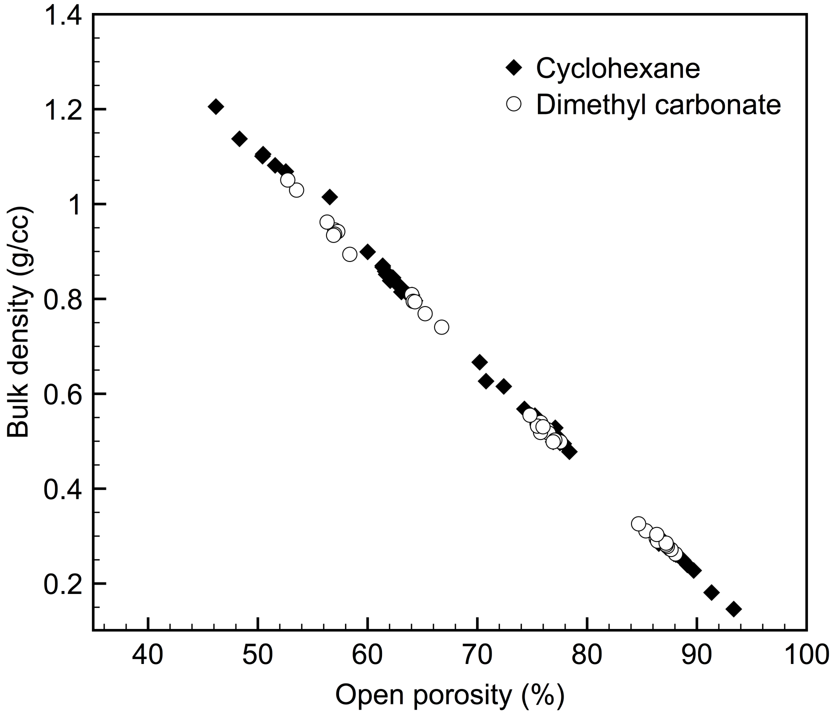

Figure 3.4. Bulk density versus apparent porosity of one hundred freeze cast SiOC samples, determined by Archimedes' method. Samples shown here were freeze cast with either cyclohexane or dimethyl carbonate as solvents.

Table 3.2. True density, apparent skeletal density, and closed porosity of freeze-cast SiOC ceramic pyrolyzed at 1100 °C calculated from helium pycnometry and the Archimedes method.

True density (g/cm^3)	Apparent skeletal density (g/cm^3)	Closed porosity (%)
2.32 ± 0.02	2.21 ± 0.04	1.18 ± 0.56

The low amount of closed porosity seen here with freeze-cast samples is expected. Pore formation during freeze casting creates predominantly open porosity since the phase segregation process in directional solidification is continuous through the height of the sample.

The closed pores observed here could be attributed to residual solvent molecules which remained soluble within the polymer throughout solidification, or simply experimental error associated with both helium pycnometry and the Archimedes method.

3.3.2. Polymer-Solvent Phase Diagrams

A set of experiments was first performed with deionized water, where T_L, T_f*, and T_f were determined to be 0.5, -3.9, and -12.9 °C, respectively. Since T_L was used as the calibration temperature, measured temperatures for all solvents were subtracted by 0.5 °C. The T_L and T_f* of water are within expected values, however the natural freezing point, T_f, is relatively low; this is possibly due to the experimental setup: a small amount of liquid restricted beneath a glass slide limits many natural motions such as convection which could help induce nucleation.

Figure 3.5 shows polymer-solvent phase diagrams of the MK preceramic polymer dissolved in several select solvents, namely, cyclooctane, cyclohexane, dioxane, and dimethyl carbonate; these solvents were chosen for closer investigation as they will be the most frequently used in following studies. Results show that every solvent had a higher liquidus temperature than freezing point, with the agitated freezing point consistently higher than the natural freezing point. These trends are as expected as the melting process is thermodynamically determined, while freezing is kinetically limited since a favorable nucleation site has to be encountered, and additional energy is required to form a nuclei. Agitating each sample during solidification helps facilitate their higher freezing temperature by effectively minimizing the influence of kinetically-limited processes; the agitation process is analogous to the ultrasound-assisted solidification technique employed to trigger ice

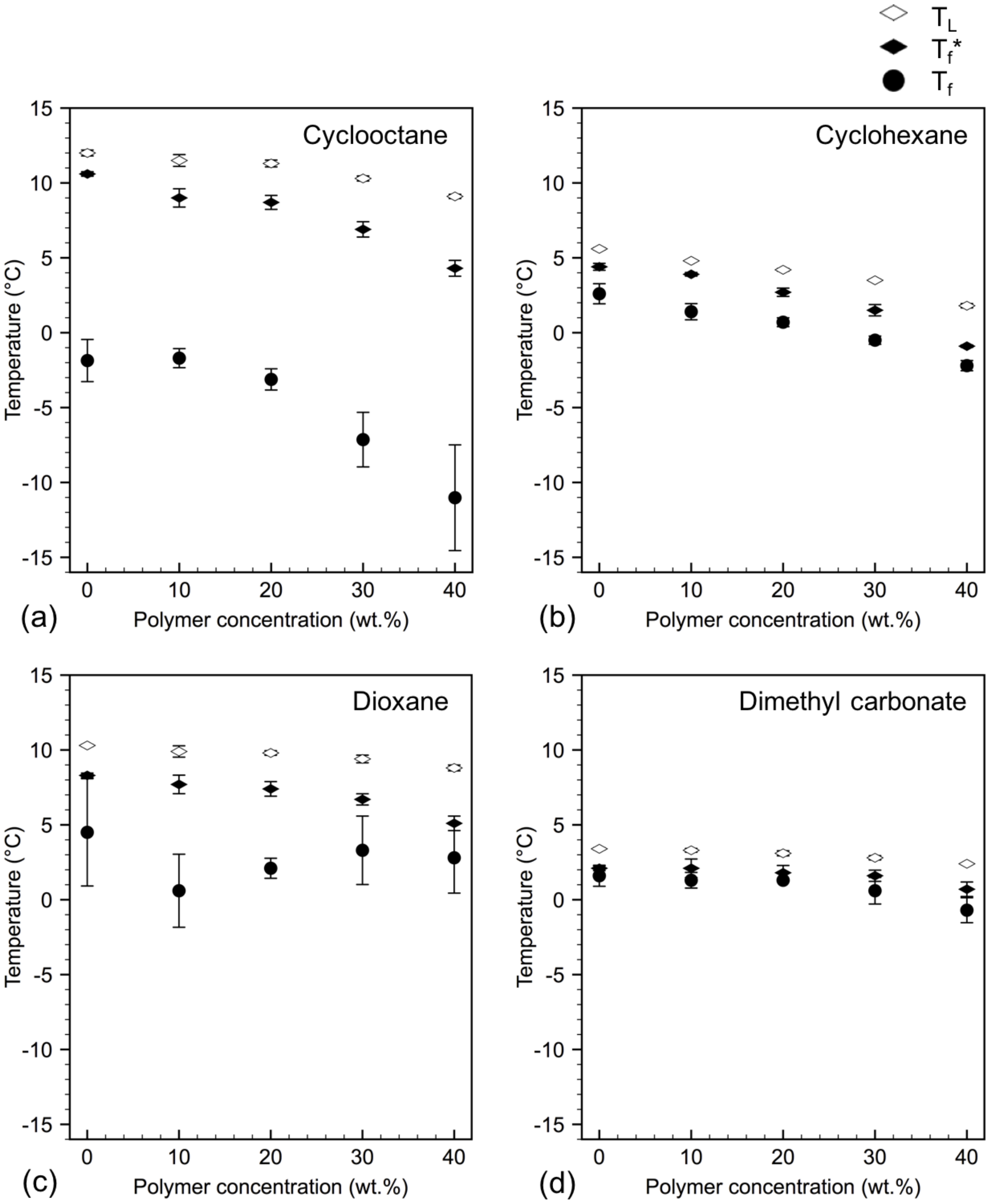

Figure 3.5. Polymer-solvent phase diagrams for MK powder and (a) cyclooctane, (b) cyclohexane, (c) dioxane, and (d) dimethyl carbonate.

nucleation.[107,108] The small error bars associated with the T_L and T_f*, as well as the low temperatures and large error bars associated with T_f support these observations. Additionally, melting and freezing point depressions can clearly be observed in all solvents as the polymer concentration increases. The effects are evident, as the T_L and T_f* decrease by roughly 1 to 5 °C for all solvents, from 0 to 40 wt.% polymer concentration.

Looking at each solvent individually, cyclooctane solutions (Fig. 3.5(a)) show a particularly large discrepancy between T_f and T_f*, more than 10 °C, indicating that the solvent can experience significant undercooling due to difficulty in locating a suitable nucleation site. In contrast, cyclohexane solutions (Fig. 3.5(b)) solidified with the T_f consistently $\sim$2 °C below the T_f*, and standard deviations of less than 0.7 °C. Dioxane solutions (Fig. 3.5(c)) show results similar to cyclooctane, where a low T_f corresponding to a large degree of undercooling is observed. Interestingly, pure dioxane solvent shows a very high variability in T_f, implying that the presence of polymer (solute) is not the cause of the variability in the natural freezing point, but rather the natural bonding and crystal structure of dioxane. Lastly, Figure 3.5(d) shows that the melting and freezing point depression of dimethyl carbonate are quite small, often less than 1 °C. The difference betweens between dimethyl carbonate's T_f and T_f* is also marginal. Overall, results for T_L paralleled those for T_f* for all samples, however certain solvents (i.e. cyclooctane and dioxane) were more prone to undercooling and displayed significant differences between T_f and T_f*, as well as large variability in the T_f. Moreover, the measured T_L of pure solvents matched very well with the values obtained from the manufacturers in Table 3.1, demonstrating the reliability of this method.

3.3.3. Effects of Dispersion Medium on the Pore Morphology

The images shown in this section demonstrate the range of pore structures that were successfully generated by freeze casting preceramic polymer with the solvents listed in Table 3.1. All samples shown here were processed with 20 wt.% polymer concentration to yield open porosities of roughly 75%, unless noted otherwise. The seven solvents used here generated pore structures which can be grouped into four distinct morphologies: isotropic, dendritic, prismatic, and lamellar.

Isotropic Pores

Cyclooctane was the only solvent to generate a surprisingly isotropic pore structure despite the temperature gradient applied during freeze casting. Figure 3.6 shows that the transverse and longitudinal orientations have no discernible difference, an indication of the isotropic pore morphology. The pores generated from cyclooctane are spherical in

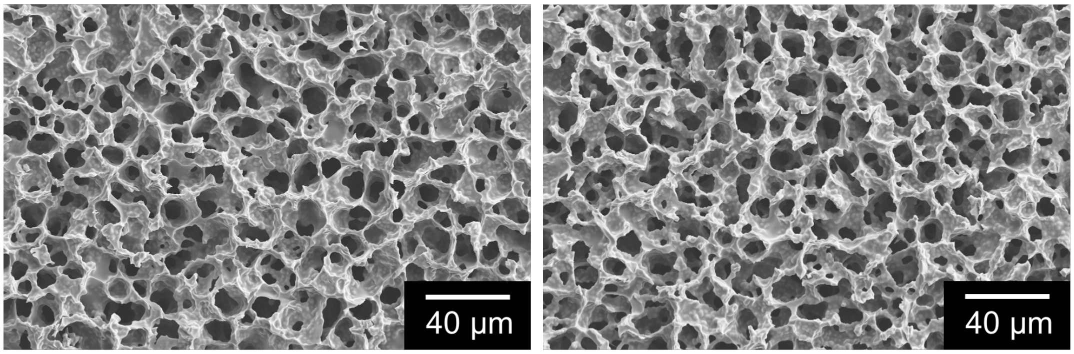

(a) Cyclooctane transverse

(b) Cyclooctane longitudinal

Figure 3.6. SEM micrographs of an isotropic pore morphology obtained by freeze casting with cyclooctane - transverse and longitudinal views show no difference in pore structure.

shape, and the structure can be described as foam-like. The pores seen here are also relatively small when compared to those of other freeze cast microstructures.

Dendritic Pores

Figure 3.7 shows the dendritic pore morphologies obtained from freezing cyclohexane, camphene, and dioxane. In all three cases, images from the transverse orientation clearly show a classic case of primary dendrite tips with pinched secondary arms. The longitudinal orientation shows the secondary dendrite arms which branch out from each of the primary dendrites. Unlike the isotropic structure seen with cyclooctane earlier, these dendrites create an anisotropic structure with directionality based on the applied thermal gradient.

Cyclohexane and camphene produced very similar pore structures, particularly with regard to the secondary dendritic arms seen in the longitudinal orientations (Figs. 3.7(b), 3.7(d)). However, cyclohexane formed consistent and well-defined dendrite tips as opposed to camphene's irregularly shaped tips (Figs. 3.7(a), 3.7(c)). This defect is possibly a result of camphene acting as a plasticizer for the preceramic polymer. Even after prolonged freezing drying ($>$ 7 days), samples would contain residual camphene which caused them to be prone to deformation. Notably, this issue was not observed with any other solvents.

Although dioxane also generated a dendritic pore morphology, its features had different characteristics from cyclohexane- and camphene-based samples. The primary dendrite tips did not show clear four-fold symmetry and also had a tendency to form linear formations. The pores generated from the secondary dendrite arms also branched out at an approxmiately 45 degree angle from the primary dendrite.

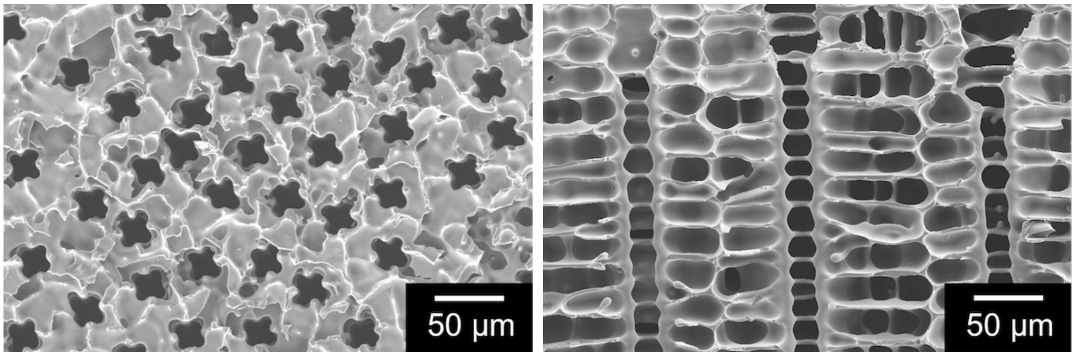

(a) Cyclohexane transverse (b) Cyclohexane longitudinal

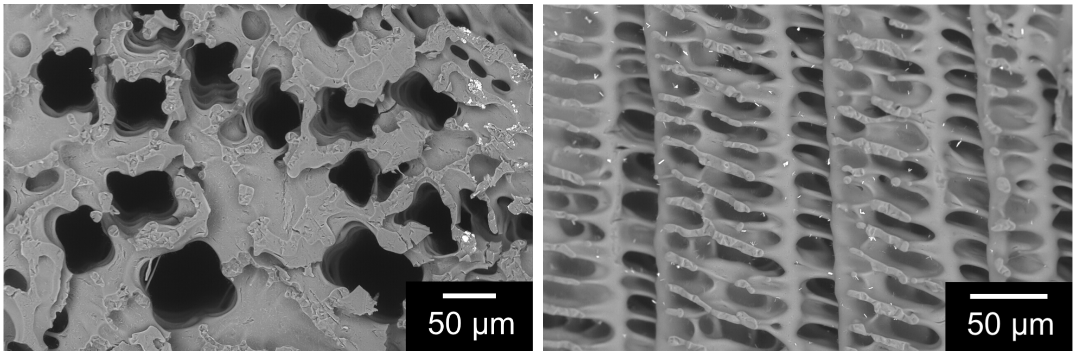

(c) Camphene transverse (d) Camphene longitudinal

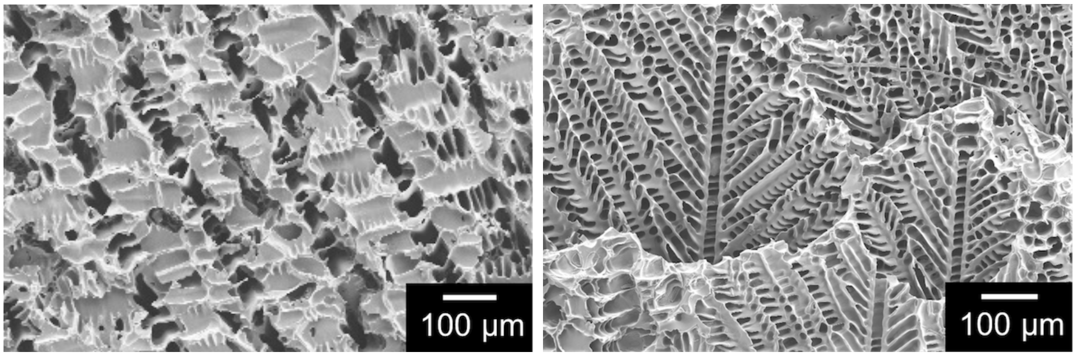

(e) Dioxane transverse (f) Dioxane longitudinal

Figure 3.7. SEM micrographs of an dendritic pore morphologies obtained by freeze casting with cyclohexane, camphene, and dioxane. Transverse and longitudinal views show dendrites growing along the temperature gradient.

Prismatic Pores

Figure 3.8 shows a prismatic pore morphology produced by freeze casting with t-butanol as the solvent. The prismatic morphology is characterized by features such as elongated pores and smooth walls which are created by needle-like crystals, particularly noticeable in the longitudinal view. Some faceting representative of TBA's rhombic crystal is observed in the transverse view, but the irregular pore morphology is characteristic of coalescence during freezing.[109,110] Instead of forming isolated prisms and channels which are enclosed by pore walls, these coalesced to form a more complicated and interconnected pore network.

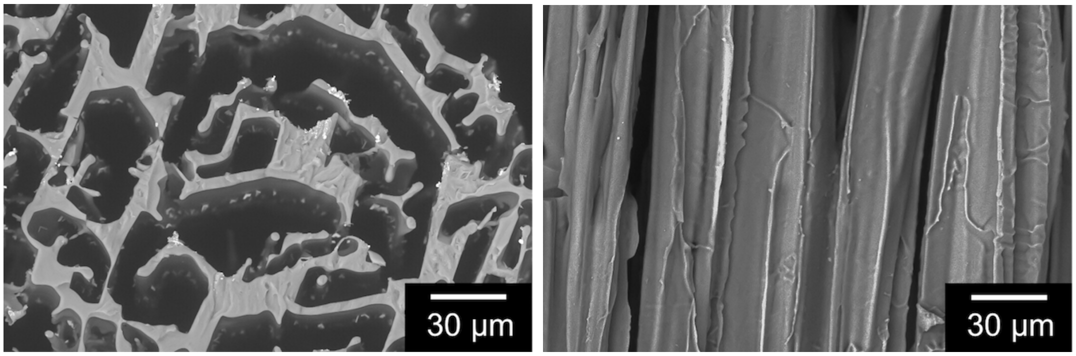

(a) t-Butanol transverse (b) t-Butanol longitudinal

Figure 3.8. SEM micrographs of a prismatic pore morphology obtained by freeze casting with t-butanol. Needle-like crystals create prisms with smooth walls.

Lamellar Pores

Lamellar pore morphologies are defined by a series of stacked two-dimensional plate-like structures. This pore morphology is commonly seen in freeze casting since they can be achieved from freezing aqueous suspension, as shown earlier in Figure 2.5(a). Here, we

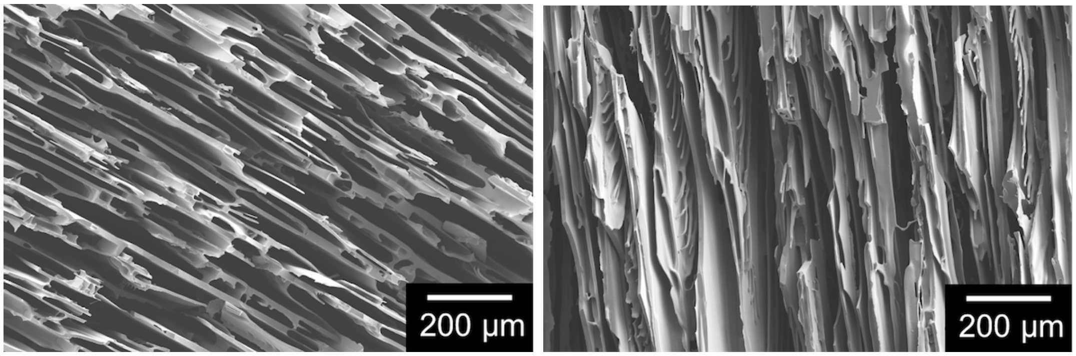

(a) Dimethyl carbonate transverse (b) Dimethyl carbonate longitudinal

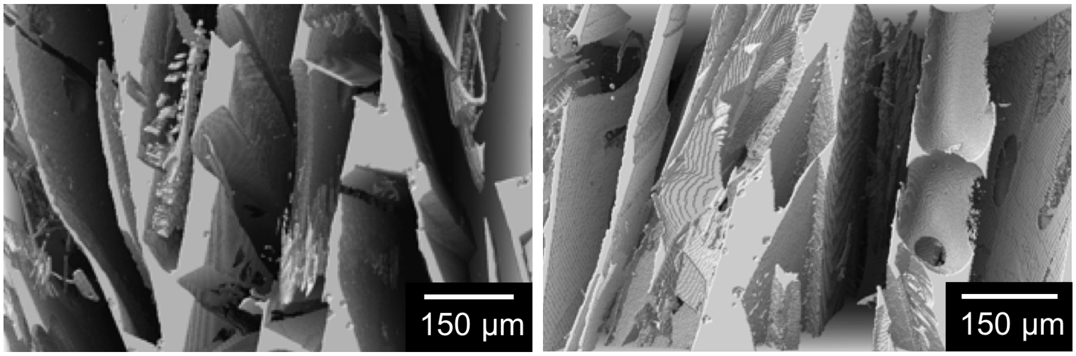

(c) p-Xylene transverse (d) p-Xylene longitudinal

Figure 3.9. Representative images of lamellar pore morphologies generated by freeze casting with (a,b) dimethyl carbonate (SEM) and (c,d) p-xylene (XCT). The lamellar structure is reminiscent of aqueous-based freeze casting.

also see that dimethyl carbonate and p-xylene can generate similar lamellar structures (Fig. 3.9). Although both solvents generated lamellar structures, their feature sizes are quite different. Dimethyl carbonate generated relatively fine lamellae, more similar to water, whereas p-xylene's lamellar structure was coarse and had a significantly larger wall thickness and pore spacing. Furthermore, at 20 wt.% polymer concentration, the thick lamellar walls cannot be fully formed and numerous structural defects are observed.

Consequently, samples freeze cast with p-xylene were very fragile even to the touch. Hence, images obtained from XCT are instead shown for p-xylene samples.

In order to gain a better comparison of the two lamellar structures, Figure 3.10 shows 3D reconstructed images of dimethyl carbonate and p-xylene samples made with 40 wt.% polymer concentration. This higher polymer concentration allows p-xylene to produce a more complete and continuous lamellar structure. Nevertheless, the lamellar thickness and spacing generated from p-xylene are still significantly larger and coarser than those from dimethyl carbonate.

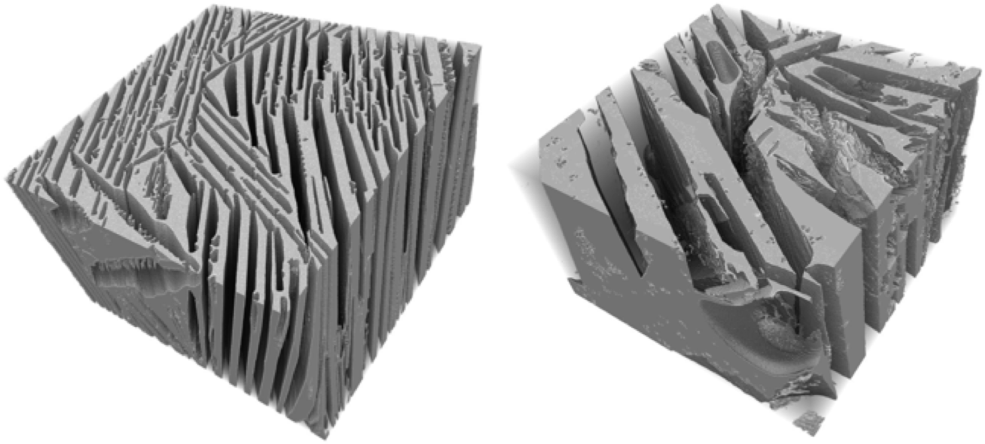

(a) Dimethyl carbonate (b) p-Xylene

Figure 3.10. 3D reconstructions of lamellar structures from 40 wt.% polymer samples using (a) dimethyl carbonate and (b) p-xylene as solvents. The images have a width and depth of 955 µm, and a height of 588 µm.

Additionally, while the lamellae may seem like flat platelets, images taken from a different angle (Fig. 3.11) show that side-branching can occur on the surface of the lamellae during solidification, creating finer microstructures. These features are predominantly observed with water and dimethyl carbonate, but less so with p-xylene.

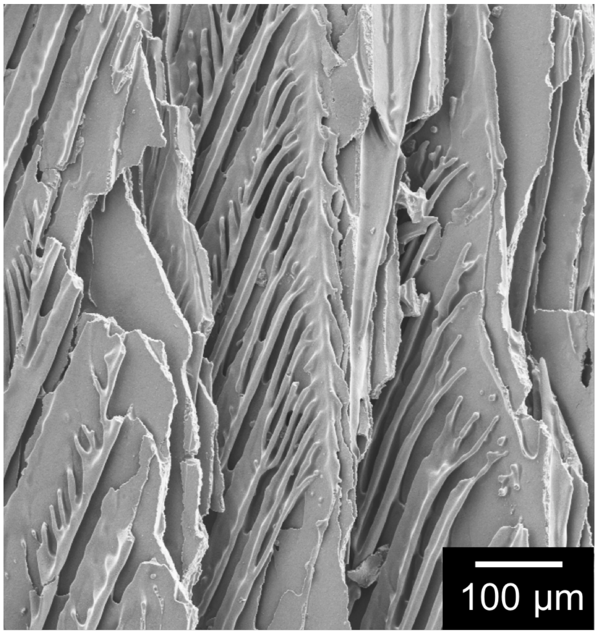

Figure 3.11. SEM micrograph of a lamellar pore structure generated by dimethyl carbonate, taken at a different angle to show ridges present on the sides of the lamellae.

Effects of Pore Morphology on Geometric Surface Area

Figure 3.12 shows the influence of various pore morphologies on the geometric specific surface area (SSA), calculated by performing a marching cubes algorithm in MATLAB using 3D data sets obtained from XCT experiments. Dendritic, prismatic, and lamellar pore morphologies produced from various solvents were compared, and a range of porosities were explored via changes in the polymer concentration. Each sample was solidified under identical conditions, by casting onto a cold surface set to -25 °C.

Normalizing the surface area by pore volume yields information regarding the feature size of the pores, with higher SSA representing smaller features and pore sizes, and vise-versa. Here, the SSA decreases with increasing porosity for all solvents used. This result is

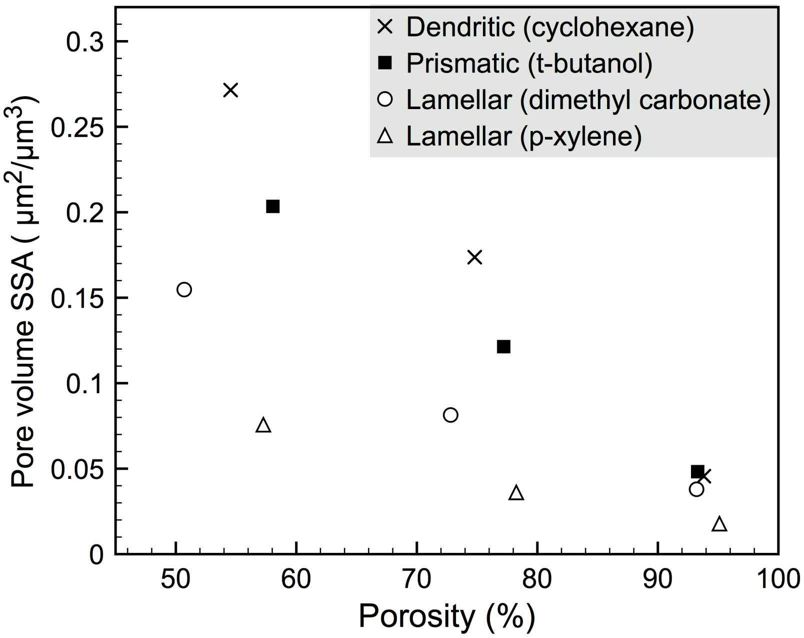

Figure 3.12. Pore volume-normalized geometric specific surface area of samples with dendritic, prismatic, and lamellar pore morphologies, produced with a range of porosities.

expected, as the higher porosity naturally produces larger pore sizes. More interestingly, a trend regarding the various pore morphologies is observed, with dendritic structures yielding higher SSA values than prismatic structures, and followed by lamellar structures. This trend correlates with the roughness of each microstructure, as the dendritic structure generates pore walls with numerous features, while prismatic and lamellar structures yield smooth and relatively featureless pore walls. Moreover, there is a significant difference between the two solvents producing lamellar structures, with dimethyl carbonate showing a higher SSA than p-xylene at a given porosity. This difference can be explained by the thicker lamellae and larger pore spacing produced from p-xylene shown earlier in Figure

3.10. From these results, it is apparent that differences in the pore morphology can influence the SSA of porous materials, by up to a factor of four to five.

3.3.4. Jackson α-factor and Solidification Microstructures

The Jackson α-factor was employed as a tool to correlate each solvent's interfacial anisotropy with the pore structures that were generated. As shown in Equation 2.2, the α-factor can be partitioned into two parts: a crystallographic term, η/Z, and an entropic term, $\mathrm{L}/(\mathrm{kT_m})$. While the crystallographic term ranges between 0.25 and 1, the entropic term can be calculated for each solvent to obtain a representative value for α, as shown in Table 3.3. Solvents are listed in order of increasing entropic terms. Recall from Section 2.2.3 that a low α-factor or entropic term generally implies atomically rough growth interfaces and interfaces without facets, whereas at high α values, faceted growth is often observed. Despite not being used in this study, water is also listed here as a reference since its lamellar structure is well-studied in aqueous suspension-based systems. As a supplementary test, optical micrographs of solidification microstructures obtained from directional solidification of various polymer-solvent solutions are also shown. Due to the significantly different thermal conditions the polymer solutions experience during optical microscopy and freeze casting, the resulting microstructures serve only as a guide rather than a direct comparison.

Beginning from solvents with relatively low entropic terms, we observed that cyclooctane (1.02), cyclohexane (1.15), and camphene (1.15) produced either isotropic or dendritic pore morphologies, both which are considered as non-faceted structures. These results agree with what is expected, as microstructures such as dendrites are often formed

Table 3.3. Enthalpy of fusion, calculated entropic term, and pore morphology for each solvent used, compared to water.

Solvent	Enthalpy of fusion (kJ/mol)	Entropic term	Pore morphology
Cyclooctane	2.41	1.02	Isotropic
Cyclohexane	2.68	1.15	Dendritic
Camphene	2.94	1.15	Dendritic
Water	6.01	2.65	Lamellar
tert-Butanol	6.70	2.71	Prismatic
Dioxane	12.30	5.21	Dendritic
Dimethyl carbonate	13.22	5.76	Lamellar
p-Xylene	17.12	7.18	Lamellar

from unstable solidification fronts where the interfacial anisotropy is low and diffusion effects are more dominant than crystallographic preferences. However, unlike the other solvents, cyclooctane, with the lowest entropic term of 1.02, produced a non-dendritic microstructure. Studies by Kobayashi et al. showed that while dendritic structures are preferred at low interfacial anisotropies, an adequate amount of anisotropy is nonetheless required for their formation.[111] In cases where the anisotropy is particularly low, a more disordered seaweed structure is often formed.[112] As confirmation of this, cyclooctane and cyclohexane polymer solutions were directionally solidified under an optical microscope and images of their solidification microstructures were recorded. Figure 3.13 shows that a seaweed structure is generated by a cyclooctane solution, while a cellular or dendritic structure is generated by cyclohexane. The isotropic pore structure obtained from cyclooctane, as viewed in cross-section, reflects this seaweed structure more accurately than the elongated features seen in cells or dendrites. Since a more directional solidification microstructure was observed with the pure cyclooctane solvent, the seaweed structure seen with the polymer solution is likely the result of a strong interaction between the polymer and the solid-liquid interface. In contrast, pure cyclohexane and cyclohexane solutions showed similar microstructures. Interestingly, the cellular growth behavior seen in Figure 3.13(b) not observed in freeze cast structures. This cellular structure can be attributed to the higher thermal gradient associated with the microscopy setup which could not be replicated during freeze casting (Fig. 2.13).

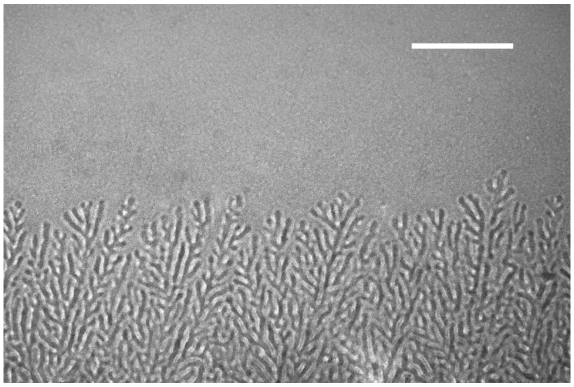

(a) Cyclooctane

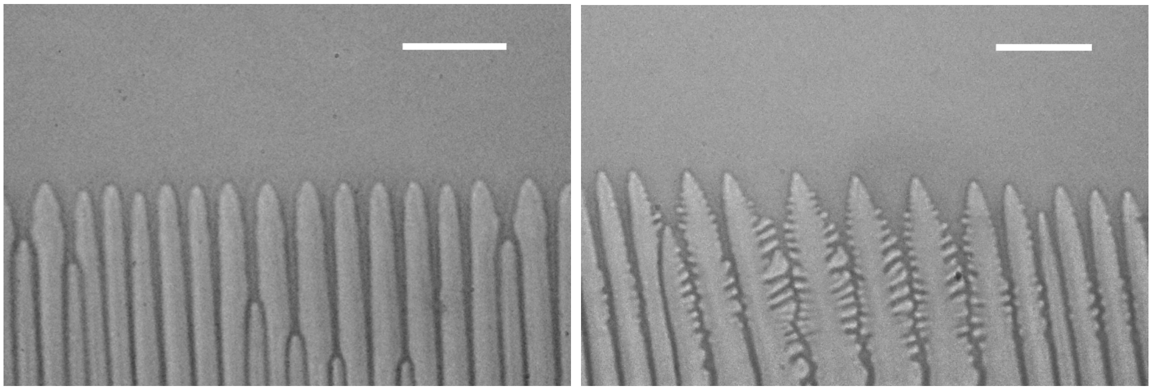

(b) Cyclohexane (Cellular)

(c) Cyclohexane (Dendritic)

Figure 3.13. Optical micrographs showing solidification microstructures for preceramic polymer solutions with (a) cyclooctane and (b,c) cyclohexane as solvents. Scale bars = 150 µm.

As the entropic term increases, faceted solidification microstructures become prevalent. At an entropic term of 2.71, t-butanol produced a prismatic pore morphology which is considerably different from the rounded morphologies observed from solvents with lower entropic factors (cyclooctane, cyclohexane, and camphene) discussed earlier. Figure 3.14 shows an optical micrograph of a solidifying t-butanol solution, where the needle-like structures used to describe the prismatic morphology are clearly seen. This structure is notably unlike cells due to its faceted features and non-uniform growth front. Again, this result correlates well with what is expected according to the Jackson α-factor.

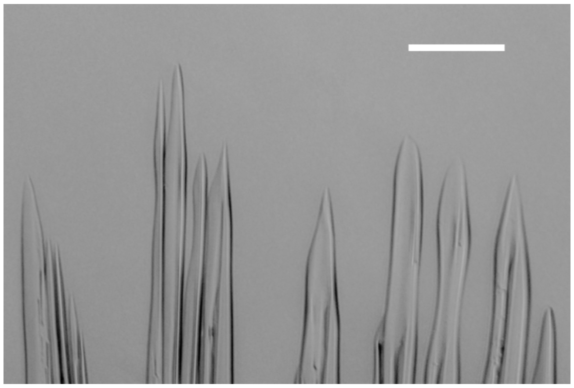

Figure 3.14. Optical micrographs showing solidification microstructures for t-butanol polymer solution. Scale bar = 150 µm.

While the Jackson α-factor has shown good correlation with the various pore morphologies thus far, an anomaly is seen with water and dioxane, where water generates a faceted lamellar structure despite its relatively low entropic term and dixoane's relatively high entropic term of 5.76 produced a non-faceted dendritic structure. Understandably, these solvents belong in the middle of the spectrum where exceptions can exist due to uncertainty in the crystallographic term. Nevertheless, minor differences exist between dioxane's dendrites and dendrites formed by solvents with lower entropic terms (i.e. cyclohexane and camphene). In addition to the secondary dendrite arms growing at an angle, dioxane's dendritic pore structure also has a tendency to form a linear, two-dimensional configuration similar to a lamellar structure (Fig. 3.7(e)). These are features that can be attributed to crystallographic preferences exerting an influence on the solidification microstructure generated. Additionally, optical micrographs of solidifying dioxane polymer solutions (Fig. 3.15) show a range of morphologies being formed, from cells to dendrites, with certain cells showing signs of instability with growing side-branches. The angled secondary pores seen in Figure 3.7(f) can also be observed here as most dendrites grow at an acute angle compared to cyclohexane solutions (Fig. 3.13(c)).

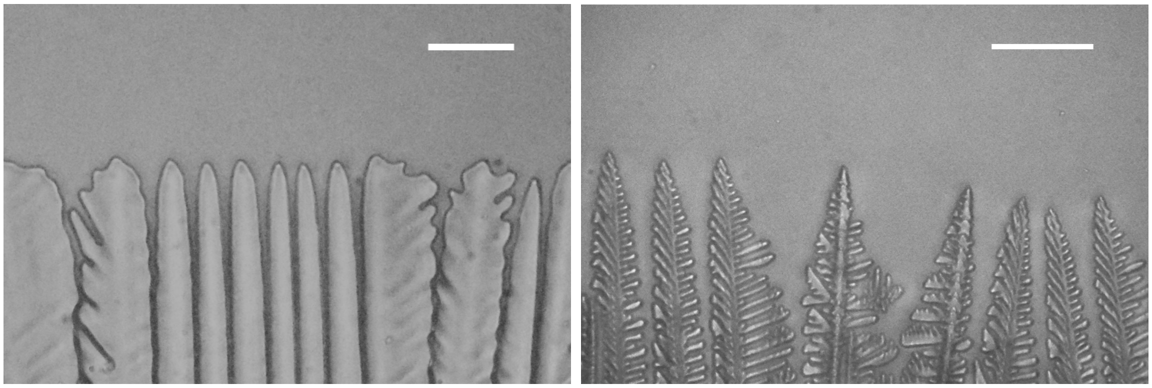

(a) Dioxane (Cellular)

(b) Dioxane (Dendritic)

Figure 3.15. Optical micrographs showing solidification microstructures of solidifying dioxane polymer solutions; (a) cellular and (b) dendritic microstructures are produced. Scale bars = 150 µm.

Finally, at the high end of the spectrum, dimethyl carbonate and p-xylene with entropic terms of 5.76 and 7.18, respectively, produced lamellar structures representative of highly faceted crystal growth. The two-dimensional, high aspect ratio feature of a lamella is proof of the strong anisotropy, as growth is preferential in a particular direction and comparatively slow in the orthogonal direction. Figure 3.16 shows examples of solidification microstructures from dimethyl carbonate solutions. Similar to many other solvents, several microstructures are observed with optical microscopy, including highly faceted and ordered lamellae with flat sides, as well as lamellae with side-branching. Pore structures matching both these solidification types were shown earlier in Figures 3.9(a) and 3.11. The fact that both types of solidification microstructures can be observed in a single sample, under relatively unchanged temperature conditions, shows that the transitional regime is within commonly used freeze casting conditions, unlike cyclohexane and dioxane.

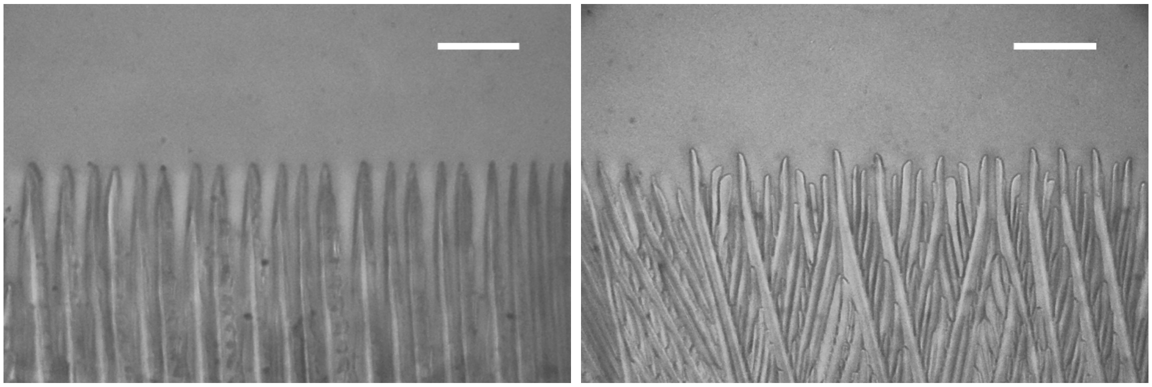
(a) Dimethyl carbonate (Flat)
(b) Dimethyl carbonate (Branched)

Figure 3.16. Optical micrographs showing solidification microstructures for preceramic polymer solutions with (a) cyclooctane and (b,c) cyclohexane as solvents. Scale bars = 150 µm.

Overall, the pore structures and optical micrographs show good agreement with the solidification behavior expected based on the Jackson α-factor and the entropic terms listed in Table 3.3. As the entropic term increases, so too does the expected anisotropy, resulting in microstructures gradually changing from non-faceted to faceted. However, certain exceptions do exist, particularly with solvents in the intermediate range of the spectrum (i.e. water and dioxane). This inconsistency demonstrates that the Jackson α-factor is not always an absolute measure of the magnitude of the solid-liquid interfacial energy, especially if the crystallographic term is not known or taken into consideration. Nevertheless, the results obtained here, as well as in other sources,[56] indicate that the α-factor is a reasonable guide to forecast the type of solidification microstructure that can be expected during freeze casting.

3.3.5. Freezing Front Velocity

The freezing front velocity of freeze cast samples was measured according to Section 3.2, however, this was applicable only to certain well-behaved solvents. Figure 3.17 show images of cyclohexane and t-butanol polymer solutions midway through freeze casting. Here, cyclohexane displayed ideal freeze casting behavior, with a flat and clearly defined freezing front that allowed for tracking. On the other hand, the t-butanol solution experienced a considerable amount of undercooling, prompting highly unstable crystal growth upon nucleation. In this latter case, the freezing front velocity cannot be tracked. Table 3.4 shows which solvents were considered suitable for freezing front tracking and which were not.

Figure 3.18 shows how the freezing front velocity changes throughout the height of the sample depending on the cooling profile used. Since the freezing front velocity affects the pore size generated, a constant velocity is desired to obtain a structurally homogeneous sample. While many studies freeze cast by pre-chilling the casting surface to a low temperature (i.e. quenching), results shown here indicate that a range of pore sizes would

(a) Cyclohexane (b) t-Butanol

Figure 3.17. Freezing front images for (a) cyclohexane and (b) t-butanol polymer solutions midway through freeze casting

be created as the freezing front velocity diminishes drastically from the bottom of the sample to the top. Ramping the temperature down at a linear rate shows a significant improvement, however a decreasing velocity is still observed as the height increases. A relatively constant freezing front velocity was successfully produced by using a parabolic cooling profile where the temperature was decreased at an accelerating rate in order to

Table 3.4. Acceptability of each solvent for freezing front velocity tracking. Solvents which solidified with a flat and clear freezing front were deemed eligible, while solvents which displayed a high degree of undercooling were ineligible.

Solvent	Freezing front tracking
Cyclooctane	✓
Cyclohexane	✓
Camphene	×
tert-Butanol	×
Dioxane	✓
Dimethyl carbonate	✓
p-Xylene	×

compensate for the increasing sample thickness, which effectively increases the thermal resistance.

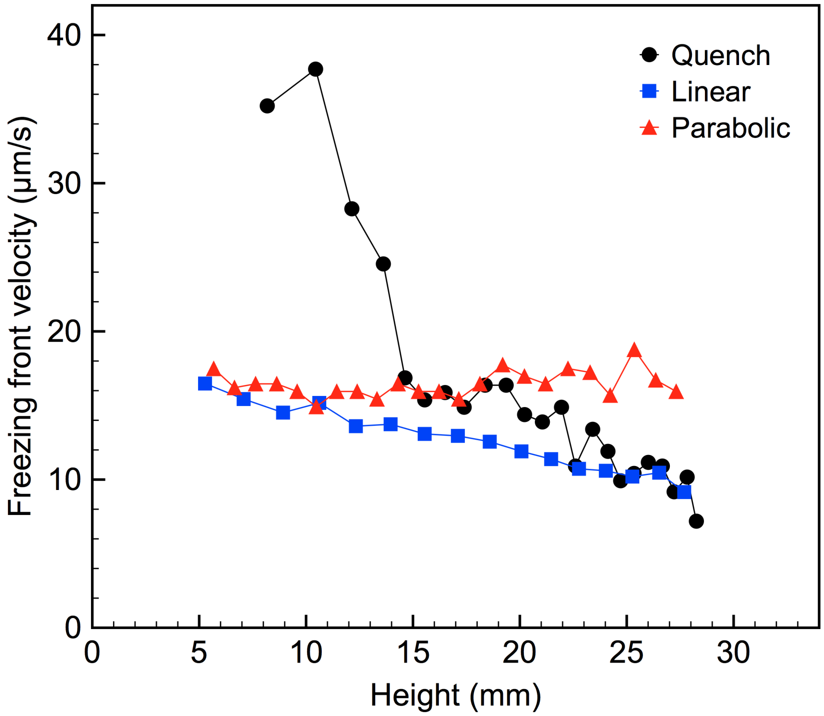

Figure 3.18. Freezing front velocity along sample height under various cooling profiles: quenching, linear ramping, and parabolic ramping

Due to its ideal solidification characteristics, cyclohexane was used as the model solvent to investigate the effects of freezing front velocity on pore size. Figure 3.19 shows the pore size distribution of cyclohexane-based samples made with 20 wt.% polymer concentration, solidified at freezing front velocities of 5 and 15 µm/s. Interestingly, cyclohexane shows a bimodal pore size distribution attributable to its dendritic structure. Primary dendrites generate the larger pores, while secondary dendrite arms generate smaller pores. The secondary dendrite arms however account for a larger portion of the pore volume since numerous secondary dendrite arms are grown from a single primary dendrite. The pore sizes for both types of dendrites are affected similarly by a change in freezing front velocity, where a slower freezing front velocity results in larger ice crystals, and consequently larger pores. Reducing the freezing front velocity from 15 µm/s to 5 µm/s, the pore diameter of the primary dendrites increased by roughly 15 µm and the secondary dendrite arms by roughly 10 µm. Overall, the median pore diameter calculated by MIP increased from 16.7 µm to 26.8 µm, a change of 60%.

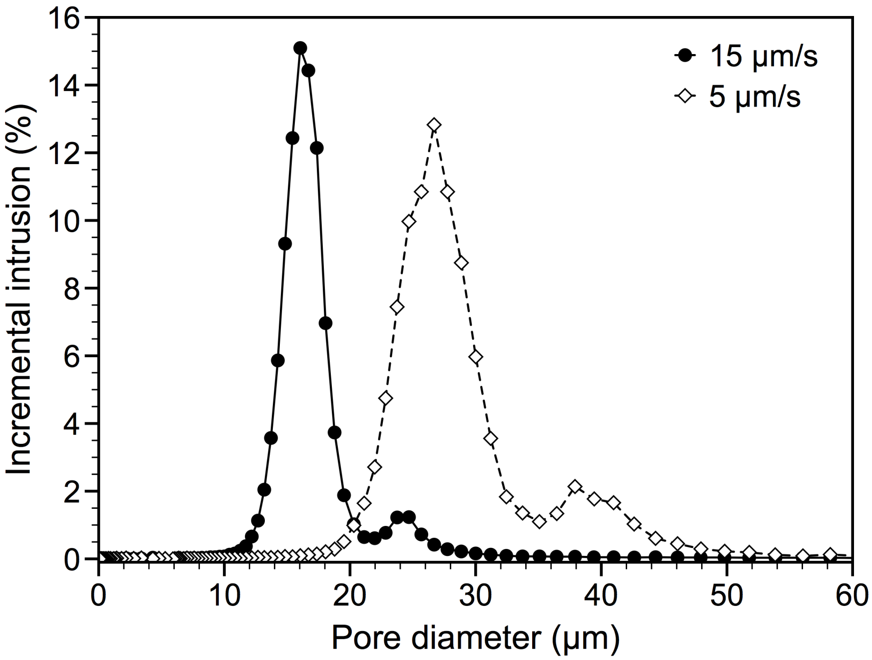

Figure 3.19. Effect of freezing front velocity on the pore size distribution obtained by MIP of cyclohexane-based SiOC structures. Samples were made with 20 wt.% polymer concentration and freeze cast at 5 and 15 µm/s.

Theoretically, changes in the type of solidification morphology can be achieved based on the freezing conditions. Particularly, cells can grow instead of dendrites under low solidification velocities and high temperature gradients, as shown earlier with optical microscopy in Figure 3.13. In this study, a freezing front velocity as low as 3 µm/s was measured with cyclohexane, however dendrites were still observed to be the prevalent morphology. This is likely due to the high thermal gradient required at the solid-liquid interface for cells to be formed (Fig. 2.13). Since most current freeze casting setups naturally induce a low thermal gradient, as the temperature is controlled at the ends of the sample rather than at the interface, this transition has yet to be observed in freeze casting. More novel casting setups with improved control of the solidification conditions may be required to achieve this transition.

3.3.6. Polymer Concentration

Figure 3.20 shows how changes in the polymer concentration, from 10 to 40 wt.%, can affect the pore size of cyclohexane-based samples. All samples were frozen at the same freezing front velocity of 15 µm/s to make pore sizes comparable. As expected, higher polymer concentrations yield smaller pore sizes since the lower pore fraction limits the space available for pores to form. Additionally, it is also possible that higher polymer concentrations contribute to an increase in the viscosity, consequently lowering the diffusion coefficient and resulting in a smaller instability wavelength and feature size (Eq. 2.1). However, unlike the definite decrease in pore fraction, the change in the diffusion coefficient, as well as its effects, have not been quantified. Interestingly, the change in pore size is noticeably more pronounced at lower polymer concentrations, with the median pore diameter of 10 wt.% and 20 wt.% samples reducing by 9.5 µm, from 25.9 to 16.4 µm (37% decrease), whereas 30 wt.% and 40 wt.% samples saw a reduction of only 2 µm, from 10.7 to 8.7 µm (19% decrease). The open porosity achieved from each polymer concentration is also listed in Table 3.5 for reference.

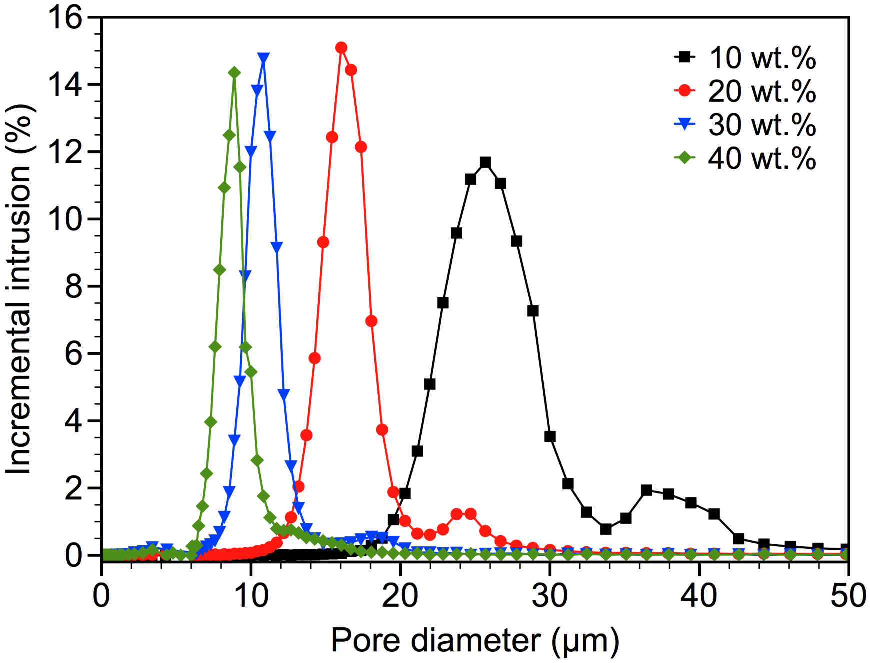

Figure 3.20. Pore size distribution data obtained by MIP showing the effect of polymer concentration on the pore size of cyclohexane-based SiOC structures freeze cast at 15 µm/s.

Table 3.5. Open porosity of cyclohexane samples made with varying polymer concentrations, determined by the Archimedes method.

Polymer concentration (wt.%)	Open porosity (%)
10	87.9
20	77.3
30	61.6
40	52.6

Additionally, Figure 3.21 compares both processing variables (i.e. freezing front velocity and polymer concentration) and their impact on the pore size. Results show that while both methods are able to significantly affect the pore size, samples with lower polymer concentrations again proved to be more sensitive to the changes in the freezing front velocity. Between freezing front velocities of 5 and 15 µm/s, samples with 10 wt.% polymer experienced a change in median pore size of 17.2 µm, a 39% change, while 30 wt.% samples varied by only 3.3 µm, a 23% change. It should also be noted that variations in the polymer concentration are linked to changes in properties such as open porosity and bulk density, however controlling the freezing front velocity enables the pore size to be adjusted independent of these properties.

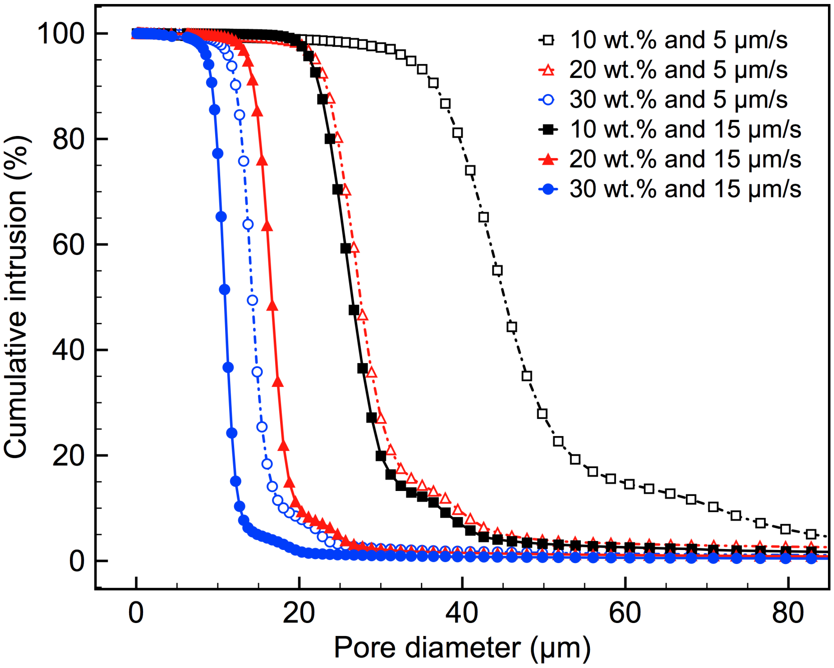

Figure 3.21. Cumulative intrusion data obtained by MIP comparing the effect of polymer concentration and freezing front velocity on the pore size of cyclohexane-based SiOC structures.

A significant change in the polymer concentration, and consequently pore fraction, can also alter the appearance and connectivity of various pore structures. Figure 3.22 shows how pore structures of cyclohexane and t-butanol samples change between 5 wt.% and 40 wt.% polymer concentrations (∼90% and 60% porosities, respectively). Recall from Section 3.3.3 that cyclohexane and t-butanol at 20 wt.% polymer concentration produced dendritic and prismatic pore morphologies, respectively.

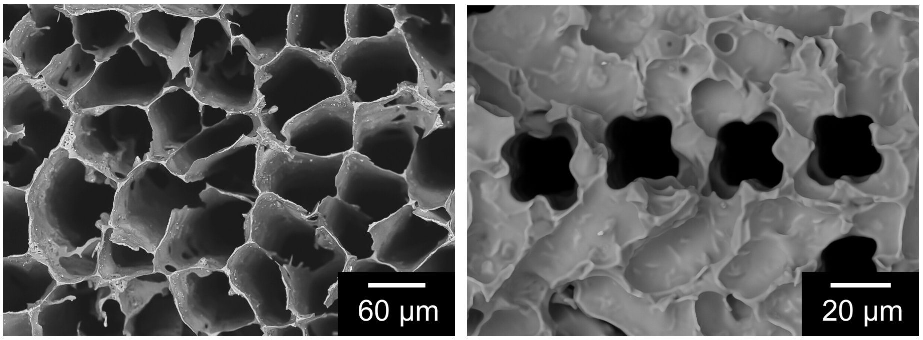

(a) Cyclohexane- 5 wt.% polymer (b) Cyclohexane- 40 wt.% polymer

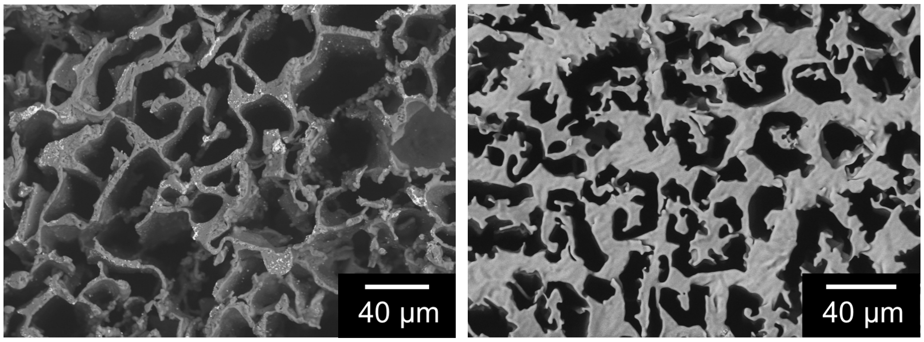

(c) t-Butanol- 5 wt.% polymer (d) t-Butanol- 40 wt.% polymer

Figure 3.22. SEM micrographs of (a,b) cyclohexane and (c,d) t-butanol samples showing changes in pore structure and connectivity due to significant changes in the polymer concentration.

Cyclohexane samples made with 5 wt.% polymer show closely packed pore channels with thin walls, similar to a honeycomb structure. While samples with higher polymer concentrations had thick walls surrounding each dendrite, the lack of solids available here results in limited solute rejection in the transverse direction and influences how the polymer is redistributed. Here, the characteristic four-fold symmetry of the secondary arms becomes less defined (Fig. 3.22(a)). However, when viewed from the longitudinal direction, it is clear that dendrites were generated even at 5 wt.% polymer concentration (Fig. 3.23). On the other hand, secondary dendritic arms are clearly seen in cyclohexane samples with 40 wt.% polymer concentration, as they have identical dendritic features to samples made at 20 wt.% polymer, but with decreased pore diameters.

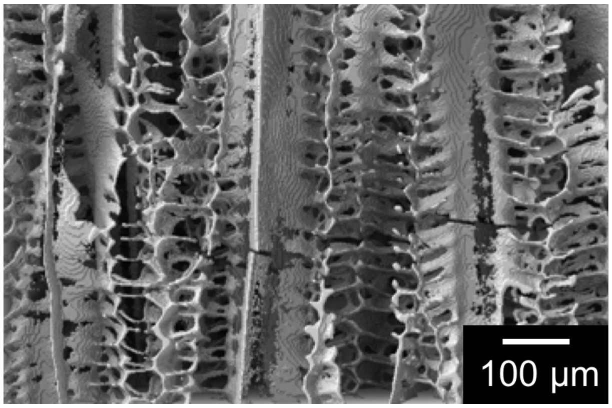

Figure 3.23. XCT image of the longitudinal view of a 5 wt.% polymer concentration made with cyclohexane as a solvent. Features from the secondary dendrite arms are clearly present despite not being visible from the transverse direction.

For TBA samples, those made with 5 wt.% polymer have thinner walls when compared to 20 wt.% samples, but similarly possess a highly irregular pore network with channels which are highly interconnected. However, samples made with 40 wt.% polymer contained enough polymer to form individual isolated channels, significantly reducing the interconnectivity of the pore structure.

Results show that changes in polymer concentration had an affect on properties such as pore fraction, pore diameter, and wall thickness. Pore size of samples made with lower polymer concentrations were more sensitive to changes in the polymer concentration as well as freezing front velocity. While structural differences were observed across varying polymer concentrations, characteristic features of certain pore morphologies such as dendritic arms and prismatic channels were preserved through a wide range of polymer concentrations, indicating that the type of solidification microstructure generated remained unchanged.

3.4. Conclusions

Fundamental concepts behind freeze casting with preceramic polymers were explored in this chapter. Results obtained from these studies can be roughly divided into two parts: general characterization of the physical and chemical characteristics of the MK preceramic polymer and the polymer-derived SiOC ceramic was first performed, followed by experiments aimed to control the pore structure during freeze casting. FTIR and XRD spectra showed that a fully amorphous ceramic SiOC structure was obtained via pyrolysis at 1100 °C. Through density measurements, the bulk density and open porosity of freeze cast SiOC were shown to range from from roughly 0.15 to 1.20 g/cm^3, and 45 to 95%, respectively, with negligible amounts of closed porosity. Finally, polymer-solvent phase diagrams constructed for four solvents showed a steady decrease in the liquidus temperature and freezing points as the polymer concentration increased, as expected from the presence of solutes. The natural freezing point was also found to be consistently lower than the agitated freezing point. However, the undercooling observed with cyclooctane and lack of undercooling from dimethyl carbonate contradicts with their Jackson-α factors as well as the pore morphologies produced from each solvent.

Solvent choice, freezing front velocity, and polymer concentration were used as processing parameters to control the pore structures generated from freeze casting. A total of seven different organic solvents were freeze cast to obtain porous SiOC ceramics with four distinct types of pore morphologies: isotropic, dendritic, prismatic, and lamellar. The Jackson-α factor was introduced as a method to correlate each solvent's enthalpy of fusion and interfacial anisotropy with the various solidification microstructures generated. Results showed good agreement with theory, where solvents with low entropic terms, or interfacial anisotropy, exhibited non-faceted structures, while those with high entropic terms generated faceted structures. Next, the effect of freezing front velocity on pore size were investigated. While some solvents, including cyclohexane, showed ideal freezing front behavior, certain solvents produced significant undercooling which was detrimental to measurement of the freezing front velocity. Results show that the pore size of cyclohexane samples was effectively increased by reducing the freezing front velocity from 15 to 5 µm/s. Polymer concentration was also shown to have a significant impact on the pore size of cyclohexane samples, while also altering the structural details of cyclohexane and t-butanol samples. The shape and interconnectivity of the pore structures were affected at very high and low polymer concentrations. However, despite large variations in the freezing front velocity and polymer concentration, a change in pore morphology created from each solvent could not be achieved (e.g. from dendritic to cellular pores), as cyclohexane and t-butanol consistently produced dendritic and prismatic pores, respectively.

CHAPTER 4

A Comparison Between Suspension- and Solution-based Freeze Casting

Material in this chapter is reproduced in part from ”Suspension- and solution-based freeze casting for porous ceramics’, M. Naviroj et al.; *Journal of Materials Research*, in press.

4.1. Introduction

While Chapter 3 has shown that freeze casting with preceramic polymer solutions is a viable alternative to the more conventional ceramic suspensions, differences in behavior between a homogeneously dissolved polymer solution and a particulate suspension can be significant and should be addressed. For example, various processing parameters studied in suspension-based freeze casting such as particle size and shape are not applicable to solution-based freeze casting. Instead, new considerations arise in solution freeze casting, including issues such as polymer-solvent interactions and solvent compatibility. These differences not only affect the processing parameters, but also the solidification behavior, which in turn determines how the pores are formed. In order to gain a better understanding of both techniques, differences between these two systems must be investigated.

In this work, suspension- and solution-based samples are freeze cast under equivalent conditions with the goal of establishing how pore structure is affected by both process and casting medium. We chose four different organic solvents, namely, cyclooctane, cyclohexane, dioxane, and dimethyl carbonate, as they showed ideal solidification behavior (Table 3.4) and could provide a range of pore structures, from non-faceted to faceted (Table 3.3). Technological implications that arise from the differences between the two systems are also discussed.

4.2. Experimental Methods

4.2.1. Sample Preparation

Suspensions

Ceramic suspensions were made by dispersing α-Al_2O_3 (HP-DBM, $d_{50} = 350$ nm, Baikowski Inc., Malakoff, TX, USA) in cyclooctane, cyclohexane, dioxane, or dimethyl carbonate at a solids loading of 15 vol.% in order to target porosities of $\sim$70%. Al_2O_3 was chosen due to its wide use in freeze casting studies and good compatibility with commercially available dispersants. Dispersants were added to each solvent at a concentration of 5 wt.% (of solids) and sonicated for 10 minutes. Hypermer KD-1 was used for dioxane and dimethyl carbonate while Hypermer KD-4 (Croda Inc., Edison, NJ, USA) was used for cyclooctane and cyclohexane based on the polarity of the solvents. Suspensions were then ball milled overnight to achieve a stable suspension prior to freeze casting.

Solutions

Preceramic polymer solutions were made by dissolving MK powder in cyclooctane, cyclohexane, dioxane, or dimethyl carbonate at a solids loading of 17 vol.%, also to obtain porosities of ∼70%. After the polymer was fully dissolved, Geniosil GF 91 was added as cross-linking agent at a concentration of 1 wt.% of the solution prior to freeze casting.

Freeze casting

The freeze casting setup and procedure used in this study were as described in Section 3.2.2.

In order to produce comparable samples, a constant freezing freezing front velocity of 15 µm/s was chosen for all samples. However, while freezing front velocity tracking was possible for the transparent solution-based samples, suspension-based samples were opaque due to the presence of alumina particles (Fig. 4.1). Consequently, solution-based samples were used to determine the temperature profiles required to obtain a constant freezing front velocity of 15 µm/s for each solvent. These temperature profiles were then used to solidify both solution and suspension-based samples. Due to the freezing point depression caused by dissolved solutes in polymer-based samples, suspension-based samples are expected to experience a freezing front velocity that is slightly higher than solution-based samples. However, these differences were neglected. Finally, Al_2O_3 samples were sintered in air at 1600 °C for 4 h, ramping at 5 °C/min, and preceramic polymer samples were pyrolyzed in argon at 1100 °C for 4 h, ramping at 2 °C/min.

4.2.2. Characterization

Pore structures from both processing methods were observed using a SEM (Zeiss 1550VP, Carl Zeiss AG, Oberkochen, Germany). Each sample was sectioned in both transverse (perpendicular to the freezing direction) and longitudinal (parallel to the freezing direction) orientations using a diamond saw. Transverse cross sections were obtained 5 mm from the bottom of each sample, with initial sample heights being roughly 20 mm. Longitudinal cross sections were obtained at the widest point in the cylinder cross-section. The pore size distribution and median pore size of each sample were characterized using MIP.

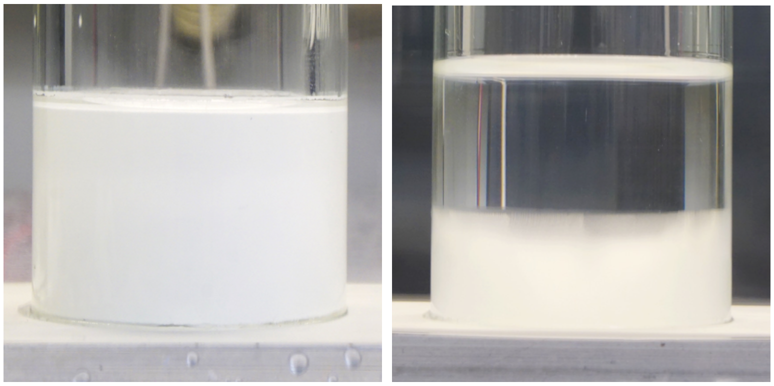

(a) Alumina suspension (b) Cyclohexane solution

Figure 4.1. Images comparing visibility of the freezing front during freeze casting of (a) suspension- and (b) solution-based samples.

4.3. Results and Discussion

4.3.1. Pore Morphology Comparisons from Suspension- and Solution-based Freeze Casting

Figure 4.2 shows the pore structures obtained by freeze casting alumina suspensions with the four organic solvents, in both transverse and longitudinal directions. Images show that cyclooctane suspensions produce a highly isotropic structure, with no differences between the transverse and longitudinal views (Figs. 4.2(a), 4.2(b), respectively) despite

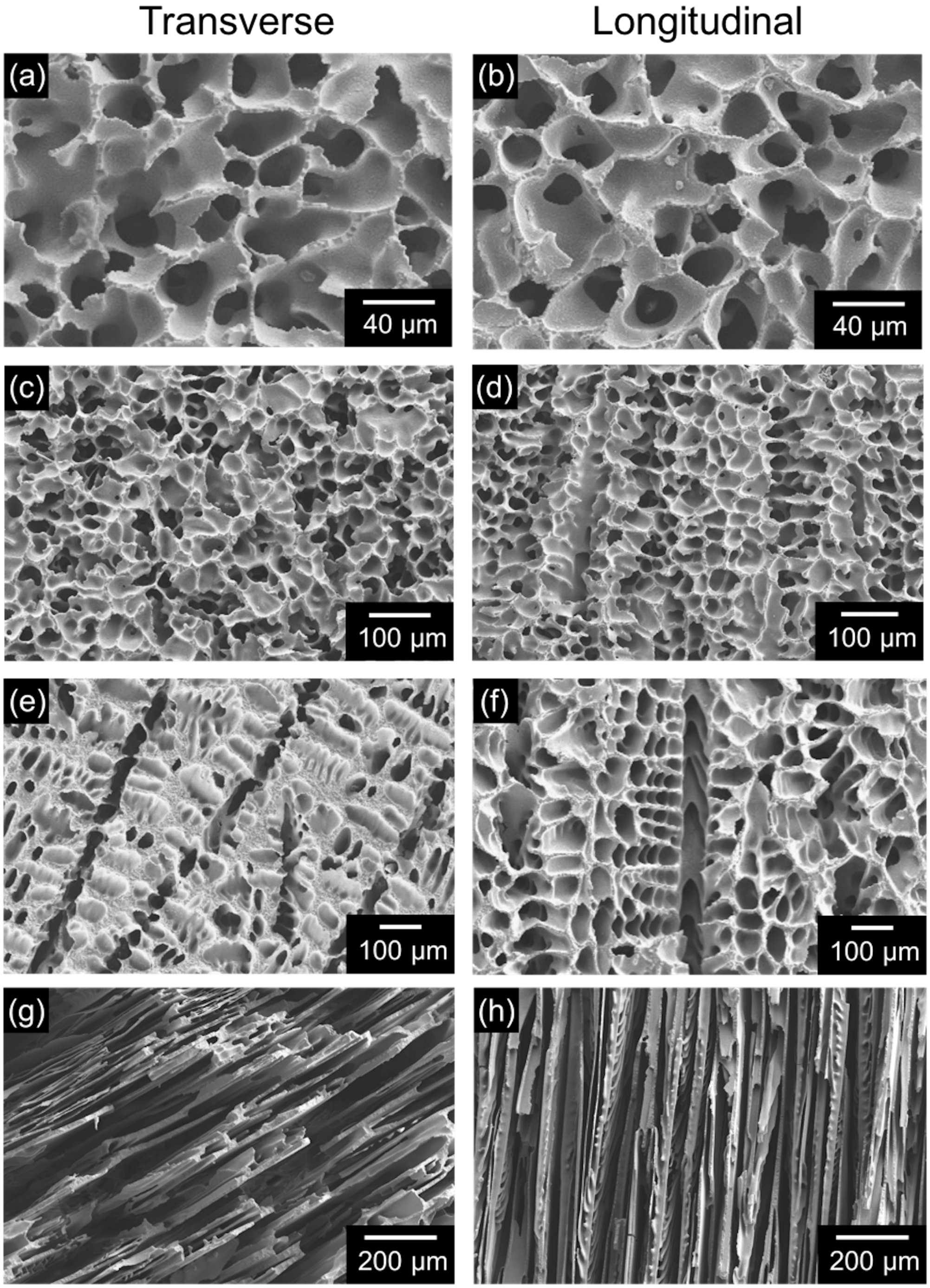

Figure 4.2. Suspension-based freeze-cast pore structures of cyclooctane (a,b), cyclohexane (c,d), dioxane (e,f), and dimethyl carbonate (g,h) based samples in both transverse (a,c,e,g) and longitudinal views (b,d,f,h) for 70% porosity Al_2O_3.

the thermal gradient applied to achieve directional solidification. Cyclohexane suspensions (Figs. 4.2(c), 4.2(d)) yield a similarly isotropic structure. Although there are some vertical features that can be seen in the longitudinal view due to directional solidification, they are relatively difficult to distinguish. With dioxane suspensions, dendritic features start to become discernible. Rows of dendrites are seen in the transverse view (Fig. 4.2(e)), while primary dendrites are seen growing upward in the longitudinal views (Fig. 4.2(f)). Finally, dimethyl carbonate suspensions generate a lamellar structure as seen in Figures 4.2(g) and 4.2(h). This lamellar structure is reminiscent of porous structures obtained via freeze casting of aqueous suspensions. The structure is also highly directional due to the temperature gradient applied during solidification.

In comparison, Figure 4.3 shows the pore structures obtained in SiOC by freeze casting preceramic polymer solutions. While cyclooctane solutions (Figs. 4.3(a), 4.3(b)) produce a highly isotropic and foam-like structure very similar to its suspension counterpart, a drastic change in pore structure is observed with cyclohexane samples. With cyclohexane solutions, the transverse view (Fig. 4.3(c)) shows clearly defined dendrites having pinched secondary arms. The longitudinal view (Fig. 4.3(d)) shows pores generated by the secondary dendrite arms, as well as the structure's high degree of anisotropy owing to the applied temperature gradient. Additionally, a considerable change in pore structure is also seen with dioxane solutions (Figs. 4.3(e), 4.3(f)). While the suspension-based samples did show some dendritic features and directionality, the dendrites seen in Figure 4.3(f) show much greater directionality compared to those seen in Figure 4.2(f). In contrast to cyclohexane where secondary dendrite arms grew orthogonal to the primary dendrites, dioxane's secondary dendrite arms grow upward at an angle of approximately 45 degrees

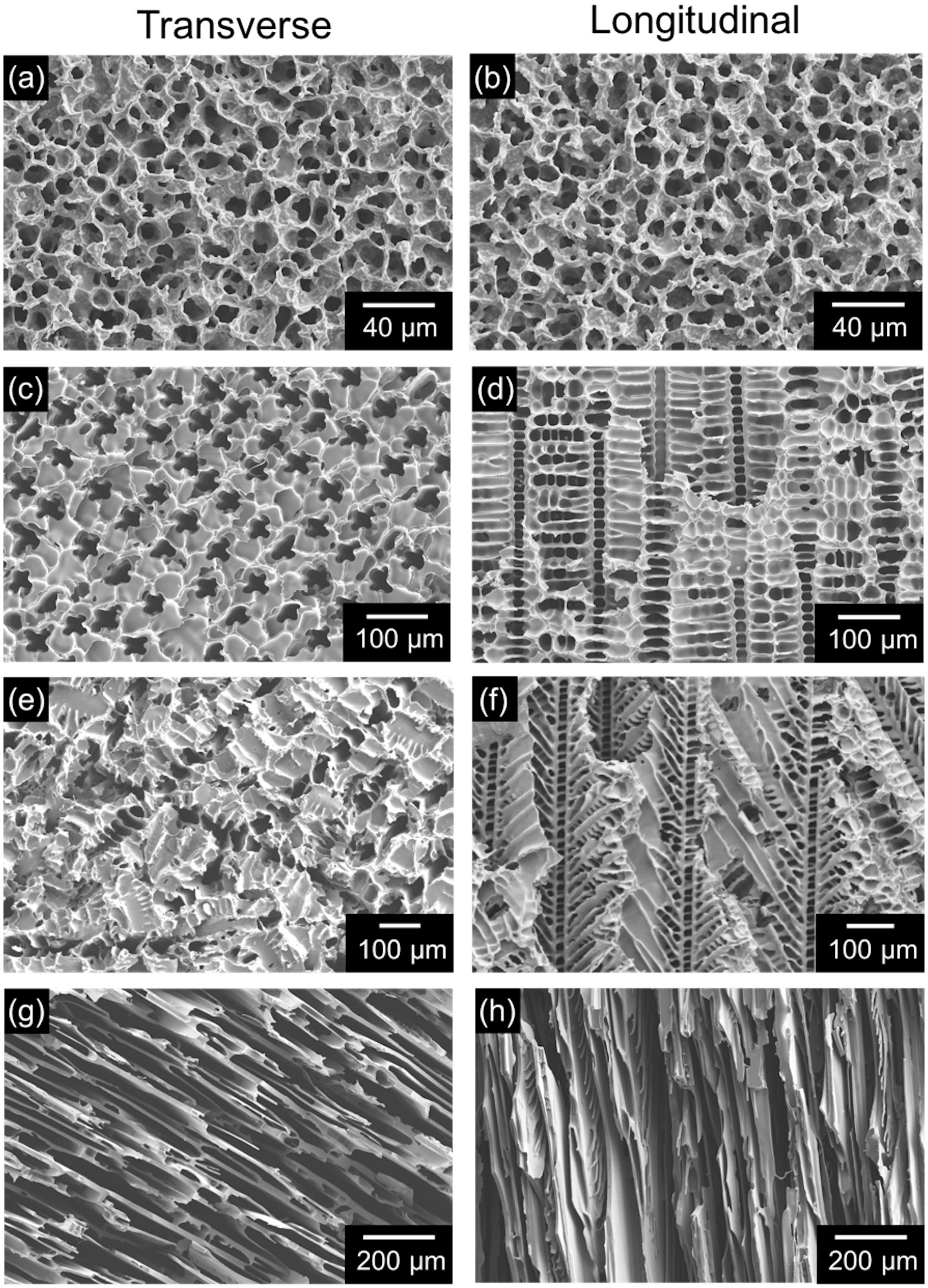

Figure 4.3. Solution-based freeze-cast pore structures of cyclooctane (a,b), cyclohexane (c,d), dioxane (e,f), and dimethyl carbonate (g,h) based samples in both transverse (a,c,e,g) and longitudinal views (b,d,f,h) for 70% porosity SiOC.

respect to the primary growth direction. Lastly, dimethyl carbonate solutions generated a lamellar structure (Figs. 4.3(g), 4.3(h)) almost identical to its suspension-based counterpart.

Furthermore, the pore wall surface morphology is also different between samples made from the two systems. Figure 4.4(a) shows a rough wall surface with visible alumina grains attributable to the sintering and coarsening of fine alumina particles. On the other hand, Figure 4.4(b) shows a smooth pore wall surface from SiOC samples. Homogeneous dissolution of a polymeric solution, along with the transformation of a preceramic polymer into an amorphous ceramic via pyrolysis, yields the glassy surface in contrast to the polycrystalline surface arising from suspension-based processing of ceramics.

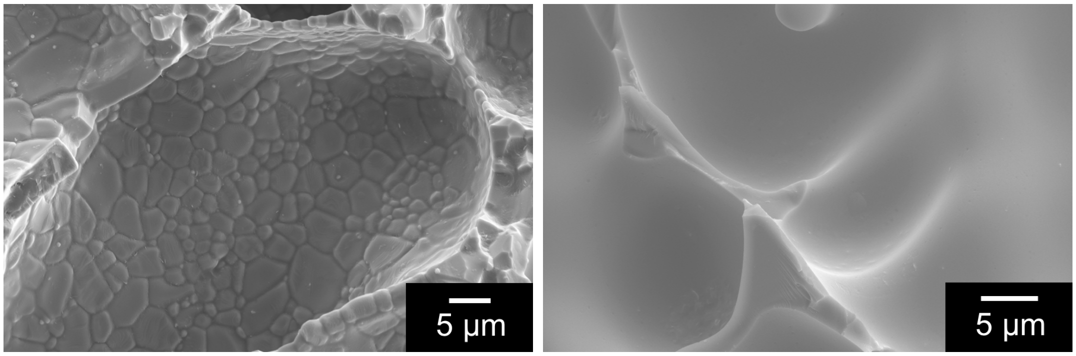

(a) Alumina suspension (b) Cyclohexane solution

Figure 4.4. Surface morphology of (a) sintered suspension-based alumina samples and (b) pyrolyzed solution-based preceramic polymer samples freeze cast with cyclohexane.

Overall, significant differences in pore structures are seen between suspension- and solution-based samples when cyclohexane and dioxane were used as solvents, with dendritic features emerging in the solution-based samples. In contrast, pore structures from cyclooctane and dimethyl carbonate samples exhibited little difference between the two systems.

It is hypothesized that the difference in pore structure from cyclohexane and dioxane is due to the presence or absence of suspended particles. Although it is possible that the addition of a solute such as the preceramic polymer to the solvent might influence the solidification microstructure due to changes in the interfacial anisotropy,[113] it was shown earlier in Figure 3.13(c) that solute-free cyclohexane produces dendrites during solidification. Moreover, mixed suspension/solution samples were made with both alumina particles and dissolved preceramic polymer. Here, the preceramic polymer was first dissolved in the solvent, followed by addition of the dispersant and alumina. After ball milling, the cross-linking agent was added prior to freeze casting. These samples produced pore structures more similar to the suspension system (Fig. 4.5), providing further evidence that suspended particles are disrupting the dendritic solidification microstructure.

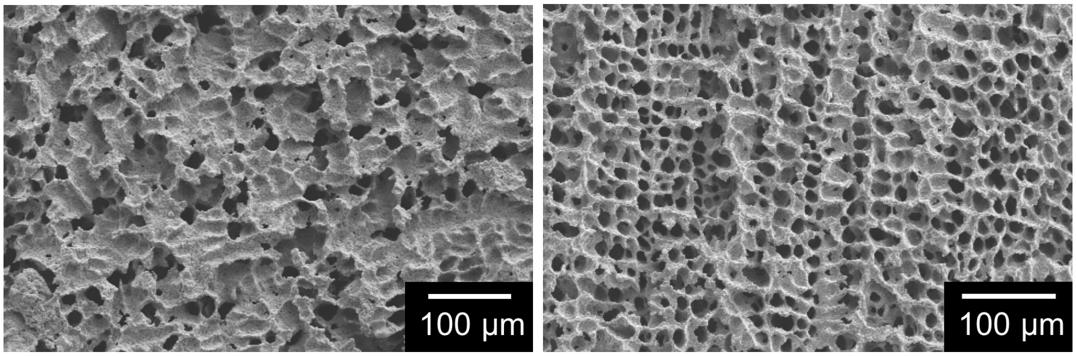

(a) Transverse (b) Longitudinal

Figure 4.5. Pore structure for a mixed suspension/solution sample consisting of both alumina powder and preceramic polymer, with cyclohexane as a solvent in (a) transverse view and (b) longitudinal views.

Brener et al. showed that a sufficient amount of *noise* ahead of a solid-liquid interface can affect the solidification microstructure by disrupting the growth of dendrite tips, destroying the regular patterns and instead creating fractal patterns.[112] This noise generally takes the form of fluctuations in the thermal or solute field ahead of the freezing front. Similarly, the presence of suspended particles located around the dendrite tips can act as a significant source of noise by inducing small temperature perturbations, as well as direct physical contact. In the present case, the noise generated by the alumina particles (∼350 nm) is approximately 1% the size of the each dendrite tip (∼40 µm). At this scale, we hypothesize that the dendrite tips are destabilized and break down, decreasing the anisotropy of the pore structure for cyclohexane and dioxane suspension-based samples.

In contrast, cyclooctane's foam-like structure and dimethyl carbonate's lamellar structure are interestingly retained regardless of processing routes. First, recall from Section 3.3.4 that cyclooctane has the lowest entropic factor of all the solvents studies, associated with a correspondingly low anisotropy. The optical micrograph of cyclooctane's solidification microstructure from Figure 3.15(b) as well as the pore structure seen in Figures 4.3(a) and 4.3(b) show that regardless of noise, stable dendritic growth is not achieved for cyclohexane in solutions. Hence, it would also be expected that cyclooctane suspension-based samples would similarly yield a non-dendritic structure. As for dimethyl carbonate, as the stability of a growing interface is proportional to the interfacial anisotropy, the faceted lamellar structure is not affected by noise generated from the suspended particles. The structures are therefore unchanged for both systems.

Results from various prior studies provide further evidence to support these claims. Camphene, a non-faceted solvent, has been shown to create different structures in suspension and solution-based systems, based upon independent studies. Suspension-based camphene produced a relatively isotropic structure,[13,34] however their solution-based counterparts created dendritic pore structures.[17,97] Moreover, tert-butanol, a faceted solvent known to generate prismatic crystals, shows negligible difference between suspension- and solution-based samples, supporting the argument for dimethyl carbonate's faceted lamellar structure being generated from both processing routes.[17,35]

4.3.2. Pore Size Comparisons from Suspension- and Solution-based Freeze Casting

The median pore diameter for each sample was calculated from MIP and is listed in Table 4.1. For both systems, pore diameters varied across the solvents used despite the same freezing front velocity of 15 µm/s being applied to all samples. This is understandable, as values for pore diameter obtained from MIP are calculated based on the throat size in which mercury is infiltrated when a certain pressure is applied. Since the throat of a spherical pore is inherently different from the lamellar spacing, differences in pore size are expected across solvents. This makes comparison of pore size across different types of structure a challenge. Pore size comparisons are best made when discussing analogous structures.

Hence, comparing equivalent solvents between the two systems, results show that suspension-based samples yielded larger pore sizes than solution-based samples for all solvents used, ranging from 50% to more than twice as large. This change can be attributed

Table 4.1. Median pore diameters obtained from mercury intrusion porosimetry for suspension- and solution-based samples.

	Suspension-based pore diameter (µm)	Solution-based pore diameter (µm)
Cycloocante	13.9	5.7
Cyclohexane	17.1	11.3
Dioxane	33.3	15.0
Dimethyl carbonate	36.3	24.6

to two factors: differences in the amount of undercooling during solidification and shrinkage during heat treatment. Solidification studies have shown that undercooling is a driving force for smaller microstructural features.[114] The presence of dissolved solutes (polymer) contributes to a larger degree of constitutional undercooling for solution-based samples, and consequently smaller pore sizes are expected. Additionally, the preceramic polymer experiences more shrinkage through pyrolysis than alumina does through sintering, measured to be roughly 26 and 13% in linear shrinkage, respectively. These differences could result in the median pore size of solution-based samples being comparatively smaller than those of suspension-based samples.

Pore size distributions for each solvent as determined by MIP, compared between suspension- and solution-based samples, are also shown in Figure 4.6. For most solvents, the distribution profiles were quite comparable: unimodal pore size distributions with broader distributions in the case of suspension-based systems. One exception is cyclohexane (Fig. 4.6(b)), where the cyclohexane suspension results in a unimodal pore distribution while its solution counterpart shows a bimodal pore size distribution. This bimodal distribution can be attributed to the two types of pores generated by the primary

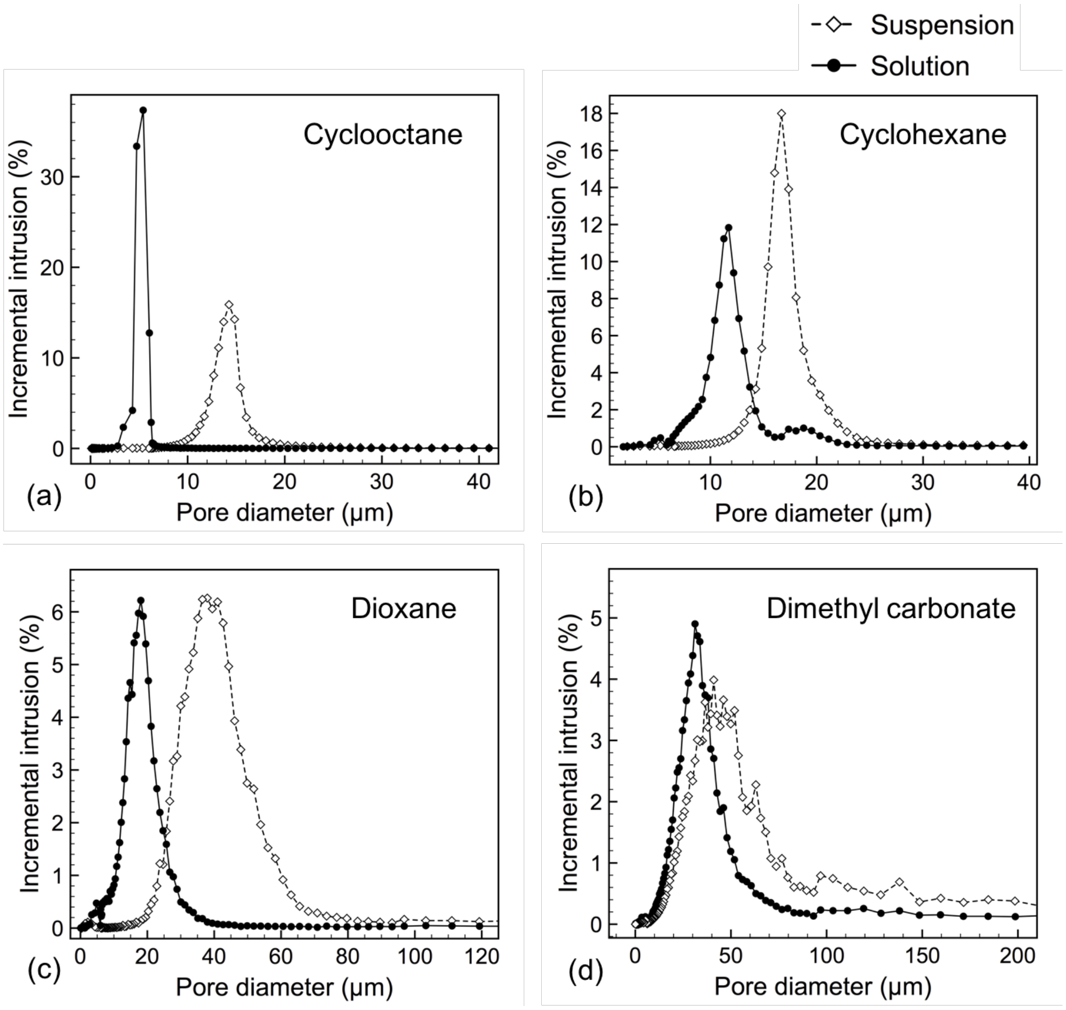

Figure 4.6. Pore size distribution plots of suspension- and solution-based samples made from (a) cyclooctane, (b) cyclohexane, (c) dioxane, and (d) dimethyl carbonate.

dendrite and secondary dendrite arms, where the average size of the primary dendrite is greater that the secondary arm. Not surprisingly, as the dendritic features are destabilized by noise in the suspension-based sample, features from the secondary dendrites disappear and a unimodal pore size distribution is instead seen. In contrast, even though dioxane solutions also generated primary and secondary dendrite arms, as seen in Figures 4.3(e), 4.3(f), a bimodal pore size distribution is not detected by MIP. On closer examination, the two types of dioxane dendritic features are not significantly different in size and therefore is not distinguishable via MIP.

4.3.3. Technological Implications of Suspension vs. Solution Freeze Casting

Aside from the changes in pore structure, freeze casting of preceramic polymer solutions offer several processing advantages over traditional suspension freeze casting. With suspension-based samples, extensive care must be taken during colloidal processing to ensure that a stable suspension is obtained prior to solidification. This requires a dispersant or surfactant that is compatible with not only the desired solvent, but also the surface chemistry of the particles. Additionally, a ball milling step is also required to break up agglomerates and prevent particles from settling. This not only increases the processing time required, but could also the reduces consistency of the samples produced. Alternatively, solution-based samples required comparatively little attention. Although a compatible solvent must be chosen such that the polymer can be dissolved, the dissolution process is completed over several minutes rather than hours.

The ability to observe the freezing front is also critical to the freeze casting technique as it provides valuable information regarding the pore formation process. While suspension-based processing consists of dispersed particles which scatter light and cause the suspension to be opaque, solution-based samples are transparent and enable measurement of the freezing front velocity. The advantages this capability provides has been shown in Section 3.3.5, as more structurally homogenous samples can be produced and greater control of the pore size can be achieved. Moreover, one can observe the shape of the freezing front and determine whether a particular solvent solidifies isothermally or requires undercooling. These benefits would otherwise not be possible with suspension-based freeze casting.

4.4. Conclusions

This study provided a direct comparison between suspension- and solution-based freeze casting as processing techniques for porous ceramics. Alumina powder and polymethylsiloxane preceramic polymer were each suspended or dissolved, respectively, in four different organic solvents and freeze cast to achieve various structures with 70% porosity. Differences in pore structures were largely seen in cyclohexane and dioxane samples, where distinct dendritic features were generated in solution-based samples but not in suspension-based samples. The presence of small suspended particles ahead of a solid-liquid interface are hypothesized to generate a sufficient amount of noise to destabilize the dendrite tip in suspension-based samples. Mercury intrusion porosimetry showed that solution-based samples generated smaller pore sizes, likely due differences in the amount of undercooling during solidification as well as shrinkage during densification. Various processing advantages gained with solution processing were also highlighted. Solution-based processing was shown to be the simpler processing technique, requiring shorter processing times. Additionally, transparent solutions allowed for direct observation during solidification, providing beneficial information for freeze casting.

CHAPTER 5

Mechanical and Permeability Properties of Freeze Cast SiOC

5.1. Introduction

Two attributes commonly sought after in porous materials are high mechanical strength and low pressure drop during transport. Although low pressure drops can be achieved by increasing the porosity, this often comes at a cost of compromising the mechanical integrity. Directionally-aligned pore structures generated from freeze casting have therefore attracted interest for optimizing these properties along the freezing direction.[115] However, studies of these properties on freeze cast structures have been limited to aqueous-based lamellar structures.[18,25,116–120] While Chapter 3 showed that freeze casting is able to produce ceramics with highly varied pore morphologies, differences in performance between various pore morphologies has not been explored.

In this chapter, the compressive strengths and permeability constants of porous SiOC with dendritic and lamellar pore morphologies are compared. Cyclohexane and dimethyl carbonate are used as solvents to generate dendritic and lamellar structures, respectively. The compressive strengths are assessed by uniaxially loading each sample to failure, while the permeability constants are calculated by measuring the flow rate of water at various pressure drops. For both tests, measurements were performed parallel to the solidification direction, and varying polymer concentrations are used to achieve a range of open porosities. The influence of changes in the freezing front velocity on both properties are also studied.

5.2. Experimental Methods

5.2.1. Sample Preparation

The freeze casting setup and procedure used in this study were as described in Section 3.2.2. Cyclohexane and dimethyl carbonate samples with 10, 20, 30, and 40 wt.% polymer concentrations were freeze cast to a height of 25 mm at a freezing front velocity of 15 µm/s. Polymer solutions were degassed prior to freezing to remove any air bubbles that may generate unwanted pores. Additional cyclohexane samples were also frozen at 5 µm/s in order to determine the influence of freezing front velocity. However, 40 wt.% samples were excluded from the low freezing front velocity since a constant velocity profile could not be maintained due to initial undercooling at the base of the sample. After each sample was freeze cast and pyrolyzed to obtain a porous SiOC ceramic, their porosities were determined by Archimedes' method prior to being machined and prepared accordingly for each testing method.

5.2.2. Porosity and Density

The porosity of each sample was measured using Archimedes' method, as mentioned in Section 3.2.2. A value of 2.32 g/cm^3 was used as the true density of SiOC, according to Table 3.2, and the bulk density was scaled linearly with the porosity, according to the relationship shown in Figure 3.4.

5.2.3. Compressive Strength Measurements

To prepare samples for compressive strength measurements, pyrolyzed samples were first machined with a diamond core drill ($\varnothing$ = 15.9 mm) in order to remove the edges of the sample and obtain a uniform cylindrical sample. Following cleaning via sonication, a high strength and low shrinkage mineral-filled acrylic system (VariDur 3003, Buehler, Lake Bluff, IL, USA) was used to cap the ends of the sample that would be in contact with the compression plates. These caps were applied to each sample since brittle porous materials are known to display crushing behavior from contact stresses in compression tests, leading to erroneous and inconsistent results. A study by Mehr et al. showed that the incorporation of an interface layer such as the one used here can help provide more accurate and reliable results without artificially altering the structure's properties.[121]

Compression tests were performed on an Instron 4204 universal testing machine (Instron, Norwood, MA, USA) in constant displacement mode. The crosshead was lowered at a rate of 0.1 mm/min and data were recorded at an interval of 0.5 seconds. A pair of spherical washers were placed between the sample and the compression platens to account for non-parallel sample surfaces and ensure that the compression load was applied along the axis of the sample. The height and diameter of each sample were also recorded prior to testing. Values for compressive strength were determined based on the highest load sustained prior to a significant drop (>20% of the maximum load) and by a measurable change in stiffness. These criteria were applied since small load drops not associated with failure can sometimes be observed, and fractured samples can continue to bear larger loads via compaction, albeit with a associated drop in the measured stiffness.

5.2.4. Permeability Measurements

For permeability measurements, samples were similarly machined with a 15.9 mm diameter core drill and cleaned via sonication. In order to ensure that there are no leaks from the sides of the porous samples which would inflate the permeability results, each sample was circumferentially enclosed with the same solid acrylic. To do so, samples were placed inside a Tygon® tube (h = 25.4 mm, ID = 19.1 mm) which acted as a casting mold for the acrylic. The acrylic was prepared and stirred for roughly 7 minutes prior to pouring onto the sample, at which point the acrylic should harden within the following minute to ensure that the pores were not infiltrated. After 24 hours of curing, the ends of the sample were removed with a diamond saw to obtain a permeability sample with a thickness of approximately 9 mm.

Permeability measurements were performed by measuring the flow rate of water at various pressure drops using a setup illustrated in Figure 5.1. A voltage-controlled gear pump was used to transfer deionized water from a reservoir to a collection vessel sitting on an electronic scale via a high-pressure Tygon® tube with 19.1 mm inner diameter. An Omega PX409 pressure transducer (Omega Engineering, Stamford, CT, USA) was attached to a pipe fitting to measure and electronically record gauge pressure. Additionally, a valve was attached to the pipe fitting to remove air from the system before each measurement.

To begin each experiment, a sample prepared according to the procedure described above was inserted into the tube and gripped with a hose clamp which was tightened using a torque wrench; the wrench was set to a value (35 inch-pounds) that ensures no circumferential leakage, determined beforehand using a dense cylindrical acrylic puck.

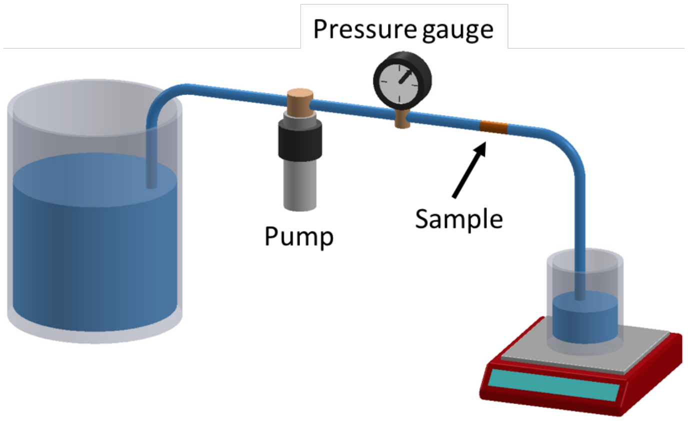

Figure 5.1. Schematic of the setup used to measure water permeability across a porous sample.

The pump was then turned on, set to a certain pressure, and held for 30 seconds while the mass change and flow rate were recorded. The pressure was incrementally increased and a minimum of six different pressures were recorded for each sample. For highly permeable samples (e.g. high porosity lamellar), pressures of roughly 10 to 100 kPa were applied, whereas low permeability samples (e.g. low porosity dendritic) experienced pressures ranging from roughly 20 to 350 kPa. All reported measurements were performed with the sample oriented such that water flowed from the top to the bottom of the sample; separate experiments were also conducted to show that results were indistinguishable from those where samples were oriented bottom to top.

With the dimensions of each sample and the flow rates associated with several pressure drops, the Darcian permeability constant can be calculated according to the Forchheimer equation:

$$\frac{\Delta \mathrm{P}}{\mathrm{L}} = \frac{\mu}{\mathrm{k}_1}\mathrm{v} + \frac{\rho}{\mathrm{k}_2}\mathrm{v}^2 \tag{5.1}$$

where ΔP is the pressure drop, L is the length of the sample, μ and ρ are the viscosity and density of the flowing fluid, respectively, v is the flow velocity, and k_1 and k_2 are the respective Darcian and non-Darcian permeability constants. The non-Darcian permeability constant describes a non-linear flow behavior associated with inertial effects which arises at high flow velocities and is usually only observed with gas flow. Since water was used as the fluid in this case, a linear flow behavior was observed, and the k_2 term can therefore be neglected. A value of 8.90 x 10^{-4} Pa-s was used for the viscosity of water at 25 °C.

5.3. Results and Discussion

5.3.1. Compression Tests

Fracture Behavior

The fracture behavior of dendritic and lamellar samples subjected to compression tests were observed to be significantly different from one another, as shown in Figure 5.2. The low magnification optical images show that dendritic samples seemed to fracture by bending of the pore walls, with cracks occurring throughout the cross-section of the sample, while lamellar samples usually show a distinctive shear crack at roughly 45 degrees, with an optically reflective fracture surface. A higher magnification SEM image (Fig. 5.2(c)) shows a representative view of the multiple deep fissures present in the dendritic sample. In contrast, the lamellar fracture surface is comprised of just a few wide lamellae plates, with their flat side facing the fracture surface (Fig. 5.2(d)). In particularly, the fracture surface of lamellar samples indicate that failure was probably not caused by crack growth through the entire sample, but rather just sliding of loosely interconnected lamellae.

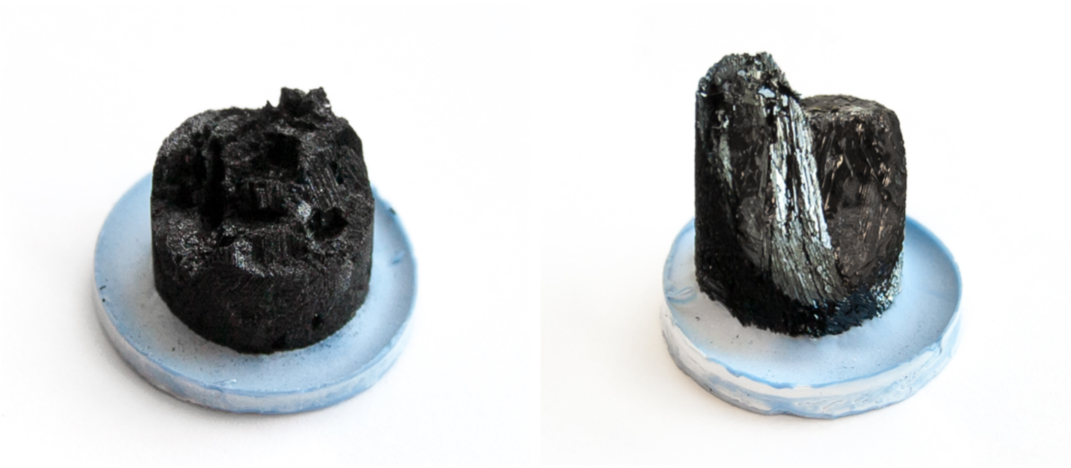

(a) Dendritic (Optical) (b) Lamellar (Optical)

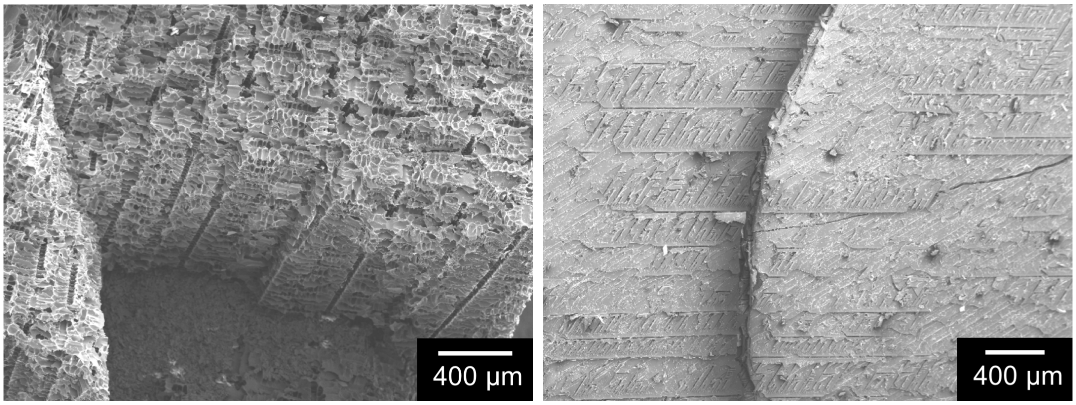

(c) Dendritic (SEM) (d) Lamellar (SEM)

Figure 5.2. Representative optical and SEM images of the fracture surfaces from (a,c) dendritic and (b,d) lamellar samples failing via compression.

Figure 5.3 shows the load-displacement plots of several representative dendritic and lamellar samples, with the maximum load used to calculate the compressive strength of each sample marked with a star. A range of fracture behaviors are observed here, ranging from typical behavior expected from porous materials to behavior characteristic of a dense, brittle ceramic. It should also be noted that the non-linearity seen at the beginning of each test can be attributed to the acrylic end caps and alignment of spherical washers used, described earlier in Section 5.2. Nevertheless, these influences are not expected to affect the failure load and the compressive strength, and should be subtracted to assess the material response.

First, Figure 5.3(a) shows constant loading until 400 N, at which point a load drop and crack propagation occur. This is followed by crushing of the sample to higher loads which is identified by a decrease in the measured stiffness. In Figure 5.3(b), several small load drops are observed prior to failure; these can be attributed to nucleation of local micro-cracks which have yet to propagate through the sample to cause failure. Eventually, the density of micro-cracks is high enough that failure is observed. Figure 5.3(c) demonstrates a dendritic sample with relatively low porosity showing ideal behavior expected from dense brittle fracture. In contrast, the response seen in Figure 5.3(d) is representative of progressive failure associated with the loosely interconnected lamellar walls produced from dimethyl carbonate. Presumably, the structure is unable to sustain higher loads as the lamellae walls begin to collapse, and a large load drop is observed when the walls become fully disconnected. Similarly, Figure 5.3(e) shows the lamellar sample failing by slipping of the lamellae plates; however it continues to experience crushing following failure. Unlike Figure 5.2(a), the failure surface of this particular sample is flat, and is therefore able to sustain higher loads as it crushes. Lastly, Figure 5.3(f) shows that small load drops attributed to local crack nucleation can also be observed in lamellar samples, also visible in Figure 5.2(d). Interestingly, this particular sample does not show a fracture surface representative of lamellae walls slipping, but rather seems to fail by wall bending, presumably due to the lamellae sheets aligning more parallel to the loading axis.

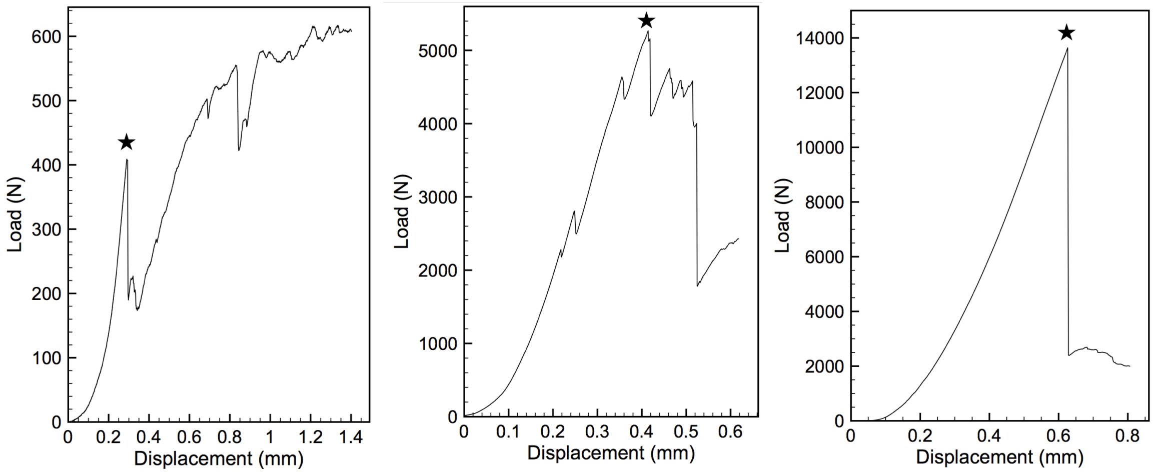

(a) Dendritic (87%) (b) Dendritic (64%) (c) Dendritic (46%)

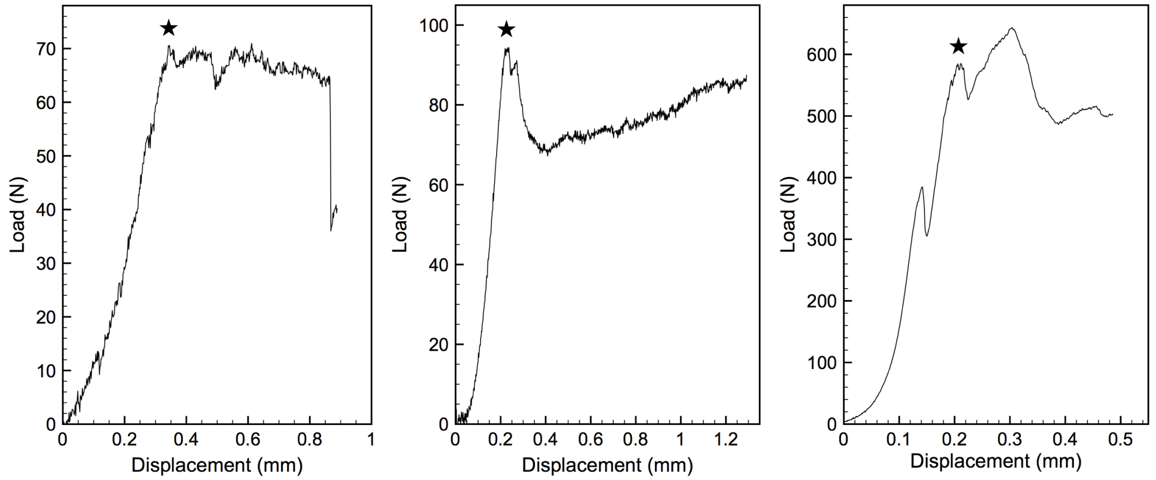

(d) Lamellar (85%) (e) Lamellar (77%) (f) Lamellar (75%)

Figure 5.3. Load-displacement plots for samples with dendritic and lamellar pore morphologies. The morphology and porosity of each sample is noted below each plot, and a star denotes the load used to calculate the compressive strength.

Many of the responses discussed here are observed in a variety of sample types, regardless of pore morphology and porosity. For example, small load drops not associated with failure are seen in both dendritic and lamellar samples, at high and low porosities. However, certain behaviors are encountered more frequently based on the sample's pore morphology and porosity. Generally, a large load drop reminiscent of dense brittle materials (Fig. 5.3(c)) is observed with dendritic samples rather than lamellar samples. Although higher porosity samples can also exhibit behavior reminiscent of dense ceramics, it is more commonly seen in low porosity samples. Additionally, lamellar samples often display more gradual and progressive failure prior to a large load drop (Fig. 5.3(d)), as expected due to the collapse of lamellar walls. Conversely, this behavior is rarely seen in dendritic samples, with typical crack growth behavior being more prevalent due to the structure's well-connected pore walls.

Compressive Strength

Figure 5.4 shows the compressive strength of SiOC samples with dendritic and lamellar pore morphologies, made using cyclohexane and dimethyl carbonate as solvents, respectively. The effect of changes in the freezing front velocity, from 5 to 15 µm/s, is also demonstrated with dendritic samples. Results show that structures with a dendritic pore morphology are significantly stronger than those with a lamellar morphology. However, highly porous samples (∼90%) show similarly low compressive strength values (∼2 MPa) for both pore morphologies. Furthermore, while a decrease in the freezing front velocity created larger pore sizes for dendritic samples, samples made with freezing front velocities of 5 µm/s did not show any noticeable affect on the compressive strength, as the results fall in line with samples made with 15 µm/s. In contrast, several studies on aqueous-based lamellar structures have correlated larger pore sizes to lower compressive strengths, explained by failure of the lamellae walls due to buckling.[39,122] In the case of these dendritic structures, it is possible that the change in median pore size from 16.7 to 26.8 µm is not significant enough to result in a difference, or that the highly-connected dendritic pore walls result in failure of the structure via compressive crushing, where the strength is dependent only on the pore fraction and not the pore size.

More specifically, dendritic samples show impressive strengths of up to 100 MPa for samples with roughly 50% porosity and a bulk density of 1.2 g/cm^3. Both freezing front velocities also produced results with a relatively low amount of dispersion when compared to fracture behavior normally expected from brittle porous materials. On the other hand, lamellar samples have a high degree of dispersion, as shown with a rescaled plot in Figure 5.5. The compressive strengths here range from as low as 0.5 to 3.1 MPa. While the trend is inconclusive for lamellar samples, there is a slightly observable increase in the strength as the porosity decreases.

This striking difference in compressive strengths between the two pore morphologies can be attributed to the lack of connectivity between lamellar walls. Whereas the pore walls in a dendritic structure are highly connected throughout the whole sample (Fig. 3.7), the lamellae produced from dimethyl carbonate form as loosely stacked platelets (Fig. 3.9). In this configuration, the slip or failure of a few lamellae can easily propagate at lower loads. Additionally, an increase in the polymer concentration (decrease in porosity) does not necessarily correlate to a stronger structure since the structural flaws remain, as the lamellae remain poorly interconnected. Yet, this result does not mean that all porous

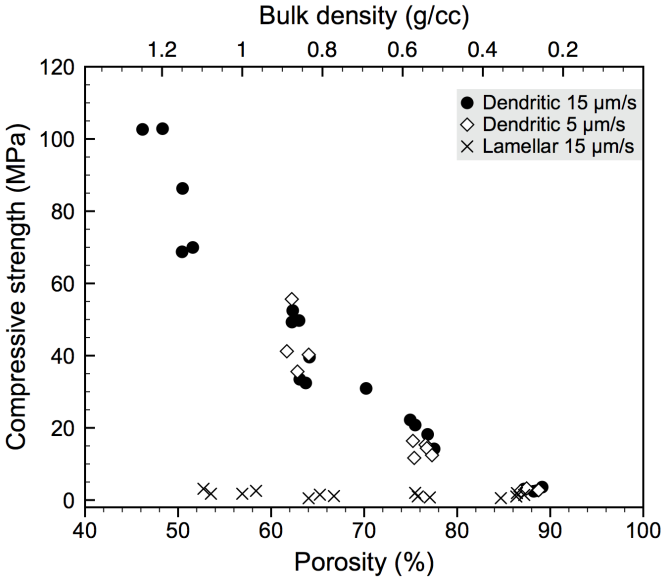

Figure 5.4. Compressive strength results of samples with dendritic and lamellar pore morphologies, produced with cyclohexane and dimethyl carbonate, respectively. Dendritic samples were produced with 5 and 15 µm/s.

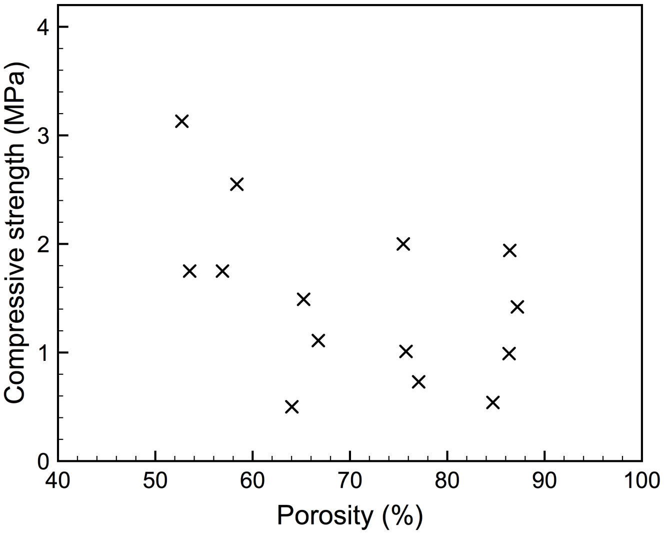

Figure 5.5. A rescaled plot of the compressive strength results for lamellar samples.

lamellar structures are inherently weak, as aqueous-based lamellar structures which are more interconnected have shown higher compressive strengths.[18,115,116]

The compressive strength values obtained from this study can be compared to other porous structures from literature. Figure 5.6 shows the compressive strength of various porous ceramics processed via freeze casting as well as foaming, plotted against porosity and bulk density.[18,43,116,123,124] However, this literature comparison should not be seen as entirely representative of structural differences; independent studies will likely have differences in processing that may explain differences in the results.

Compared at equivalent porosities, the compressive strength of this study's dendritic SiOC lies around the average, where it is significantly stronger than foamed hydroxyapatite[124] and freeze cast lamellar alumina,[43] comparable to freeze cast lamellar hydroxyapatite,[116] but noticeably weaker than freeze cast dendritic alumina[123] and lamellar YSZ.[18]

However, the data shown here include structures made from hydroxyapatite, alumina, and yttria-stabilized zirconia, all which are considerably denser than SiOC (Table 5.1). Consequently, the compressive strength is also plotted against bulk density where the results can be normalized by weight. Doing so, this study's dendritic SiOC show superior performance for situations where weight is a consideration. While the lamellar YSZ can still yield very high compressive strengths of up to 200 MPa, the dendritic SiOC produced here can provide equivalent compressive strength values with roughly half the weight.

On the other hand, the lamellar SiOC made from dimethyl carbonate in this study is weaker than most structures, with the exception of foamed hydroxyapatite. Results do however fall in line with other freeze cast lamellar structures (filled makers) if extrapolated to low bulk densities. Nevertheless, a large variation in the strength of lamellar structures

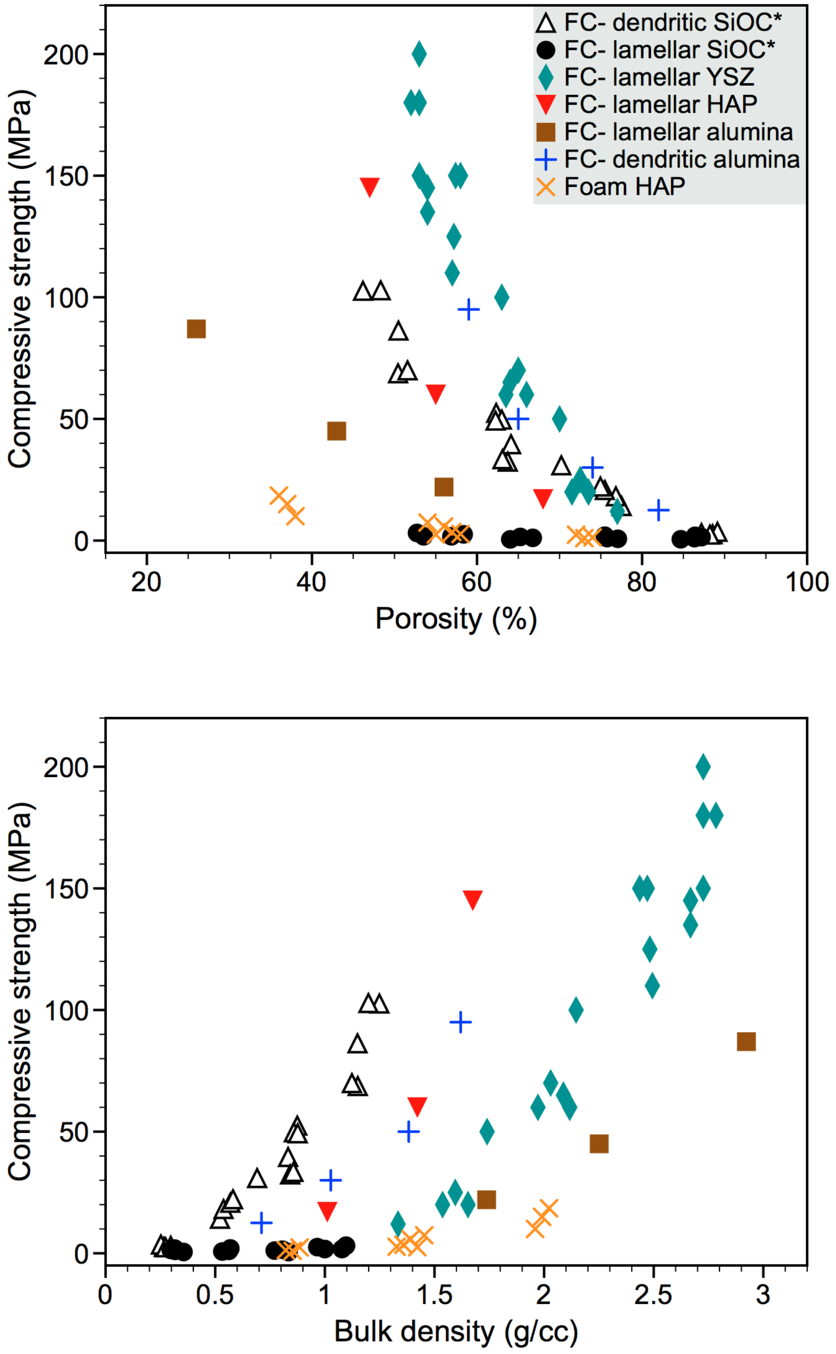

Figure 5.6. Compressive strength results compared to literature values plotted against porosity and bulk density.[18,43,116,123,124] FC denotes that the sample was made by directional freeze casting and loaded parallel to the freezing direction, whereas an asterisk marks the results from this study.

Table 5.1. Density of several materials used in literature for compression tests. The bulk density was calculated based on these densities and the associated porosity.

Material	Density (g/cm^3)
Silicon oxycarbide (SiOC)	2.32
Hydroxyapatite (HAP)	3.16
Alumina (Al_2O_3)	3.95
Yttria-stabilized zirconia (YSZ)	5.80

is seen across multiple studies. Figure 5.7 shows how the structure varies significantly between the weaker and more loosely interconnected lamellar platelets produced in this study from dimethyl carbonate, shown in Figure 5.7(a) (black circle, Fig. 5.6) and the stronger and highly interconnected structure of YSZ in Figure 5.7(b) (teal diamond, Fig. 5.6). Whereas dimethyl carbonate produces plates which look to be stacked adjacently, water produces bridges which form connections between each lamella. This difference in structure could be explained with the Jackson-α factor discussed in Section 3.3.4, where dimethyl carbonate's faceted plates is associated to its high entropic factor. From these results, it is evident that minor differences in the structural details can have a considerable impact on the strength of freeze cast lamellar structures.

Comparison to Theoretical Models

Several models have been developed to describe the porosity dependence of various mechanical properties, including compressive strength. For example, Gibson and Ashby extensively discussed the mechanical response of various types of cellular materials, defined as porous materials where the relative density is less than 0.3; as the relative density increased above 0.3, pores often become isolated such that assumptions made regarding interconnected pore networks were no longer applicable.[125] In their study, porous structures were categorized as either honeycombs, open-cell foams, or closed-cell foams. The resulting relationship between relative density (or porosity) and compressive strength of the porous material, is given as:

$$\frac{\sigma_{\mathrm{o}}}{\sigma_{\mathrm{fs}}} = \mathrm{C}\left(\frac{\rho^*}{\rho}\right)^{\mathrm{n}} \tag{5.2}$$

where σ_o is the compressive strength of the porous material, σ_{fs} is the flexural strength of the cell wall material, C is a dimensionless constant, n is the fitting parameter, and ρ^* and ρ is the bulk and true density, respectively. For brittle failure in compression, n was determined to be 1, 3/2, and 2 for axially-loaded honeycombs, open-cell foams, and closed-cell foams, respectively. However, studies by Gulati and Schneider showed

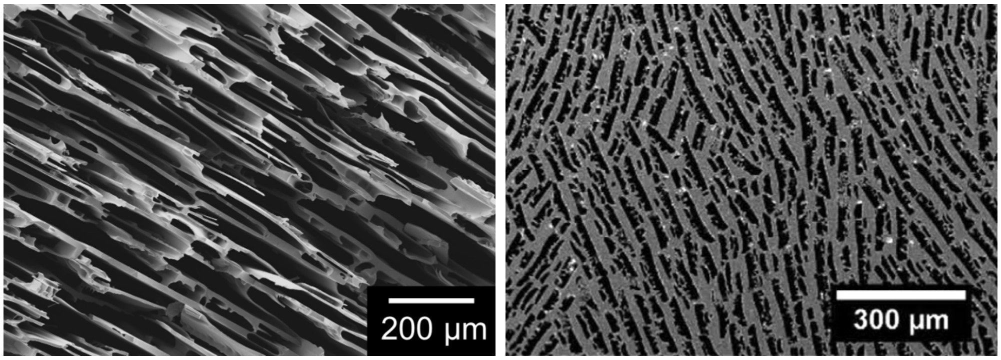

(a) (b)

Figure 5.7. SEM micrographs of variations in lamellar structure that could lead to changes in compressive strength: (a) loosely interconnected lamellar network from dimethyl carbonate (black circle, Fig. 5.6) and (b) highly interconnected lamellar yttria stabilized zirconia network from water (teal diamond,[18] Fig. 5.6).

contradictory results, with a dependence of n = 2 for extruded square-cell honeycombs loaded in the axial direction.[126,127]

Figure 5.8 shows the compressive strength of dendritic samples from this study compared against expected values from the model, using several n values, and where C = 0.65. A flexural strength of 385 MPa was used based on results from 3-point bending tests of siloxane-derived SiOC bars by Renlund et al.[128] Although a flexural strength of 153 MPa for SiOC fibers was also reported in the same study with smaller errors, and used to model the compressive strength of SiOC foams in a study by Colombo et al.,[129] the value was too small to produce an appropriate fit for this study.

Here, a good fit was observed with n = 2, particularly in the range of low (< 0.3) relative densities. The fit of n = 2 correlates to a structure representative of closed-cell foams, as described by Gibson and Ashby, or extruded honeycombs, per Gulati and Schneider. Given their cylindrical and directionally-aligned pores, the dendritic pore structure produced from freeze casting cyclohexane in this study better resembles a honeycomb structure than a closed-cell foam. At higher relative densities (> 0.3), the compressive strengths deviate slightly from n = 2, presumably due to the pores becoming more isolated, as alluded to earlier. Studies by Roy Rice treated porous structures low porosities according to their minimum solid area (MSA), which yields a 1 - P dependence (where P is the pore fraction), similar to Equation 5.2; in this case, n = 1 represents the upper bound of the dependence.[127] However, even at high relative densities, results from our study do not fit this model. Interestingly, the compressive strength of SiOC foams from Colombo et al. also showed good agreement with n = 2, although with significantly lower compressive strengths than this study's dendritic samples at equivalent porosities, roughly

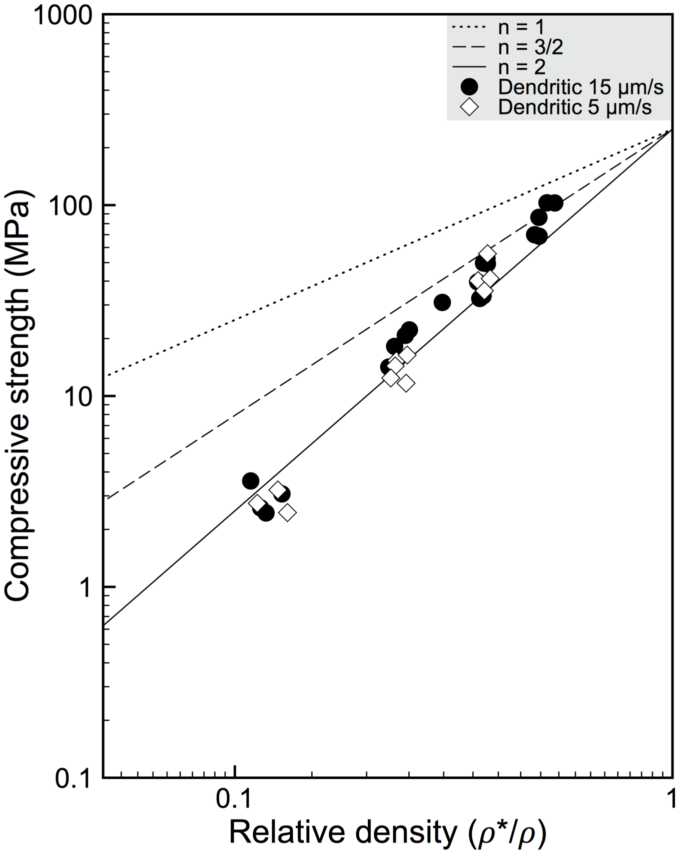

Figure 5.8. Compressive strength of dendritic samples compared to expected values from theoretical models.

10 versus 20 MPa at 75% porosity, respectively.[129] In conjunction, these results show that the difference in pore morphology between a directionally-aligned dendritic structure and an isotropic foam yields notable differences in the compressive strength, but does not seem to have an effect on the porosity dependence.

5.3.2. Permeability Tests

Figure 5.9 shows data obtained from permeability measurements of pressure drop across a sample length L plotted against various water flow rates. Each line represents a single sample, with a decreasing slope corresponding to samples with higher porosities and consequently to those yielding lower pressure drops. While some overlap in permeability between dendritic samples with high porosity and lamellar samples with low porosity can be observed, it is already clear from these data, shown for both types of samples in the same porosity range, that lamellar samples are more permeable to fluid flow. Additionally, the linear behavior of the samples shown here confirms that the non-Darcian permeability constant from Equation 5.1 can be neglected. Due to water being used as a fluid, the flow rate is not sufficiently high to display inertial behavior which would otherwise be present with gases.

Using the dimensions of each sample and pressure drop data from Figure 5.9, the permeability constant k_1 is calculated according to Equation 5.1 and shown in Figure 5.10. The effect of pore morphology (dendritic and lamellar) and freezing front velocity on the permeability constant are compared. Results show that lamellar samples yield higher permeability constants than dendritic samples across all porosities. Comparing samples produced with the same freezing front velocity of 15 µm/s, dendritic samples with $\sim$77% porosity have equivalent permeability constants to lamellar samples with $\sim$55% porosity. A decrease in the freezing front velocity to 5 µm/s for dendritic samples expectedly yields samples in noticeably higher k_1 values compared to their 15 µm/s counterpart. This difference is due to the larger dendrites formed during slower solidification, as shown earlier in Figure 3.19, where the size of the primary and secondary dendrites increased by approximately 15 and 10 µm, respectively, an increase of roughly 60% in both cases. An equivalent 5 µm/s dendritic sample with $\sim$77% porosity now corresponds to similar k_1 values with $\sim$65% porosity lamellar samples.

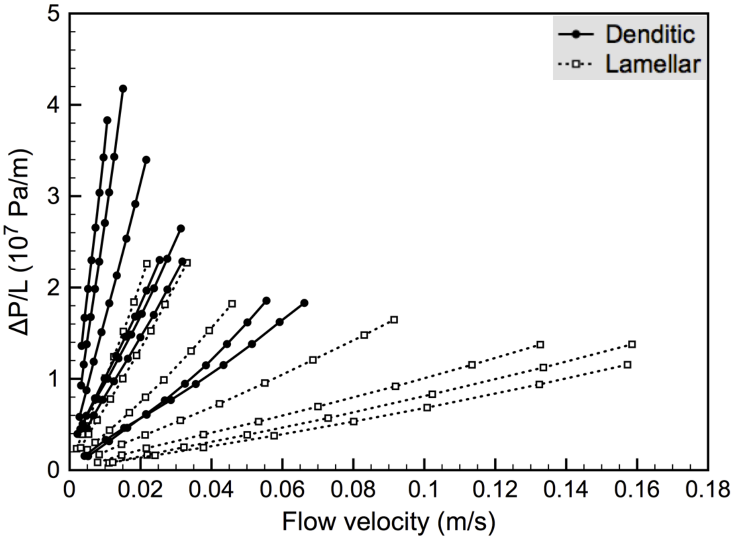

Figure 5.9. Data obtained from permeability measurements: water flow rate at various pressure drops for dendritic and lamellar samples.

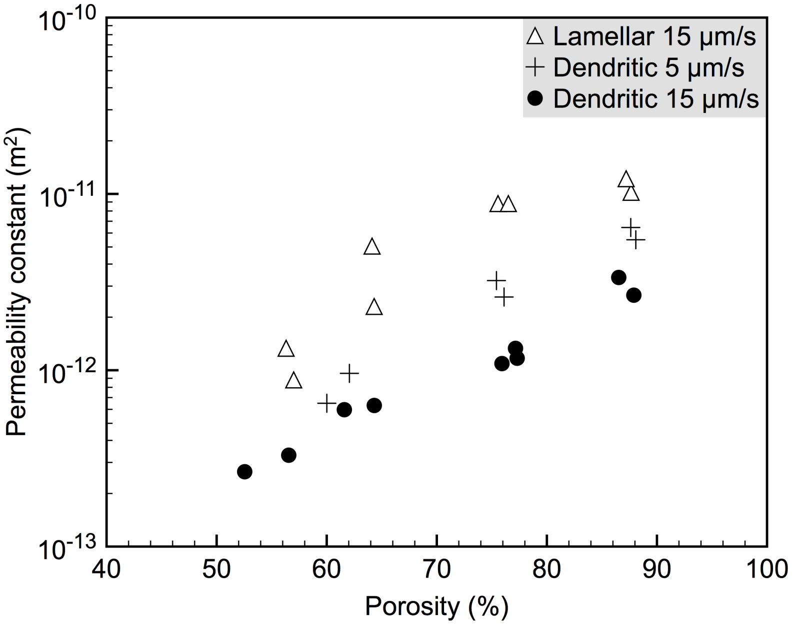

Figure 5.10. Darcian permeability constants for dendritic and lamellar samples.

The lower permeability constants observed with dendritic structures produced from cyclohexane can be attributed to their branched pore structure, and possibly differences in the pore size. While the lamellar structure is comprised of two-dimensional pores which travel from top to bottom with few lateral features that could have an adverse affect on the fluid flow, cyclohexane's dendritic structure contains features from the secondary dendrite arms that are not aligned along the flow direction. With regard to flow rate, this structural inefficiency effectively increases the tortuosity of dendritic samples and results in higher pressure drops compared to lamellar samples. Additionally, while the original intent for using the same freezing front velocity for both solvents was to have the pore morphology be the main process variable, mercury porosimetry results from Table 4.1 showed that dimethyl carbonate produced a median pore size of 24.6 µm, versus 11.3 µm for cyclohexane. Naturally, this would seem to contribute to a higher permeability for lamellar samples. However, several factors make the median pore size an unreliable indicator of permeability. As discussed in Chapter 4, comparing pore sizes across various types of pore morphologies can be problematic due to differences in the pore geometries. The elongated lamellar pores are not well-represented by the spherical pore assumption of the Washburn equation, and the calculated pore size seems to represent the lamellar spacing without taking into account their length. Moreover, cyclohexane's median pore diameter is heavily weighted towards the smaller secondary dendrites while the primary dendritic pores should be providing most of the flow capabilities. These issues introduce ambiguity in trying to compare the permeability of different pore morphologies using identical freezing front velocities. Nevertheless, the solidification conditions had to be kept comparable, and freezing front velocity was determined to be the more suitable processing parameter when compared to a constant cold plate temperature or ramp rate, as various solvents can have significantly different melting temperatures.

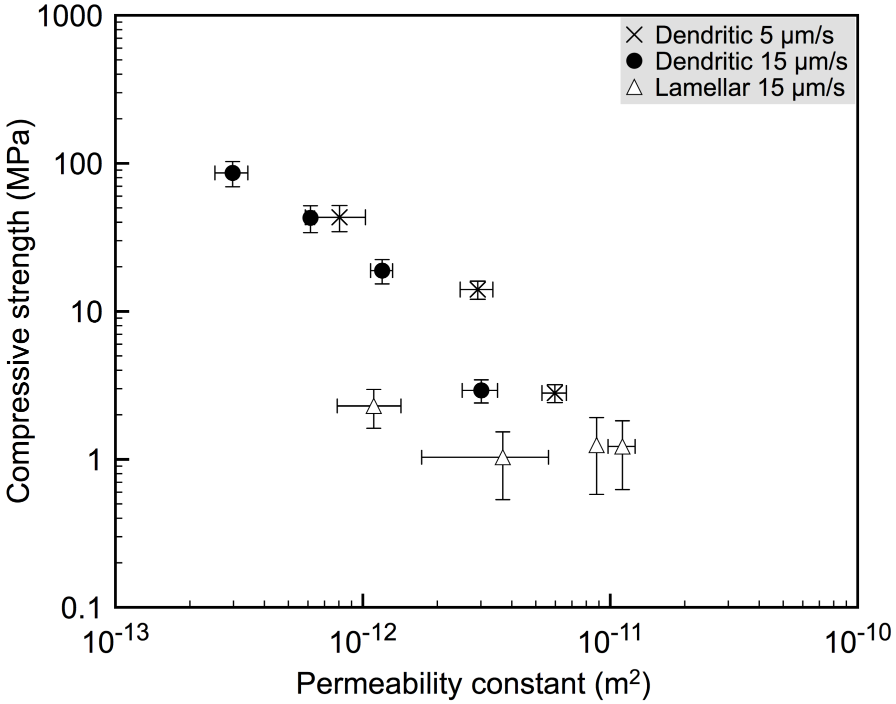

Figure 5.11. Compressive strength and permeability constants of dendritic and lamellar samples group according to the polymer concentration used (similar pore fractions).

Finally, Figure 5.11 shows the combined result of the compressive strengths and permeability constants of samples with dendritic and lamellar structures. Each data point represents a group of samples made from either 10, 20, 30, or 40 wt.% polymer concentration, producing similar porosity values with a standard deviation of roughly 1 to 2 % porosity. Here, the negative correlation is clearly seen between the two properties. While high compressive strength and permeability constants are often preferred for most applications, this can be difficult to achieve. Nevertheless, the result suggests that both properties could possibly be maximized by either (i) producing a structure with well-interconnected pore walls such as the dendritic structure, and creating the largest pore size suitable for the particular application, or (ii) improving the pore wall connectivity of the flow-conducive lamellar structures to enhance their compressive strengths.

5.4. Conclusions

Compressive strength and water permeability tests were performed on freeze cast samples with dendritic and lamellar pore morphologies, made from cyclohexane and dimethyl carbonate, respectively. Results showed that dendritic samples possessed significantly higher compressive strengths than lamellar samples, and a decrease in freezing front velocity for dendritic samples did not produce any evident change in compressive strength. The strengths ranged from roughly 1 to 100 MPa for dendritic samples and 1 to 3 MPa for lamellar samples, with 90 to 50% porosity, respectively. Compared to literature values, dendritic samples showed comparable strength to other freeze cast structures when judged against equivalent pore fractions. However, when compared using bulk density, this study's SiOC samples showed superior performance. On the other hand, the poor strength of this study's lamellar samples was attributed to subtle microstructural differences, as dimethyl carbonate produced lamellae which were poorly interconnected when compared with those of aqueous-based samples. Conversely, permeability tests showed that lamellar samples had higher Darcian permeability constants than dendritic samples. While a lower freezing front velocity for dendritic samples did not have an affect on compressive strength, a considerable increase in the permeability constant is seen in this case, although not enough to surpass lamellar samples. The disparity in permeability constants between the two types of pore morphologies was attributed to structural inefficiency associated with dendritic samples, as well as differences in pore sizes.

CHAPTER 6

Nucleation-controlled Freeze Casting for Improved Pore Alignment

Material in this chapter is reproduced in part from ”Nucleation-controlled freeze casting of preceramic polymers for uniaxial pores in Si-based ceramics”, M. Naviroj et al.; *Scripta Materialia*, 130 (2017): 32-36.

6.1. Introduction

A main advantage that freeze casting provides as a processing technique is its innate tendency to create directionally-aligned pores based on the thermal gradient applied during solidification. This aspect of the technique is highly desirable since applications such as catalyst supports, filtration membranes, and electrodes require optimized flow and mechanical properties along a particular direction. However, the majority of freeze casting is performed by simply pouring the precursor into a mold resting on the cold surface, resulting in random nucleation of crystals at the base of the sample.[130] Although freeze cast structures generated in this manner have indeed shown directionality, crystals growing at oblique angles create defects such as misaligned pores. For example in water-based systems with lamellar pores, numerous pore domains are present since nucleation of certain ice crystals produces grains which grow off-axis from the thermal gradient.[23] These defects can reduce the homogeneity and directionality of the pore structure, effectively compromising its performance.[39,115,131]

While many studies on freeze casting have explored the effects of various processing conditions such as solvent choice, particle size, and freezing front velocity on the pore structure, only a few studies have considered to control the process of nucleation and grain formation of solvent crystals. Recently, Bai et al. has shown that lamellar structures can be aligned by creating dual temperature gradients during solidification.[132] Munch et al. has also demonstrated the use of various patterned surfaces to manipulate the growth of ice crystals.[44] Although these methods have shown improvements in pore alignment, this study takes a different approach to the nucleation problem.

Here, a classic grain selection process is applied to freeze casting to achieve increased alignment of dendritic pores. Grain selection is a technique frequently used in metals processing where single crystal components are required. For example, Ni-superalloy turbine blades which require creep resistance at high temperatures are often produced using a spiral grain selector, also known as a pigtail.[133,134] In this work, instead of pouring the precursor directly onto a cold surface, a 3D printed template was placed between the casting mold and the cold surface to serve as a grain selector. This template decreases the number of off-axis solvent crystals and effectively increases the alignment of pores. Image analysis and permeability measurements were employed to quantify the effectiveness of each template.

6.2. Experimental Methods

6.2.1. Sample Preparation

The freeze casting setup and procedure used in this study were as described in Section 3.2.2. Polymer solutions were prepared by dissolving MK powder in cyclohexane using a magnetic stir bar. The cross-linking agent Geniosil GF 91 was then added at a concentration of 1 wt.% of the solution. Polymer solutions were degassed in a vacuum chamber prior to freezing to remove air bubbles that may generate unwanted pores during freezing. All samples freeze cast in this study were prepared with 20 wt.% of polysiloxane in cyclohexane and a freezing front velocity of 5 µm/s, resulting in porosities of roughly 75 vol.% after pyrolysis. Samples were pyrolyzed in Ar at 1100 °C for 4 hours, using a ramp rate of 2 °C/min.

6.2.2. Grain-selection Templates

To improve the pore alignment, grain selection templates were printed using stereolithography (Autodesk Ember, San Rafael, CA, USA). Figure 6.1 shows an example of a CAD drawing used to print a template. Each of the templates contained a hollow column located in the center acting as the grain selector. A total of three different templates with varying heights, hole diameters, and aspect ratios were used in this study, and their dimensions are listed in Table 6.1. Template 1 is the shortest at 5 mm, Template 2 has an increased height of 10 mm, but with the same hole diameter as Template 1, and Template 3 has the height of Template 2 but with a reduced diameter of 0.5 mm. The templates were designed as open sandwich structures so that air could be used to create sufficient thermal insulation between the top and bottom surfaces, such that nucleation is prevented from occurring anywhere besides the bottom of the designated column. Consequently, this insulation also caused thermal conduction to be limited to just the 0.5 or 1.5 mm diameter column, severely limiting the cooling capacity, and hence a relatively low freezing front velocity of 5 µm/s was used. In addition to the templated samples, a control sample freeze cast directly on the cold surface was also analyzed for comparison.

Table 6.1. Dimension of the various grain-selection templates used.

	Template height (mm)	Hole diameter (mm)	Aspect ratio
Template 1	5.0	1.5	3.33
Template 2	10.0	1.5	6.67
Template 3	10.0	0.5	20

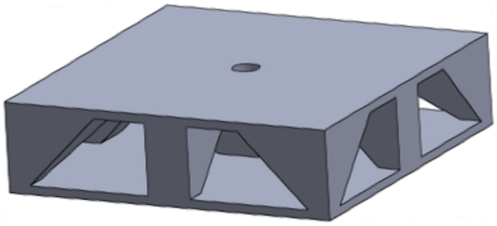

Figure 6.1. Representative CAD drawing of a 3D-printed template used for grain selection. The open structure provides additional insulation between the top and bottom plates to prevent unwanted nucleation.

6.2.3. Pore Alignment Analysis

Low magnification images used to determine the degree of pore alignment for each sample were obtained by stitching six SEM micrographs together. An image processing software was then used to segment each pore domain and color-code them according to one of the three following classifications - pore domains aligned parallel to the freezing axis, pore domains off-axis to the freezing axis, or domain boundaries. The number of pixels within each segmented domain was recorded and normalized with the pixel count of the total image to obtain the percent area occupied by each domain.

Water permeability measurements were also performed on each sample according to the experimental setup and procedure described in Chapter 5. Similar to previous tests, the Darcian permeability constant was calculated according to Equation 5.1 and the non-Darcian permeability constant was excluded due to low flow rates and linear flow behavior.

6.3. Results and Discussions

6.3.1. Improved Pore Alignment via Grain-selection Templates

Effect of Grain-selection Templates on Dendritic Pore Structures

Figure 6.2 shows the transverse view of a typical dendritic pore structure obtained from conventional freeze casting with cyclohexane as a solvent. First, Figure 6.2(a) shows a group, or *domain*, of primary dendrites which are aligned parallel to the temperature gradient applied during freeze casting. However, a lower magnification image (Fig. 6.2(b)) shows a more representative structure of the freeze cast samples on a larger scale. While many pores align upward according to the temperature gradient (area 1), there are also pore domains which grow off-axis (area 2), and boundaries between each domain (area 3).

Figure 6.3 shows the evolution of the pore structure with respect to the different templates used. The extremely low magnification images are used to ensure that each image is representative of the whole sample and not biased toward a small and specific area. While this might present a challenge to identify individual pores, pores that are directly aligned with the freezing axis can be detected as dark spots. Figure 6.3(a) shows that the control sample cast without a template contains very few areas with pores which

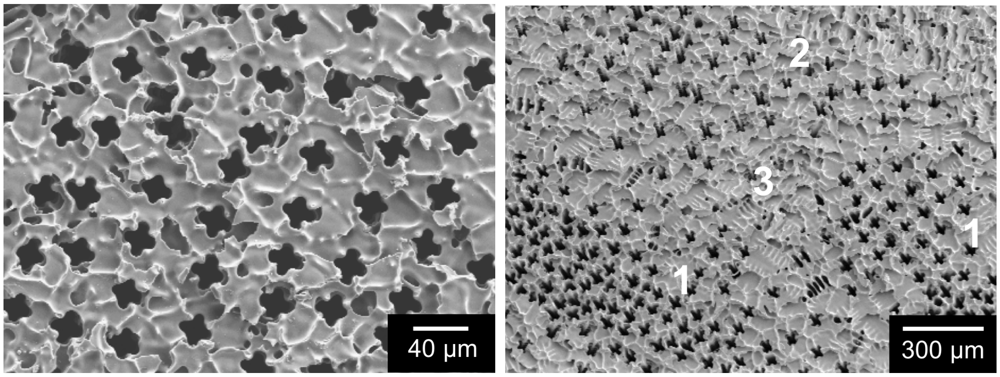

(a) High magnification (b) Low magnification

Figure 6.2. Representative SEM micrographs of the dendritic pore structure from cyclohexane with (a) high magnification image showing a single domain, and (b) low magnification image showing a less uniform microstructure consisting of areas that can be classified as aligned porosity (area 1), off-axis porosity (area 2), and domain boundaries (area 3).

are aligned directly parallel with the temperature gradient. The majority of the area is composed of pore domains which are aligned slightly off-axis, and therefore are difficult to see when looking at a direct transverse cross-section. Since so many cyclohexane crystals have been allowed to nucleate on the cold surface, this degree of misalignment is understandable. However, Figure 6.3(b) shows that once Template 1 is used and a grain selection process occurs, nuclei are forced to grow in a very constrained area and a significant improvement in alignment is observed. The sample now contains numerous large domains with pores highly aligned to the freezing direction. Figure 6.3(c) shows that alignment improves further when Template 2 is used and the column height is increased from 5 mm to 10 mm. In this case, the increased height allows for more off-axis cyclohexane crystals to be eliminated throughout the course of the template, resulting in even larger and more aligned pores. Domains with aligned pores span several millimeters and cover most of the sample, leaving only a few off-axis domains. Lastly, the improving

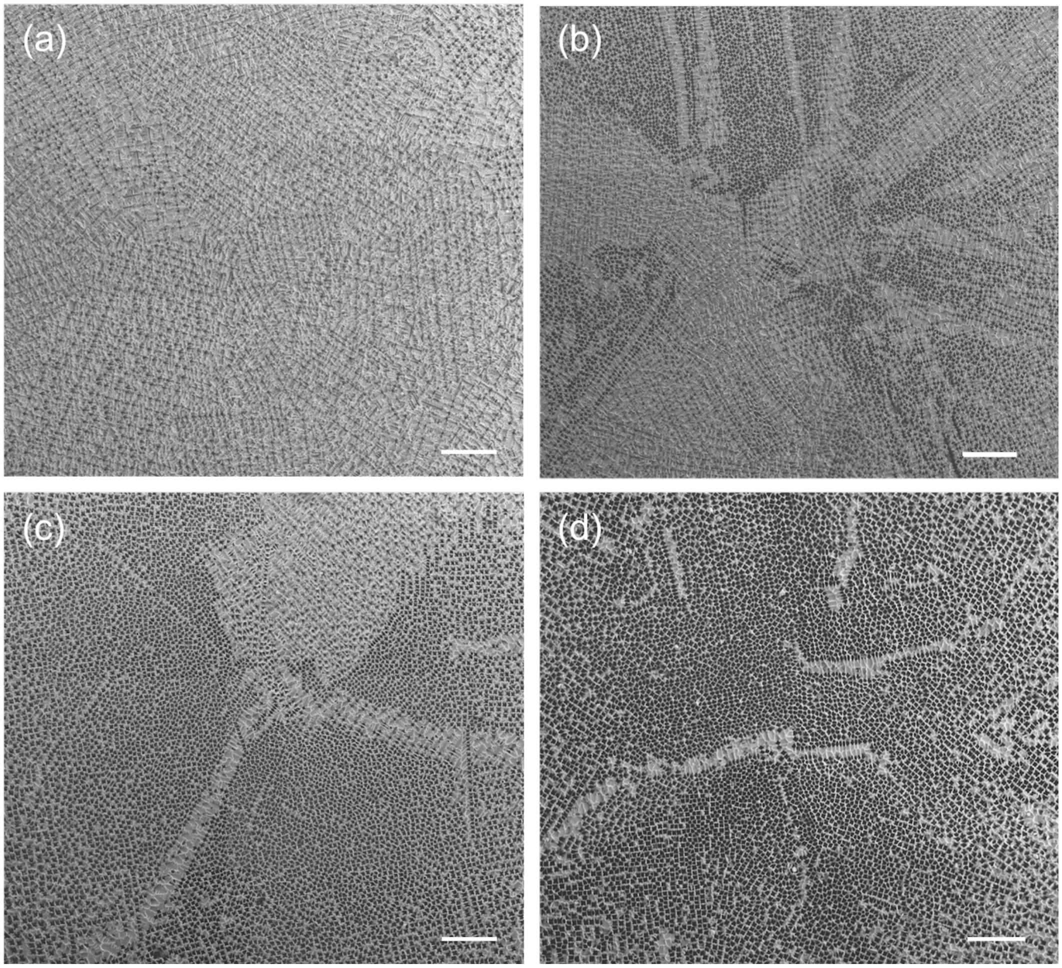

Figure 6.3. Low magnification SEM images of pore structures from (a) the control sample, (b) Template 1, (c) Template 2, and (d) Template 3. Scale bar = 1 mm.

trend continues in Figure 6.3(d) when the diameter of the column is reduced to 0.5 mm with Template 3. Here, we produce a sample with no distinguishable solvent crystals that have grown off-axis, resulting in fully aligned pores along the temperature gradient. The reduced diameter of the column proves to effectively decrease the number of nucleation sites, enhancing the grain selection process along the height of the column. However, despite this highly ordered pore structure, the cyclohexane did not seem to grow as a single crystal and boundaries are still present, producing the various pore domains seen in Figure 6.3(d). These are low-angle boundaries or neighboring cyclohexane crystals that are rotated with respect to one another.

Higher magnification micrographs of certain areas from Figure 6.3 are shown in Figure 6.4, such that the various features become more distinguishable. Figure 6.4(a) shows an area where the dendrite domain is fully aligned along the temperature gradient. Interestingly, certain regions of templated samples, such as the one shown here, contain dendrites domains which are closely packed and appear to be more cellular than those seen from conventional freeze casting (Fig. 6.2(a)). It is possible the use of a grain selection template results in larger dendritic crystals being grown, affecting their arrangement and consequently their shape. The left area of Figure 6.4(b) shows an area of dendrites aligned parallel to the thermal gradient, which meets with a different domain from the right side consisting of off-axis dendrites. Lastly, Figure 6.4(c) shows two large on-axis domains separated by a domain boundary. These are the domains alluded to in the previous paragraphs that could be generated due to low-angle boundaries or rotated crystals.

The increase in pore alignment from Figure 6.3(a) to Figure 6.3(d) may give an impression that the pore fraction has increased incrementally from one template to another,

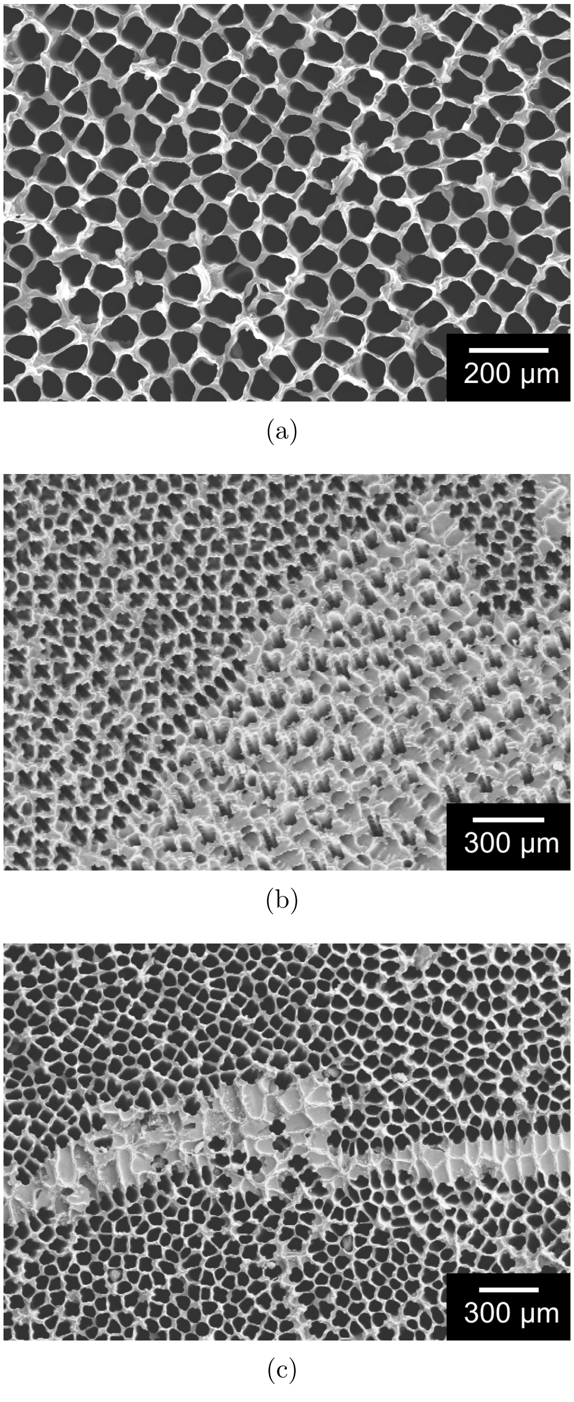

Figure 6.4. Higher magnification micrographs of certain areas of samples freeze cast with a grain-section template. (a) A domain aligned parallel to the thermal gradient, (b) on- and off-axis domains adjacent to each other, (c) a domain boundary between two on-axis domains.

however, this is not the case. As mentioned earlier, all samples were produced with the same polymer concentration, and therefore, have similar porosities. This illusion is simply a product of the pores being increasingly visible in the transverse cross-section as they become more aligned to the temperature gradient, with Figure 6.4(b) providing a good example of this scenario.

It is also noteworthy to mention that an additional sample was made with a template where no air insulation between the top and bottom surfaces was incorporated. The template is merely a solid polymeric block 10 mm tall, with a hollow column of 1.5 mm in diameter at the center. The resulting pore structure was largely identical to the control sample (Fig. 6.3(a)) with mostly off-axis pore domains. Presumably, heat was conducted through the entire surface of the template rather than just the column, allowing nucleation to occur throughout the base of the sample as it did with the control scenario. This proves that a sufficient amount of insulation is required between the base of the sample and the cold plate in order to confine nucleation exclusively to the column area. While acrylate polymers like the one used in this study are generally good insulators, their thermal conductivity is still roughly an order of magnitude greater than that of air.[135]

Quantifying Pore Alignment

Image analysis was used to quantify the amount of change in pore alignment attributed to each template. Each image from Figure 6.3 is segmented into the three separate types of domains highlighted in Figure 6.4(c); (i) domains parallel to the freezing axis, (ii) domains off-axis to the freezing axis, and (iii) domain boundaries. Figure 6.5 shows each type of domain color-coded as green, purple, and orange, respectively. Here, the evolution of the microstructure through the different templates becomes more evident as the percentage of off-axis domains (purple) gradually decrease and are replaced with aligned pores (green). While most domains are distinguishable and contain boundaries between them, certain areas contain crystals rotated by low angles that barely show any boundary and can be difficult to discern.

The total percent area occupied by each type of domain is listed in Table 6.2. A significant increase in pore alignment from the control sample is clearly observed as grain selection templates are used, and the effectiveness increases in conjunction with the aspect ratio of the each template. The largest increase in percent of on-axis area (from 13.9 to 92.6%) and decrease in off-axis area (from 65.7 to 0%) comes from the transition between the control sample to that of Template 3. However, the largest incremental increase from one condition to the next comes from the control sample to Template 1. In this case, the percent of on-axis area increased from 13.9 to 58.6% and the off-axis area decreased from 65.7 to 25.2%. This result shows that the use of a grain selection template is very effective even if the template does not have the ideal dimensions. Moreover, a gradual decrease in percent area occupied by boundaries is observed as the effectiveness of the template increases. This is possibly indicative of a decrease in the number of solvent crystals nucleated, consequently producing fewer domain boundaries.

As a complementary test of pore alignment, permeability measurements were performed on samples made from each condition using deionized water as the flowing fluid. Figure 6.6 shows the measured values for samples from this study (black diamond), plotted with the results from Chapter 5, where the diamond marker with the lowest permeability

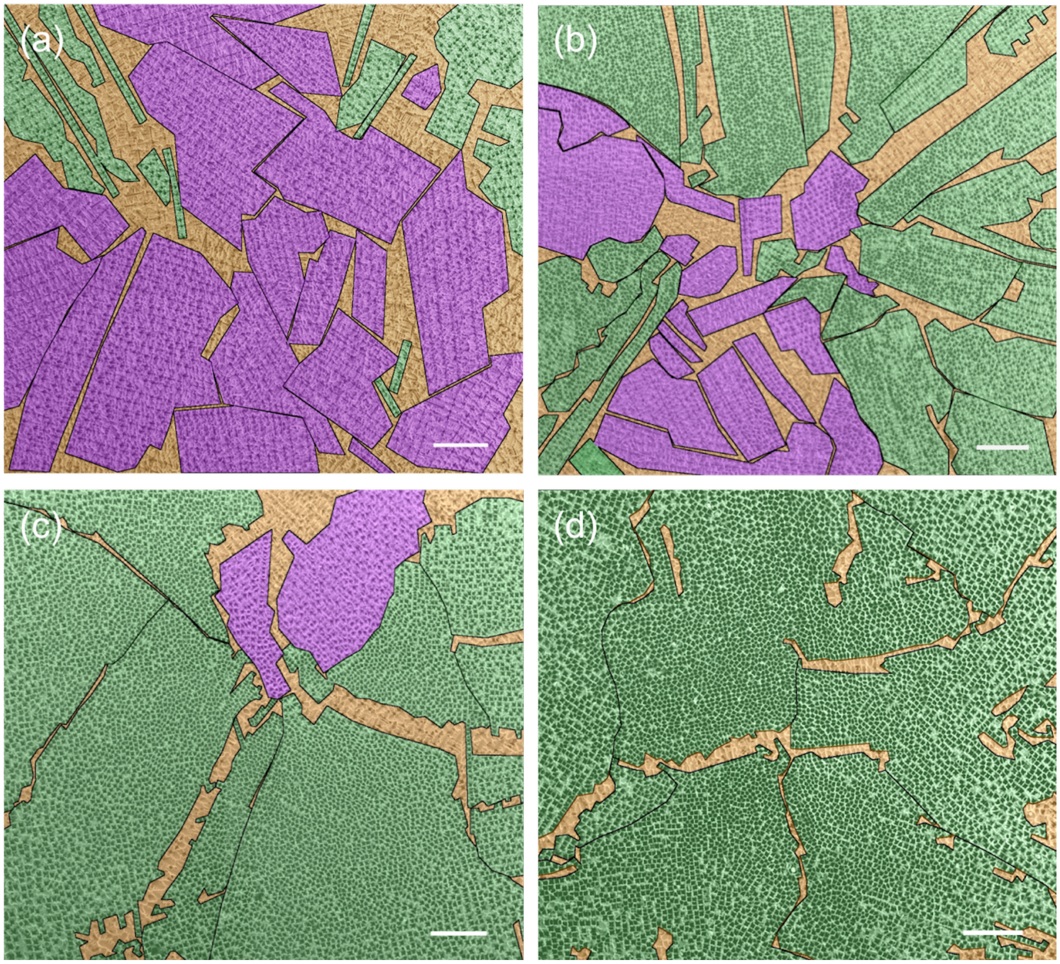

Figure 6.5. Segmented and colored SEM images (from Fig. 6.3) of pore structures from (a) the control sample, (b) Template 1, (c) Template 2, and (d) Template 3. Each color represents particular features in the pore structure; pores parallel to the freezing axis (green), off-axis pores (purple), and domain boundaries (orange). Scale bar = 1 mm.

Table 6.2. Percent area occupied by each type of pore domain for each template used, compared with a control sample. Area calculations are based on the segmented areas shown in Fig. 6.5.

	Percent area parallel to freezing direction	Percent area off-axis to freezing direction	Percent area of boundaries
Control	13.9	65.7	20.4
Template 1	58.6	25.2	16.2
Template 2	79.8	9.3	10.9
Template 3	92.6	0	7.4

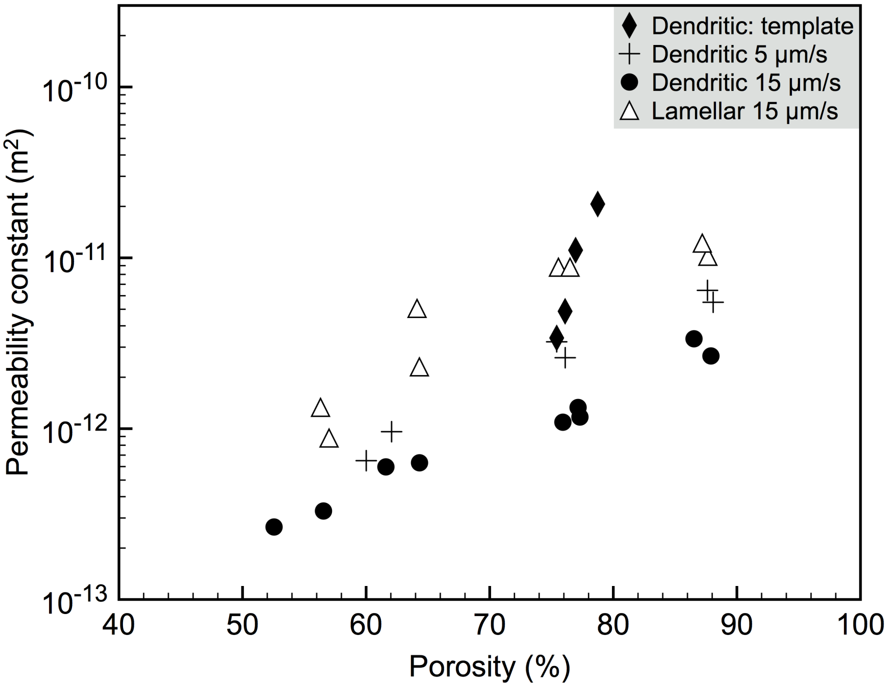

Figure 6.6. Permeability measurement results of samples freeze cast with grain-selection templates, plotted with various conventionally freeze cast dendritic and lamellar samples from Figure 5.10. Black diamond markers corresponds to samples from this study, with the lowest permeability representing the control sample and samples from Template 1, 2, and 3 yielding progressively higher permeability constants.

constant represents the control sample, and samples from Templates 1, 2, and 3 corresponds to progressively higher permeability constants. This shows that the flow properties behave as expected in concert with results from image analysis: increased pore alignment proves to increase water permeability. As all these samples were made with a freezing front velocity of 5 µm/s, results from the control sample expectedly fall in line with the previous study. The change in flow behavior from the control sample ($k_1 = 3.4 \times 10^{-12}$ m^2) to the Template 3 sample ($k_1 = 2.1 \times 10^{-11}$ m^2) is also significant - a more than six-fold increase. Notably, Template 3 produced a dendritic structure which yielded a higher permeability constant than the highly permeable lamellar samples from Chapter 5.

6.4. Conclusions

This study showed that the use of grain selection templates allows for greater control over the nucleation process in freeze casting, consequently improving pore alignment along the freezing axis. Three different types of 3D-printed templates with varying heights and column diameters were used and compared with a conventionally freeze cast control sample. Templates with higher aspect ratio holes (from 3.33:1 to 20:1) proved to be more effective in eliminating off-axis crystal growth and significantly improved the directionality of the pores. Image analysis was used to quantify the changes in the pore structures and results showed that the percent of pore domains aligned parallel to the freezing axis increased from 14 to 93%. Additionally, results from water permeability measurements show substantial improvements in flow properties as pore domains become more aligned. These improvements in pore alignment due to the use of grain selection templates show that controlling solvent crystal nucleation is crucial in freeze casting and should be taken into more consideration when trying to produce anisotropic and directionally-aligned pore structures.

CHAPTER 7

Summary, Conclusions, and Future Work

7.1. Summary and Conclusions

Solution-based freeze casting of preceramic polymers was demonstrated to be a promising technique for producing directionally porous ceramics. A broad scope of the technique was covered, beginning from the processing details and sample fabrication, to the control and characterization of various freeze cast pore structure, and finally to the evaluation of various structures' functional performances.

A commercially available polymethylsiloxane preceramic polymer was freeze cast with seven different organic solvents to obtain porous silicon oxycarbide (SiOC) with isotropic, dendritic, prismatic, and lamellar pore morphologies. SiOC ceramics with open porosities of roughly 50 to 95% were produced, corresponding to bulk densities of 1.2 to 0.1 g/cm^3, respectively. By controlling processing parameters such as the solvent choice, freezing front velocity, and polymer concentration, the pore structure of freeze cast samples can be carefully manipulated. For the conditions used in this study, solvent choice was shown to dictate the pore morphology produced. The Jackson α-factor of each solvent, along with optical micrographs of solidifying polymer solutions, were used to explain the various pore structures produced. Changes in the freezing front velocity showed that pore size can be carefully controlled, while polymer concentration influenced pore size and connectivity, but naturally also affected the porosity. The effects of these changes in the pore structure are strongly dictated by fundamental solidification principles and can be explained through concepts such as the freezing front instability and the interfacial anisotropy of each solvent.

Freeze casting with preceramic polymers necessitated adjustments from conventional suspension-based freeze casting, including polymer-solvent dissolution and cross-linking of the preceramic polymer. The solution-based system however introduces new capabilities and benefits to the technique, proving to be a more facile processing method and also enabling direct observation of the freezing front. Moreover, the absence of suspended particles in solution-based systems was shown to affect the pore morphologies produced. Dendritic structures produced from cyclohexane and dioxane as solvents were significantly more well-defined and directional in solution-based samples due to the lack of noise ahead of the freezing front caused by small particles. Lamellar structures produced from dimethyl carbonate did not show any discernible change, possibly due to the faceted growth interface being more stable.

The properties of various pore structures generated from freeze casting were then compared by calculating their specific surface area, compressive strength, and permeability constant. Geometric specific surface area results obtained from X-ray computed tomography data showed that samples which contained pore morphologies with rougher features (e.g. dendrites) produced higher surface areas than smooth and faceted morphologies (e.g. prismatic and lamellar). Additionally, compression tests showed that cyclohexane-based dendritic structures were significantly stronger than dimethyl carbonate-based lamellar structures, presumably due to differences in the connectivity of the pore walls. The compressive strength of dendritic samples ranged from roughly 1 to 100 MPa, with 90 to 50% open porosity, respectively. In comparison, lamellar structures had compressive strengths of only 1 to 3 MPa. However, lamellar structures were significantly more permeable to fluid flow due to their two-dimensional structure. An exception existed, as dendritic samples which were freeze cast with grain-selection templates, introduced as a method to increase the pore alignment, yielded highly aligned dendritic pores which resulted in improved permeability properties. Grain-selection templates were shown to successfully reduce the number of solvent crystals and improve the pore alignment, where the percent area of pores parallel to the freezing direction increased from 13.9% in the control sample to 92.6% in the sample freeze cast with the most effective grain-selection template.

7.2. Suggestions for Future Work

7.2.1. Incorporating Hierarchical Porosity

A limitation freeze casting faces as a processing technique is its inability to produce multiple types of pores within a single sample. Moreover, pores generated through this method are limited to sizes ranging from roughly 5 to 200 µm, frequently aimed at providing functions such as fluid flow. In order to increase the utility of freeze cast materials, features spanning multiple length scales are desired. These type of materials are also known as hierarchically porous structures, often possessing nanometer-sized features which contribute to additional functionality. A review by Sun et al. covers the motivation for creating hierarchically porous structures and discusses their potential applications; numerous processing techniques for incorporating these features are also introduced.[136]

Some preliminary studies have been performed in this work to increase the surface area of freeze cast structures, exploring methods such as partial pyrolysis of preceramic polymers and nanowire growth on pore walls. Partial pyrolysis is a technique explored by Wilhelm et al. where the innate characteristics of preceramic polymers can be used to create nanometer-sized pores.[137] In this technique, preceramic polymers are pyrolyzed to a relatively low temperature, where pores are created from escaping volatile gases. Higher temperatures must be avoided as it initiates densification which eliminates the pores. Since these structures are not fully converted into a ceramic, they are fittingly coined as *ceramers*. Figure 7.1 shows BET gas adsorption results obtained from our study's cyclohexane-based freeze cast samples, pyrolyzed to various temperatures. The ceramer sample pyrolyzed to 600 °C yielded a high specific surface area of 600 m^2/g, indicating the presence of nanometer-sized pores. Samples pyrolyzed to 1100 °C and 1400 °C resulted in a densified ceramic with low specific surface areas (12 and 20 m^2/g, respectively) representative of macropores. While this method may seem effective, the sample pyrolyzed to 600 °C was extremely fragile and effectively unusable. For these samples, dibutyltin dilaurate was used as the cross-linking agent, and a simple pyrolysis step of 5 °C/min up to 600 °C for 4 hours was employed. Future studies could explore changes in the processing conditions in which a robust hierarchically porous structure can be created via partial pyrolysis. Nevertheless, the fact that these structures cannot operate at higher temperatures may be a concern for certain applications.

Additionally, we have achieved growth of nanowires within the freeze-cast SiOC by applying a similar procedure to the one explored by Colombo et al. for foam structures.[88] To create SiC nanowire-decorated freeze-cast SiOC, cobalt-based catalysts were mixed

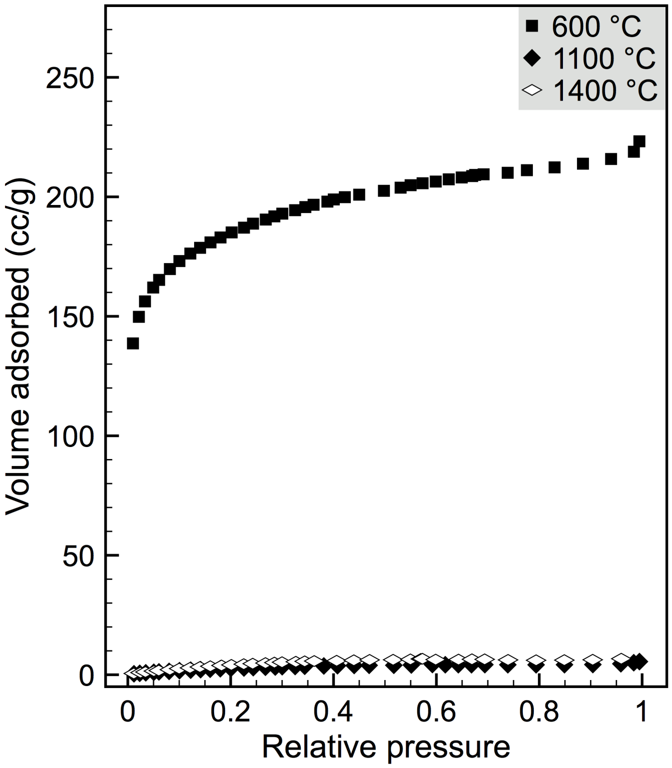

Figure 7.1. Nitrogen adsorption curves used to calculate the BET surface area of MK preceramic polymer pyrolyzed at various temperatures. The partially pyrolyzed sample showed a high specific surface area attributed to micropores generated from gaseous species escaping.

into cyclohexane-MK powder solutions, after which conventional freeze casting and freeze drying methods were used. The polymeric structure was then pyrolyzed in an argon atmosphere and held at a higher temperature of 1400 °C for 4 hours to initiate nanowire growth. Figure 7.2(a) shows a sample where nanowires are seen growing from the walls and extending into dendritic pores, created by incorporating $CoCl_2$ as a catalyst; $CoCl_2$ did not dissolve in cyclohexane and ball milling was required to disperse the particles. In contrast, Figure 7.2(b) shows a cluster of nanowires in a sample made with cobalt acetylacetonate, where the catalyst was fully dissolved by cyclohexane and a homogenous purple solution was obtained prior to freeze casting.

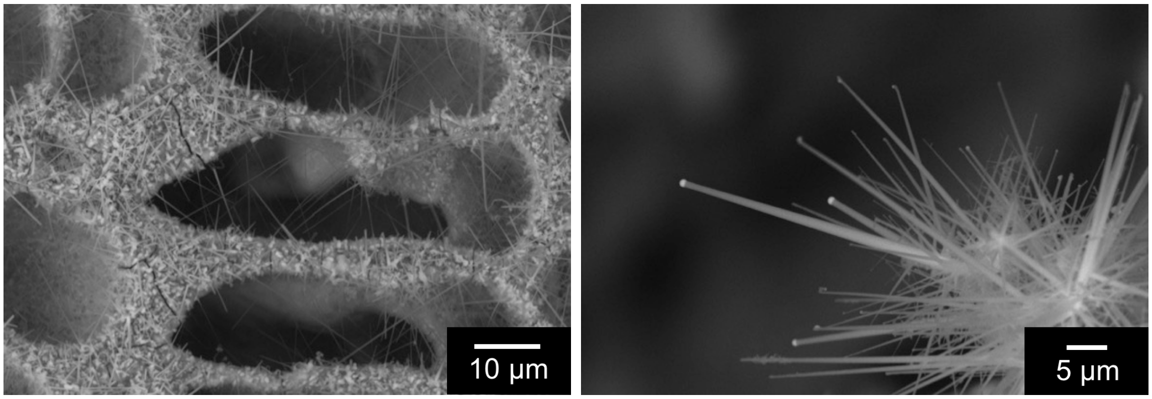

(a) (b)

Figure 7.2. SEM micrographs of nanowires grown in freeze-cast dendritic structures, creating hierarchically porous materials.

Nevertheless, both types of catalysts yielded samples with inhomogeneous nanowire growth and damaged pore walls. While nanowires were observed in certain areas of the sample, other areas contained whiskers larger than several microns, or simply bare walls. This inconsistency was attributed to poor gas flow within the sample during pyrolysis which resulted in an uneven distribution of the reactants required for nanowire growth. Moreover, the growth of these nanowires is accompanied by carbothermal reduction of the SiOC, damaging the pore walls and compromising the mechanical integrity. Future studies should address these issues to create a more homogeneous and defect-free sample. The effect of nanowires on the specific surface area can also be investigated via gas adsorption techniques. Additionally, mechanical tests can be performed to determine if the strength can be maintained, or possibly increased, compared to results from Chapter 5.

Other possible techniques to incorporate hierarchical porosity to freeze cast structures include taking advantage of processes such as gelation or phase separation. For example, mesoporous colloidal structures can be created via a gelation and supercritical drying process, similar to the production of aerogels. With this method, Zera et al. used polycarbosilane as a preceramic polymer to create ceramics with a specific surface area of 444 m^2/g and a compressive strength of 1.6 MPa.[138] However, innovative processing techniques would have to be implemented to integrate freeze casting with this technique. In particular, a two-component system might be created where one component would independently undergo solidification while the other gels. Additionally, the effects of supercritical drying, as opposed to conventional freeze drying, on the freeze cast pore structure should also be investigated. A similar technique was employed by Samitsu et al., creating mesoporosity via flash freezing and cold crystallization in polymeric systems.[41] A concern for using this method with preceramic polymers is the possibility of the mesopores being eliminated during pyrolysis as densification occurs, similar to what happens with partial pyrolysis. Future studies should integrate this technique with preceramic polymer freeze casting and determine if the mesopores can be retained. Lastly, a secondary polymer such as PDMS could be incorporated into the preceramic polymer solution to act as another sacrificial phase in addition to the ice crystals. During freeze casting, the PDMS should be exsolved by the ice crystals and distributed throughout the preceramic polymer, where it can be removed upon pyrolysis to create mesopores within the pore walls.

7.2.2. Improved Solidification Control

Various sections of this work have alluded to the limited control of solidification parameters possible in most freeze casting studies. Despite freeze-cast pore structures being heavily dependent on the solidification conditions, there is a shortage of setups which can independently control the temperature gradient across the solid-liquid interface and the freezing velocity. Current setups rely solely on thermal conductivity across the thickness of the solidified sample to determine the solidification conditions at the interface. Variations of the Czochralski, Bridgman, or Stockbarger processes used in single crystal semiconductor processing could be implemented to solve this issue by providing independent control of the two solidification parameters. However, these methods introduce radial temperature gradients which may affect the directionality of the freeze cast structures. While a simpler setup with thermoelectric devices placed on the top as well as the bottom of the casting mold enables improved control, the two processing variables remain indirectly controlled.

Better control of the solidification conditions will not only improve pore size control, but could also enable transitions in the solidification microstructure currently unachievable during freeze casting. For example, while cyclohexane is currently used to produce dendritic pores in solution-based systems, a transition to cellular growth can be achieved with a higher temperature gradient across the solid-liquid interface. This not only allows for a single solvent to create various pore morphologies, but could also allow for microstructural gradients to be created, where a unimodal cellular structure is generated in one half of the sample and a bimodal or trimodal dendritic structure in the other.

The use of preceramic polymers can also improve control over the solidification process by introducing viscosity as another processing parameter. While the effect of viscosity on freeze-cast pore networks has been investigated in aqueous-based suspensions, it has been achieved through the addition of compounds such as polyethylene glycol.[122] The addition of these compounds can introduce ambiguity to the root cause of the changes in the structure. In contrast, the viscosity, and consequently the diffusion coefficient, of polymer solutions can be manipulated by controlling the degree of cross-linking and molecular weight of the polymer simply via thermal curing.

7.2.3. Alternative Precursors

While this study has selected to use polysiloxanes as the model preceramic polymer due to their chemical stability and commercial availability, other types of preceramic polymers should also be explored as precursors to freeze-cast ceramics. In addition to the polysiloxane used here, Yoon et al. showed that a solid polycarbosilane preceramic polymer can be freeze cast with camphene and cross-linked thermally, without the addition of a cross-linking agent, to obtain SiC with dendritic pores.[97,139] Nevertheless, future studies should investigate the effects of using different types of preceramic polymers under identical processing conditions to provide new insights to the technique. Doing so will help determine whether various aspects of the processing technique can be seamlessly transferred to new material systems, or whether certain polymer characteristics affects the processing requirements. The effects of changes in the type of polymer on the pore size or pore morphology can also be investigated. Moreover, a wider variety of phase compositions can be chosen to suit particular applications.

7.2.4. Infiltration of Porous Structures

In addition to the usual functions pores provide, they can also be infiltrated with a second phase to create composite materials. Lamellar pore structures obtained from freeze casting are often compared to nacre, holding promises as use for tough, bio-inspired materials.[140] For example, Munch et al. showed that freeze-cast lamellar structures infiltrated with PMMA can yield a material with high strength and toughness attributable to the unique layered structure providing crack deflection.[141] As numerous other pore morphologies have been generated from freeze casting, a new study could investigate the mechanical properties and fracture behavior of composites made with prismatic, cellular, or dendritic structures and determine if interesting toughening mechanisms emerge.

References

[1] Gary L. Messing and Adam J. Stevenson. Toward Pore-Free Ceramics. *Science*, 322(5900):383–384, 2008.

[2] Marc André Meyers, Po-Yu Chen, Albert Yu-Min Lin, and Yasuaki Seki. Biological materials: Structure and mechanical properties. *Progress in Materials Science*, 53(1):1–206, 2008.

[3] B. A. Haberman and J. B. Young. Three-dimensional simulation of chemically reacting gas flows in the porous support structure of an integrated-planar solid oxide fuel cell. *International Journal of Heat and Mass Transfer*, 47(17–18):3617–3629, 2004.

[4] Joseph R. Woodard, Amanda J. Hilldore, Sheeny K. Lan, C. J. Park, Abby W. Morgan, Jo Ann C. Eurell, Sherrie G. Clark, Matthew B. Wheeler, Russell D. Jamison, and Amy J. Wagoner Johnson. The mechanical properties and osteoconductivity of hydroxyapatite bone scaffolds with multi-scale porosity. *Biomaterials*, 28(1):45–54, 2007.

[5] Steffen Heidenreich. Hot gas filtration – A review. *Fuel*, 104:83–94, 2013.

[6] Michael Scheffler and Paolo Colombo. *Cellular Ceramics: Structure, Manufacturing, Properties and Applications*. John Wiley & Sons, 2006.

[7] Paolo Colombo. Engineering porosity in polymer-derived ceramics. *Journal of the European Ceramic Society*, 28(7):1389–1395, 2008.

[8] Ulrike G. K. Wegst, Matthew Schecter, Amalie E. Donius, and Philipp M. Hunger. Biomaterials by freeze casting. *Philosophical Transactions of the Royal Society A: Mathematical, Physical and Engineering Sciences*, 368(1917):2099–2121, 2010.

[9] André R. Studart, Urs T. Gonzenbach, Elena Tervoort, and Ludwig J. Gauckler. Processing Routes to Macroporous Ceramics: A Review. *Journal of the American Ceramic Society*, 89(6):1771–1789, 2006.

[10] M. T. Johnson and K. T. Faber. Catalytic graphitization of three-dimensional wood-derived porous scaffolds. *Journal of Materials Research*, 26(1):18–25, 2011.

[11] Kiyoshi Okada, Toshihiro Isobe, Ken-ichi Katsumata, Yoshikazu Kameshima, Akira Nakajima, and Kenneth J. D. MacKenzie. Porous ceramics mimicking nature—preparation and properties of microstructures with unidirectionally oriented pores. *Science and Technology of Advanced Materials*, 12(6):064701, 2011.

[12] David J. Green and P. Colombo. Cellular Ceramics: Intriguing Structures, Novel Properties, and Innovative Applications. *MRS Bulletin*, 28(4):296–300, 2003.

[13] Kiyoshi Araki and John W. Halloran. Porous Ceramic Bodies with Interconnected Pore Channels by a Novel Freeze Casting Technique. *Journal of the American Ceramic Society*, 88(5):1108–1114, 2005.

[14] Sylvain Deville, Eduardo Saiz, Ravi K. Nalla, and Antoni P. Tomsia. Freezing as a Path to Build Complex Composites. *Science*, 311(5760):515–518, 2006.

[15] W L Li, K Lu, and J Y Walz. Freeze casting of porous materials: Review of critical factors in microstructure evolution. *International Materials Reviews*, 57(1):37–60, 2012.

[16] Philipp M. Hunger, Amalie E. Donius, and Ulrike G. K. Wegst. Structure–property-processing correlations in freeze-cast composite scaffolds. *Acta Biomaterialia*, 9(5):6338–6348, 2013.

[17] M. Naviroj, S. M. Miller, P. Colombo, and K. T. Faber. Directionally aligned macroporous SiOC via freeze casting of preceramic polymers. *Journal of the European Ceramic Society*, 35(8):2225–2232, 2015.

[18] Jordi Seuba, Sylvain Deville, Christian Guizard, and Adam J. Stevenson. Mechanical properties and failure behavior of unidirectional porous ceramics. *Scientific Reports*, 6, 2016.

[19] S. Deville. Freeze-Casting of Porous Ceramics: A Review of Current Achievements and Issues. *Advanced Engineering Materials*, 10(3):155–169, 2008.

[20] Sylvain Deville. Ice-templating, freeze casting: Beyond materials processing. *Journal of Materials Research*, 28(17):2202–2219, 2013.

[21] Stephen S. L. Peppin, M. Grae Worster, and J. S. Wettlaufer. Morphological instability in freezing colloidal suspensions. *Proceedings of the Royal Society of London A: Mathematical, Physical and Engineering Sciences*, 463(2079):723–733, 2007.

[22] Yasumasa Chino and David C. Dunand. Directionally freeze-cast titanium foam with aligned, elongated pores. *Acta Materialia*, 56(1):105–113, 2008.

[23] Sylvain Deville, Eduardo Saiz, and Antoni P. Tomsia. Ice-templated porous alumina structures. *Acta Materialia*, 55(6):1965–1974, 2007.

[24] D. R. Uhlmann, B. Chalmers, and K. A. Jackson. Interaction Between Particles and a Solid-Liquid Interface. *Journal of Applied Physics*, 35(10):2986–2993, 1964.

[25] Dipankar Ghosh, Mahesh Banda, Hyungsuk Kang, and Nikhil Dhavale. Platelets-induced stiffening and strengthening of ice-templated highly porous alumina scaffolds. *Scripta Materialia*, 125:29–33, 2016.

[26] Sylvain Deville. *Freezing Colloids: Observations, Principles, Control, and Use: Applications in Materials Science, Life Science, Earth Science, Food Science, and Engineering.* Springer, 2017.

[27] Jessica C. Li and David C. Dunand. Mechanical properties of directionally freeze-cast titanium foams. *Acta Materialia*, 59(1):146–158, 2011.

[28] Ranier Sepúlveda, Amelia A. Plunk, and David C. Dunand. Microstructure of Fe2O3 scaffolds created by freeze-casting and sintering. *Materials Letters*, 142:56–59, 2015.

[29] Hyungyung Jo, Min Jeong Kim, Hyelim Choi, Yung-Eun Sung, Heeman Choe, and David C. Dunand. Morphological Study of Directionally Freeze-Cast Nickel Foams. *Metallurgical and Materials Transactions E*, 3(1):46–54, 2016.

[30] Haifei Zhang, Irshad Hussain, Mathias Brust, Michael F. Butler, Steven P. Rannard, and Andrew I. Cooper. Aligned two- and three-dimensional structures by directional freezing of polymers and nanoparticles. *Nature Materials*, 4(10):787–793, 2005.

[31] Michael Barrow, Ali Eltmimi, Adham Ahmed, Peter Myers, and Haifei Zhang. Frozen polymerization for aligned porous structures with enhanced mechanical stability, conductivity, and as stationary phase for HPLC. *Journal of Materials Chemistry*, 22(23):11615–11620, 2012.

[32] Mohamed N. Rahaman and Qiang Fu. Manipulation of Porous Bioceramic Microstructures by Freezing of Suspensions Containing Binary Mixtures of Solvents. *Journal of the American Ceramic Society*, 91(12):4137–4140, 2008.

[33] Rui Guo, Chang-An Wang, and Ankun Yang. Piezoelectric Properties of the 1–3 Type Porous Lead Zirconate Titanate Ceramics. *Journal of the American Ceramic Society*, 94(6):1794–1799, 2011.

[34] Jiecai Han, Changqing Hong, Xinghong Zhang, Jiancong Du, and Wei Zhang. Highly porous ZrO2 ceramics fabricated by a camphene-based freeze-casting route: Microstructure and properties. *Journal of the European Ceramic Society*, 30(1):53–60, 2010.

[35] Ruifeng Chen, Chang-an Wang, Yong Huang, Liguo Ma, and Weiyuan Lin. Ceramics with Special Porous Structures Fabricated by Freeze-Gelcasting: Using tert-Butyl Alcohol as a Template. *Journal of the American Ceramic Society*, 90(11):3478–3484, 2007.

[36] Hiroshi Chikama, Hiroyuki Shibata, Toshihiko Emi, and Mikio Suzuki. "<I>In-situ</I>" Real Time Observation of Planar to Cellular and Cellular to Dendritic Transition of Crystals Growing in Fe–C Alloy Melts. *Materials Transactions, JIM*, 37(4):620–626, 1996.

[37] Yukinobu Natsume, Kenichi Ohsasa, Hisao Esaka, and Toshio Narita. Analysis of Growth Behavior of a Cellular and Dendritic Interface under a Constrained Growth Condition using a Phase-Field Model. *Materials Transactions*, 44(5):824–828, 2003.

[38] Silvère Akamatsu and Henri Nguyen-Thi. In situ observation of solidification patterns in diffusive conditions. *Acta Materialia*, 108:325–346, 2016.

[39] Jordi Seuba, Sylvain Deville, Christian Guizard, and Adam J. Stevenson. The effect of wall thickness distribution on mechanical reliability and strength in unidirectional porous ceramics. *Science and Technology of Advanced Materials*, 17(1):128–135, 2016.

[40] Otávio F. L. da Rocha, Cláudio A. Siqueira, and Amauri Garcia. Theoretical - Experimental Analysis of Cellular and Primary Dendritic Spacings during Unidirectional Solidification of Sn-Pb Alloys. *Materials Research*, 5(3):391–397, 2002.

[41] Sadaki Samitsu, Rui Zhang, Xinsheng Peng, Mohan Raj Krishnan, Yoshihisa Fujii, and Izumi Ichinose. Flash freezing route to mesoporous polymer nanofibre networks. *Nature Communications*, 4:2653, 2013.

[42] Thomas Waschkies, Rainer Oberacker, and Michael J. Hoffmann. Control of Lamellae Spacing During Freeze Casting of Ceramics Using Double-Side Cooling as a Novel Processing Route. *Journal of the American Ceramic Society*, 92:S79–S84, 2009.

[43] Yufei Tang, Qian Miao, Sha Qiu, Kang Zhao, and Long Hu. Novel freeze-casting fabrication of aligned lamellar porous alumina with a centrosymmetric structure. *Journal of the European Ceramic Society*, 34(15):4077–4082, 2014.

[44] Etienne Munch, Eduardo Saiz, Antoni P. Tomsia, and Sylvain Deville. Architectural Control of Freeze-Cast Ceramics Through Additives and Templating. *Journal of the American Ceramic Society*, 92(7):1534–1539, 2009.

[45] Christopher M. Pekor, Predrag Kisa, and Ian Nettleship. Effect of Polyethylene Glycol on the Microstructure of Freeze-Cast Alumina. *Journal of the American Ceramic Society*, 91(10):3185–3190, 2008.

[46] Kai Hui Zuo, Yu-Ping Zeng, and Dongliang Jiang. Effect of polyvinyl alcohol additive on the pore structure and morphology of the freeze-cast hydroxyapatite ceramics. *Materials Science and Engineering: C*, 30(2):283–287, 2010.

[47] Congwang Ye, Anthony Chen, Paolo Colombo, and Carlos Martinez. Ceramic microparticles and capsules via microfluidic processing of a preceramic polymer. *Journal of The Royal Society Interface*, 7(Suppl 4):S461–S473, 2010.

[48] Michael M. Porter, Michael Yeh, James Strawson, Thomas Goehring, Samuel Lujan, Philip Siripasopsotorn, Marc A. Meyers, and Joanna McKittrick. Magnetic freeze casting inspired by nature. *Materials Science and Engineering: A*, 556:741–750, 2012.

[49] Y. F. Tang, K. Zhao, J. Q. Wei, and Y. S. Qin. Fabrication of aligned lamellar porous alumina using directional solidification of aqueous slurries with an applied electrostatic field. *Journal of the European Ceramic Society*, 30(9):1963–1965, 2010.

[50] Yumin Zhang, Luyang Hu, and Jiecai Han. Preparation of a Dense/Porous BiLayered Ceramic by Applying an Electric Field During Freeze Casting. *Journal of the American Ceramic Society*, 92(8):1874–1876, 2009.

[51] Kristen L. Scotti, Emily E. Northard, Amelia Plunk, Bryce C. Tappan, and David C. Dunand. Directional solidification of aqueous TiO2 suspensions under reduced gravity. *Acta Materialia*, 124:608–619, 2017.

[52] L. A. Tennenhouse, M. B. Koss, J. C. LaCombe, and M. E. Glicksman. Use of microgravity to interpret dendritic growth kinetics at small supercoolings. *Journal of Crystal Growth*, 174(1):82–89, 1997.

[53] A. Ludwig, J. Mogeritsch, M. Kolbe, G. Zimmermann, L. Sturz, N. Bergeon, B. Billia, G. Faivre, S. Akamatsu, S. Bottin-Rousseau, and D. Voss. Advanced Solidification Studies on Transparent Alloy Systems: A New European Solidification Insert for Material Science Glovebox on Board the International Space Station. *JOM*, 64(9):1097–1101, 2012.

[54] N. Bergeon, D. Tourret, L. Chen, J.-M. Debierre, R. Guérin, A. Ramirez, B. Billia, A. Karma, and R. Trivedi. Spatiotemporal Dynamics of Oscillatory Cellular Patterns in Three-Dimensional Directional Solidification. *Physical Review Letters*, 110(22):226102, 2013.

[55] W. Kurz and D. J. Fisher. *Fundamentals of Solidification*. CRC Press, Uetikon-Zuerich, Switzerland ; Enfield, N.H, 4th edition edition, 1998.

[56] Martin Eden Glicksman. *Principles of Solidification. [Electronic Resource] : An Introduction to Modern Casting and Crystal Growth Concepts*. New York, NY : Springer New York : Imprint: Springer, 2011., 2011.

[57] W. W. Mullins and R. F. Sekerka. Stability of a Planar Interface During Solidification of a Dilute Binary Alloy. *Journal of Applied Physics*, 35(2):444–451, 1964.

[58] J. S. Langer. Instabilities and pattern formation in crystal growth. *Reviews of Modern Physics*, 52(1):1–28, 1980.

[59] P. Kurowski, C. Guthmann, and S. de Cheveigné. Shapes, wavelength selection, and the cellular-dendritic "transition" in directional solidification. *Physical Review A*, 42(12):7368–7376, 1990.

[60] Stephen H. Davis. *Theory of Solidification*. Cambridge University Press, 2001. Google-Books-ID: UxTZCiyoFkQC.

[61] K. A. Jackson, D. R. Uhlmann, and J. D. Hunt. On the nature of crystal growth from the melt. *Journal of Crystal Growth*, 1(1):1–36, 1967.

[62] P. Bennema. Morphology of crystals determined by alpha factors, roughening temperature, F faces and connected nets. *Journal of Physics D: Applied Physics*, 26(8B):B1, 1993.

[63] Kenneth A. Jackson. Constitutional supercooling surface roughening. *Journal of Crystal Growth*, 264(4):519–529, 2004.

[64] Seishi Yajima, Josaburo Hayashi, and Mamoru Omori. Continuous Silicon Carbide Fiber of High Tensile Strength. *Chemistry Letters*, 4(9):931–934, 1975.

[65] S. Yajima, Y. Hasegawa, K. Okamura, and T. Matsuzawa. Development of high tensile strength silicon carbide fibre using an organosilicon polymer precursor. *Nature*, 273(5663):525–527, 1978.

[66] Peter Greil. Active-Filler-Controlled Pyrolysis of Preceramic Polymers. *Journal of the American Ceramic Society*, 78(4):835–848, 1995.

[67] Paolo Colombo, Gabriela Mera, Ralf Riedel, and Gian Domenico Sorarù. Polymer-Derived Ceramics: 40 Years of Research and Innovation in Advanced Ceramics. *Journal of the American Ceramic Society*, 93(7):1805–1837, 2010.

[68] Gabriela Mera, Alexandra Navrotsky, Sabyasachi Sen, Hans-Joachim Kleebe, and Ralf Riedel. Polymer-derived SiCN and SiOC ceramics – structure and energetics at the nanoscale. *Journal of Materials Chemistry A*, 1(12):3826, 2013.

[69] Ralf Riedel, Gabriela Mera, Ralf Hauser, and Alexander Klonczynski. Silicon-Based Polymer-Derived Ceramics: Synthesis Properties and Applications-A Review. *Journal of the Ceramic Society of Japan*, 114(1330):425–444, 2006.

[70] Anran Guo, Martina Roso, Michele Modesti, Jiachen Liu, and Paolo Colombo. Preceramic polymer-derived SiOC fibers by electrospinning. *Journal of Applied Polymer Science*, 131(3):n/a–n/a, 2014.

[71] P. Greil. Polymer Derived Engineering Ceramics. *Advanced Engineering Materials*, 2(6):339–348, 2000.

[72] Jeffrey A. Rahn, Richard M. Laine, and Zhi-Fan Zhang. The Catalytic Synthesis of Inorganic Polymers for High Temperature Applications and as Ceramic Precursors. In *Symposium O – Polymer Based Molecular Composites*, volume 171 of *MRS Online Proceedings Library*, 1989.

[73] Barry C. Arkles. Polysilane-siloxane oligomers and copolymers and methods of making the same, 1986. U.S. Classification 528/34, 528/25, 525/477, 528/33, 556/430; International Classification C08G77/48, C08G77/42, C08G77/00, C08G77/60; Cooperative Classification C08G77/485, C08G77/42, C08G77/48; European Classification C08G77/48B, C08G77/48, C08G77/42.

[74] Jan Kurjata and Julian Chojnowski. Equilibria and kinetics of the cationic ring-opening polymerization of permethylated 1,4-dioxa-2,3,5,6-tetrasilacyclohexane. Comparison with cyclosiloxanes. *Die Makromolekulare Chemie*, 194(12):3271–3286, 1993.

[75] M. Scheffler, T. Gambaryan-Roisman, T. Takahashi, J. Kaschta, H. Muenstedt, P. Buhler, and P. Greil. Pyrolytic decomposition of preceramic organo polysiloxanes. In N. Bansal and J. P. Singh, editors, *Innovative Processing and Synthesis of Ceramics, Glasses, and Composites Iv*, volume 115, pages 239–250. Amer Ceramic

Soc, Westerville, 2000. WOS:000171311000021.

[76] Q. Wei, E. Pippel, J. Woltersdorf, M. Scheffler, and P. Greil. Interfacial SiC formation in polysiloxane-derived Si–O–C ceramics. *Materials Chemistry and Physics*, 73(2–3):281–289, 2002.

[77] Rahul Harshe, Corneliu Balan, and Ralf Riedel. Amorphous Si(Al)OC ceramic from polysiloxanes: Bulk ceramic processing, crystallization behavior and applications. *Journal of the European Ceramic Society*, 24(12):3471–3482, 2004.

[78] Cekdar Vakifahmetoglu, Eckhard Pippel, Jörg Woltersdorf, and Paolo Colombo. Growth of One-Dimensional Nanostructures in Porous Polymer-Derived Ceramics by Catalyst-Assisted Pyrolysis. Part I: Iron Catalyst. *Journal of the American Ceramic Society*, 93(4):959–968, 2010.

[79] Carlo G. Pantano, Anant K. Singh, and Hanxi Zhang. Silicon Oxycarbide Glasses. *Journal of Sol-Gel Science and Technology*, 14(1):7–25, 1999.

[80] Atanu Saha, Rishi Raj, and Don L. Williamson. A Model for the Nanodomains in Polymer-Derived SiCO. *Journal of the American Ceramic Society*, 89(7):2188–2195, 2006.

[81] Atanu Saha and Rishi Raj. Crystallization Maps for SiCO Amorphous Ceramics. *Journal of the American Ceramic Society*, 90(2):578–583, 2007.

[82] Tamas Varga, Alexandra Navrotsky, Julianna L. Moats, R. Michelle Morcos, Fabrizia Poli, Klaus Müller, Atanu Saha, and Rishi Raj. Thermodynamically Stable SixOyCz Polymer-Like Amorphous Ceramics. *Journal of the American Ceramic Society*, 90(10):3213–3219, 2007.

[83] Hans-Joachim Kleebe and Yigal D. Blum. SiOC ceramic with high excess free carbon. *Journal of the European Ceramic Society*, 28(5):1037–1042, 2008.

[84] Adrian C. Wright. The Great Crystallite Versus Random Network Controversy: A Personal Perspective. *International Journal of Applied Glass Science*, 5(1):31–56, 2014.

[85] S. J. Widgeon, S. Sen, G. Mera, E. Ionescu, R. Riedel, and A. Navrotsky. 29Si and 13C Solid-State NMR Spectroscopic Study of Nanometer-Scale Structure and Mass Fractal Characteristics of Amorphous Polymer Derived Silicon Oxycarbide Ceramics. *Chemistry of Materials*, 22(23):6221–6228, 2010.

[86] Amir H. Tavakoli, Matthew M. Armentrout, Masaki Narisawa, Sabyasachi Sen, and Alexandra Navrotsky. White Si–O–C Ceramic: Structure and Thermodynamic Stability. *Journal of the American Ceramic Society*, pages n/a–n/a, 2014.

[87] Tian Liang, Ya-Li Li, Dong Su, and He-Bao Du. Silicon oxycarbide ceramics with reduced carbon by pyrolysis of polysiloxanes in water vapor. *Journal of the European Ceramic Society*, 30(12):2677–2682, 2010.

[88] Cekdar Vakifahmetoglu, Paolo Colombo, Sara Maria Carturan, Eckhard Pippel, and Jörg Woltersdorf. Growth of One-Dimensional Nanostructures in Porous Polymer-Derived Ceramics by Catalyst-Assisted Pyrolysis. Part II: Cobalt Catalyst. *Journal of the American Ceramic Society*, 93(11):3709–3719, 2010.

[89] Michael Adam, Cekdar Vakifahmetoglu, Paolo Colombo, Michaela Wilhelm, and Georg Grathwohl. Polysiloxane-Derived Ceramics Containing Nanowires with Catalytically Active Tips. *Journal of the American Ceramic Society*, 97(3):959–966, 2014.

[90] Jens Cordelair and Peter Greil. Electrical Characterization of Polymethylsiloxane/MoSi2-Derived Composite Ceramics. *Journal of the American Ceramic Society*, 84(10):2256–2259, 2001.

[91] Emanuel Ionescu, Christoph Linck, Claudia Fasel, Mathis Müller, Hans–Joachim Kleebe, and Ralf Riedel. Polymer-Derived SiOC/ZrO2 Ceramic Nanocomposites with Excellent High-Temperature Stability. *Journal of the American Ceramic Society*, 93(1):241–250, 2010.

[92] Emanuel Ionescu, Benjamin Papendorf, Hans-Joachim Kleebe, and Ralf Riedel. Polymer-Derived Silicon Oxycarbide/Hafnia Ceramic Nanocomposites. Part II: Stability Toward Decomposition and Microstructure Evolution at $T \gg 1000°C$. *Journal of the American Ceramic Society*, 93(6):1783–1789, 2010.

[93] M. Graczyk-Zajac, L. Toma, C. Fasel, and R. Riedel. Carbon-rich SiOC anodes for lithium-ion batteries: Part I. Influence of material UV-pre-treatment on high power properties. *Solid State Ionics*, 225:522–526, 2012.

[94] Ralf Riedel, Liviu Toma, Enrico Janssen, Jürgen Nuffer, Tobias Melz, and Holger Hanselka. Piezoresistive Effect in SiOC Ceramics for Integrated Pressure Sensors. *Journal of the American Ceramic Society*, 93(4):920–924, 2010.

[95] M. Schulz. Polymer derived ceramics in MEMS/NEMS – a review on production processes and application. *Advances in Applied Ceramics*, 108(8):454–460, 2009.

[96] Rui Zhuo, Paolo Colombo, Carlo Pantano, and Erwin A. Vogler. Silicon oxycarbide glasses for blood-contact applications. *Acta Biomaterialia*, 1(5):583–589, 2005.

[97] Byung-Ho Yoon, Eun-Jung Lee, Hyoun-Ee Kim, and Young-Hag Koh. Highly Aligned Porous Silicon Carbide Ceramics by Freezing Polycarbosilane/Camphene Solution. *Journal of the American Ceramic Society*, 90(6):1753–1759, 2007.

[98] Huixing Zhang, Pedro D'Angelo Nunes, Michaela Wilhelm, and Kurosch Rezwan. Hierarchically ordered micro/meso/macroporous polymer-derived ceramic monoliths fabricated by freeze-casting. *Journal of the European Ceramic Society*, 36(1):51–58, 2016.

[99] Tatsuhiro Takahashi, Joachim Kaschta, and Helmut Münstedt. Melt rheology and structure of silicone resins. *Rheologica Acta*, 40(5):490–498, 2001.

[100] Paolo Colombo and John R. Hellmann. Ceramic foams from preceramic polymers. *Materials Research Innovations*, 6(5-6):260–272, 2002.

[101] Friedrich Wolff, Christoph Kugler, and Helmut Münstedt. Viscoelastic properties of a silicone resin during crosslinking. *Rheologica Acta*, 50(11-12):917–924, 2011.

[102] Friedrich Wolff, Christoph Kugler, and Helmut Münstedt. Time- and temperature-dependent crosslinking behaviour of a silicone resin. *Rheologica Acta*, 51(1):71–80, 2012.

[103] Herbert Giesche. Mercury Porosimetry: A General (Practical) Overview. *Particle & Particle Systems Characterization*, 23(1):9–19, 2006.

[104] Rami Al-Oweini and Houssam El-Rassy. Synthesis and characterization by FTIR spectroscopy of silica aerogels prepared using several Si(OR)4 and R″Si(OR′)3 precursors. *Journal of Molecular Structure*, 919(1–3):140–145, 2009.

[105] Cekdar Vakifahmetoglu, Marco Balliana, and Paolo Colombo. Ceramic foams and micro-beads from emulsions of a preceramic polymer. *Journal of the European Ceramic Society*, 31(8):1481–1490, 2011.

[106] Liviu Toma, Claudia Fasel, Stefan Lauterbach, Hans-Joachim Kleebe, and Ralf Riedel. Influence of nano-aluminum filler on the microstructure of SiOC ceramics. *Journal of the European Ceramic Society*, 31(9):1779–1789, 2011.

[107] Kyuya Nakagawa, Aurélie Hottot, Séverine Vessot, and Julien Andrieu. Influence of controlled nucleation by ultrasounds on ice morphology of frozen formulations for pharmaceutical proteins freeze-drying. *Chemical Engineering and Processing:*

Process Intensification, 45(9):783–791, 2006.

[108] Adriana E. Delgado, Liyun Zheng, and Da-Wen Sun. Influence of Ultrasound on Freezing Rate of Immersion-frozen Apples. *Food and Bioprocess Technology*, 2(3):263–270, 2009.

[109] Robert Snyder. Ethel Browning's toxicity and metabolism of industrial solvents, 1987.

[110] Pamela A. McGregor, David R. Allan, Simon Parsons, and Stewart J. Clark. Hexamer formation in tertiary butyl alcohol (2-methyl-2-propanol, $C_4H_{10}O$). *Acta Crystallographica Section B Structural Science*, 62(4):599–605, 2006.

[111] Ryo Kobayashi. Modeling and numerical simulations of dendritic crystal growth. *Physica D: Nonlinear Phenomena*, 63(3):410–423, 1993.

[112] E. Brener, H. Müller-Krumbhaar, and D. Temkin. Structure formation and the morphology diagram of possible structures in two-dimensional diffusional growth. *Physical Review E*, 54(3):2714–2722, 1996.

[113] Tomorr Haxhimali, Alain Karma, Frédéric Gonzales, and Michel Rappaz. Orientation selection in dendritic evolution. *Nature Materials*, 5(8):660–664, 2006.

[114] L. Nastac. Numerical modeling of solidification morphologies and segregation patterns in cast dendritic alloys. *Acta Materialia*, 47(17):4253–4262, 1999.

[115] Aaron Lichtner, Denis Roussel, David Jauffrès, Christophe L. Martin, and Rajendra K. Bordia. Effect of Macropore Anisotropy on the Mechanical Response of Hierarchically Porous Ceramics. *Journal of the American Ceramic Society*, pages n/a–n/a, 2015.

[116] Sylvain Deville, Eduardo Saiz, and Antoni P. Tomsia. Freeze casting of hydroxyapatite scaffolds for bone tissue engineering. *Biomaterials*, 27(32):5480–5489, 2006.

[117] Eun-Jung Lee, Young-Hag Koh, Byung-Ho Yoon, Hyoun-Ee Kim, and Hae-Won Kim. Highly porous hydroxyapatite bioceramics with interconnected pore channels using camphene-based freeze casting. *Materials Letters*, 61(11–12):2270–2273, 2007.

[118] Kechao Zhou, Yan Zhang, Dou Zhang, Xiaoyong Zhang, Zhiyou Li, Gang Liu, and Tim W. Button. Porous hydroxyapatite ceramics fabricated by an ice-templating method. *Scripta Materialia*, 64(5):426–429, 2011.

[119] Christopher Peko, Ben Groth, and Ian Nettleship. The Effect of Polyvinyl Alcohol on the Microstructure and Permeability of Freeze-Cast Alumina. *Journal of the American Ceramic Society*, 93(1):115–120, 2010.

[120] Jordi Seuba, Sylvain Deville, Christian Guizard, and Adam J. Stevenson. Gas permeability of ice-templated, unidirectional porous ceramics. *Science and Technology of Advanced Materials*, 0(ja):1–29, 2016.

[121] Mehrad Mehr, Calvin Davis, Kazi Sadman, Ryan J. Hooper, Michele V. Manuel, and Juan C. Nino. Epoxy interface method enables enhanced compressive testing of highly porous and brittle materials. *Ceramics International*, 42(1, Part B):1150–1159, 2016.

[122] Michael M. Porter, Russ Imperio, Matthew Wen, Marc A. Meyers, and Joanna McKittrick. Bioinspired Scaffolds with Varying Pore Architectures and Mechanical Properties. *Advanced Functional Materials*, 24(14):1978–1987, 2014.

[123] Byung-Ho Yoon, Won-Young Choi, Hyoun-Ee Kim, Ji-Hwan Kim, and Young-Hag Koh. Aligned porous alumina ceramics with high compressive strengths for bone tissue engineering. *Scripta Materialia*, 58(7):537–540, 2008.

[124] Jintao Tian and Jiemo Tian. Preparation of porous hydroxyapatite. *Journal of Materials Science*, 36(12):3061–3066, 2001.

[125] Lorna J. Gibson and Michael F. Ashby. *Cellular Solids: Structure and Properties.* Cambridge University Press, 1997.

[126] Suresh Gulati and G Schneider. Mechanical strength of cellular ceramic substrates. *EnviCeram'88(Special edition of CFI, Ceramic Forum International)*, 4(2):118–25, 1989.

[127] Roy W. Rice. *Porosity of Ceramics: Properties and Applications.* CRC Press, 1998. Google-Books-ID: 6pfZdxGLMY0C.

[128] Gary M. Renlund, Svante Prochazka, and Robert H. Doremus. Silicon oxycarbide glasses: Part II. Structure and properties. *Journal of Materials Research*, 6(12):2723–2734, 1991.

[129] Paolo Colombo, John R. Hellmann, and David L. Shelleman. Mechanical Properties of Silicon Oxycarbide Ceramic Foams. *Journal of the American Ceramic Society*, 84(10):2245–2251, 2001.

[130] Andrea Bareggi, Eric Maire, Audrey Lasalle, and Sylvain Deville. Dynamics of the Freezing Front During the Solidification of a Colloidal Alumina Aqueous Suspension: In Situ X-Ray Radiography, Tomography, and Modeling. *Journal of the American Ceramic Society*, 94(10):3570–3578, 2011.

[131] Denis Roussel, Aaron Lichtner, David Jauffrès, Julie Villanova, Rajendra K. Bordia, and Christophe L. Martin. Strength of hierarchically porous ceramics: Discrete simulations on X-ray nanotomography images. *Scripta Materialia*, 113:250–253, 2016.

[132] Hao Bai, Yuan Chen, Benjamin Delattre, Antoni P. Tomsia, and Robert O. Ritchie. Bioinspired large-scale aligned porous materials assembled with dual temperature gradients. *Science Advances*, 1(11):e1500849, 2015.

[133] P Carter, D. C Cox, C. A Gandin, and R. C Reed. Process modelling of grain selection during the solidification of single crystal superalloy castings. *Materials Science and Engineering: A*, 280(2):233–246, 2000.

[134] H. J. Dai, N. D'Souza, and H. B. Dong. Grain Selection in Spiral Selectors During Investment Casting of Single-Crystal Turbine Blades: Part I. Experimental Investigation. *Metallurgical and Materials Transactions A*, 42(11):3430–3438, 2011.

[135] James Mark, Kia Ngai, William Graessley, Leo Mandelkern, Edward Samulski, Jack Koenig, and George Wignall. *Physical Properties of Polymers*. 2004.

[136] Ming-Hui Sun, Shao-Zhuan Huang, Li-Hua Chen, Yu Li, Xiao-Yu Yang, Zhong-Yong Yuan, and Bao-Lian Su. Applications of hierarchically structured porous materials from energy storage and conversion, catalysis, photocatalysis, adsorption, separation, and sensing to biomedicine. *Chem. Soc. Rev.*, 2016.

[137] Michaela Wilhelm, Christian Soltmann, Dietmar Koch, and Georg Grathwohl. Ceramers—functional materials for adsorption techniques. *Journal of the European Ceramic Society*, 25(2–3):271–276, 2005.

[138] Emanuele Zera, Renzo Campostrini, Parakkulam Ramaswamy Aravind, Yigal Blum, and Gian Domenico Sorarù. Novel SiC/C Aerogels Through Pyrolysis of Polycarbosilane Precursors. *Advanced Engineering Materials*, 16(6):814–819, 2014.

[139] Byung-Ho Yoon, Chee-Sung Park, Hyoun-Ee Kim, and Young-Hag Koh. In Situ Synthesis of Porous Silicon Carbide (SiC) Ceramics Decorated with SiC Nanowires. *Journal of the American Ceramic Society*, 90(12):3759–3766, 2007.

[140] Ulrike G. K. Wegst, Hao Bai, Eduardo Saiz, Antoni P. Tomsia, and Robert O. Ritchie. Bioinspired structural materials. *Nature Materials*, 14(1):23–36, 2015.

[141] E. Munch, M. E. Launey, D. H. Alsem, E. Saiz, A. P. Tomsia, and R. O. Ritchie. Tough, Bio-Inspired Hybrid Materials. *Science*, 322(5907):1516–1520, 2008.

This work was supported by the National Science Foundation, DMR-1411218. Portions of this work were performed in the EPIC and Keck-II facilities of the NUANCE Center at Northwestern University. NUANCE Center is supported by NSF-NSEC, NSF-MRSEC, The Keck Foundation, The State of Illinois, and Northwestern University. Portions of this work made use of the J.B. Cohen X-ray Diffraction Facility and the Optical Microscopy and Metallography Facility, supported by the MRSEC program of the National Science Foundation, DMR-0520513, at the Materials Research Center of Northwestern University. Portions of this work made use of the Advanced Photon Source at Argonne National Laboratory.